Optical and Optoelectronic Fiber Devices

by

Ofer Shapira

B.Sc. Electrical Engineering
Technion - Israeli Institute of Technology, Israel, 1997
M.Sc. Electrical Engineering
Technion - Israeli Institute of Technology, Israel, 1999

SUBMITTED TO THE DEPARTMENT OF ELECTRICAL ENGINEERING AND COMPUTER SCIENCE IN PARTIAL FULFILLMENT OF THE REQUIREMENTS FOR THE DEGREE OF

DOCTOR OF PHILOSOPHY IN ELECTRICAL ENGINEERING AND COMPUTER SCIENCE
AT THE
MASSACHUSETTS INSTITUTE OF TECHNOLOGY

JUNE 2007

Signature of Author: _____
Department of Electrical Engineering and Computer Science
March 10, 2007

Certified by: _____
Yoel Fink
Associate Professor of Materials Science
Thesis Supervisor

Accepted by: _____
Arthur M. Smith
Chair, Departmental Committee on Graduate Students

Optical and Optoelectronic Fiber Devices

by
Ofer Shapira

Submitted to the Department of Electrical Engineering and Computer Science
on March 10, 2007 in Partial Fulfillment of the Requirements for the Degree of
Doctor of Philosophy in Electrical Engineering and Computer Science

ABSTRACT: The ability to integrate materials with disparate electrical, thermal, and optical properties into a single fiber structure enabled the realization of fiber devices with diverse and complex functionalities. Amongst those, demonstrated first in our work, are the surface-emitting fiber laser, the hollow-core fiber amplifier, the thermally self-monitored high-power transmission fiber device, and the photo-detecting fiber-web based imaging system. This work presents the design, analysis, and characterization of those devices. It opens with a study of the transmission properties of the multimode hollow-core photonic bandgap fiber constructed of a periodic multilayer cladding. A defect is then introduced into one of the cladding layers and the interaction between core and defect modes is investigated. The second chapter addresses the experimental problem encountered in many multimode waveguide applications: how to extract, and to some extent to control, the modal content of the field at the output of a waveguide. We developed a non-interferometric approach to achieve mode decomposition based on a modified phase retrieval algorithm that can yield the complete vectorial eigenmode content of any general waveguiding structure and demonstrated its validity experimentally. In the third chapter an active material is introduced into the hollow-core to form a surface-emitting fiber laser. A unique azimuthally anisotropic optical wave front results from the interplay between the cylindrical resonator, the anisotropic gain medium, and the linearly polarized axial pump. We show that the direction and polarization of the wave front are directly controlled by the pump polarization. In the last two chapters, a new type of fiber is presented, constructed of semiconducting, insulating, and conducting materials, which enables the integration of semiconductor devices into the fiber structure. In the first we demonstrate a fiber comprised of an optical transmission element designed for the transport of high power radiation and multiple thermal-detecting elements encompassing the hollow core for distributed temperature monitoring and real-time failure detection. In the second, we demonstrate optical imaging using large-area, three-dimensional optical-detector arrays, built from one-dimensional photodetecting optoelectronic fibers. Lensless imaging of an object is achieved using a phase retrieval algorithm.

Thesis Supervisor: Yoel Fink
Title: Thomas B. King Associate Professor of Materials Science

Acknowledgments

My thanks are due firstly to my advisor Prof. Yoel Fink who has provided me with immaculate guidance throughout my PhD program. His profound knowledge in diverse disciplines, enthusiasm, and innovative thinking made my research work exciting and interesting. I would like to thank Prof. John Joannopoulos for his constant support and critical comments. I would also like to thank my committee members Prof. Erich Ippen and Prof. Rajeev Ram for their assistant and comments.

This work could not have been accomplished without the dedicated work of my research group. In particular I am grateful to Dr. Ayman Abouraddy from whom I learned a lot and enjoyed fruitful discussions; Fabien Sorin and Dr. Mehmet Bayindir for their great contribution to the development of device fibers; Dr. Ken Kuriki, Nicholas Orf, Gilles Benoit, and Sasha Stolyarov for their work on the surface-emitting fiber laser. I would also like to thank the reminder of the group for their assistant and support: Dr. Peter Rakich, Dr. Zheng Wang, Zachary Ruff, Jeff Viens, Jerimy Arnold, Dr. Shandon Hart, Dr. Burak Temelkuran, Dr. Sylvain Danto, Dana Shemuly, and Dr. Shunji Egusa. This research was greatly benefited from the collaboration with other research groups, in particular I would like to thank Yaakov Tischler, Dr. Aimee Rose, Larry Takiff, and Kristin Mulherin for providing the organic materials and teaching me about their properties, as well as Dr. Mihai Ibanescu and Alex Rodriguez for their contribution in developing some of the theory behind this work. I would also like to acknowledge the support of DARPA, the ARO, the ONR and the AFOSR who provided much of my funding.

Finally, and most importantly, I am endlessly grateful to my family, my parents Ester and Shlomo, my sisters Orly and Keren, and my brother Chen, for their love and encouragements throughout my years at MIT. This period of time was joyful and pleasant thanks to many of my friends here in Cambridge and in Israel, especially my longstanding friends Vered and Tal Nusbaum, Catherine Bruce, Fabien Sorin, Ayman Abouraddy, and Sasha Stolyarov.

1. Transmission properties of Cylindrical Photonic Bandgap Fiber

1.1 Introduction

The transmission of electromagnetic waves in hollow waveguides dates back to the early seventies with Bell-labs WT4 long-haul communication system [1] designed to transmit millimeter waves in a hollow metallic tube. Although the advent of high-purity silica fibers set the basis for modern optical communication, the approach of confining light in a hollow core using highly reflective walls had been continuously explored [2-5] in a broad range of wavelength and intensities, where solid-core fibers fails. Conventional optical fibers rely on light propagation through total internal reflection in solid materials that has a fundamental limitations stemming from nonlinear effects, light absorption by electrons and phonons, material dispersion and Rayleigh scattering. These limitations have motivated the study of light propagation through air in hollow fibers with many applications in high-power laser guidance for medical procedures [6], atom guiding [7], higher-harmonic generation [8], supercontinuum generation [9], and others. At first, hollow metallic or metallo-dielectric waveguides have been studied extensively and found useful in practical applications, however in the visible and NIR the metal finite conductivity results in high transmission loss as well as limited fabrication length and mechanical flexibility. In order to surmount this problem, an all-dielectric reflector based on photonic bandgap structures was introduced, initially with structures that are based on doped-silica technology that have a low index contrast between the layers [2,10-14]. A more recent work by Fink *et al* [5] demonstrated a Photonic Bandgap (PBG) fiber constructed of a multilayer cylindrical cladding of high refractive-index contrast, leading to large photonic bandgap and omnidirectional reflectivity. The multilayer structure contains alternating layers of chalcogenide glass and a high transition temperature thermoplastic polymer with refractive indices of ~2.8 and ~1.6 ranging from the visible to the MIR, respectively. Hollow core guidance versions of these fibers have recently been successfully fabricated with fundamental photonic bandgaps at 10.6 μm. These fibers have losses that are 4-5 orders of magnitude lower then the cladding material [5] and were used to deliver a high-power CO_2 laser beam for medical applications [15]. A PBG

fiber having the same structure was later fabricated and transmission was demonstrated in the NIR [16].

1.2 Planar Infinite Multilayer

The pertinent theoretical background for the PBG fiber is due to Yeh *et al* [2] demonstrating theoretically transmission of non-index-guided mode through a multilayer cylindrical structure by Bragg reflection from the cladding. A more recent analysis [17] showed that the ability to reflect light of arbitrary angle of incidence and polarization from an all-dielectric planar multilayer structure can be associated with the existence of a complete photonic-bandgap. Such structure, when reshaped into a fiber form may act as an ultra low loss waveguide, high-quality factor cavity, high dispersive medium, and have other unique transmission properties [18-19]. General features of the transport properties of the multilayer cylindrical fiber can be understood from the properties of a planar infinite structure. In a structure with an infinite number of layers, translational symmetry along the direction perpendicular to the layers, r, leads to Bloch wave solution $u_K(r,z) = E_K(r)\exp(iKr)\exp(ik_z z)$ where $E_K(r)$ is periodic with a period of length a, and K is the Bloch wave number. These waves represent solution to an eigenvalue problem and are completely and uniquely defined by the specification of K, k_z, and the frequency $\omega=c|k|$. The solution can be of propagating or evanescent waves, corresponding to real or imaginary Bloch wave numbers, respectively. Figure 1.1 depicts the projected band diagram for a planar multilayer structure having the same parameters of the fiber layers, where both the TE (blue) and TM (light blue) polarizations are overlapped. Regions shown in white correspond to a band gap region in which an incoming plane wave with (k_z,ω) values cannot be transmitted and have an imaginary Bloch wave number (the electric field decays exponentially in the mirror). The gray area shows the range of frequency where a complete photonic band gap exist. For these frequencies light reflects back for every angle of incident and polarization. The blue and light blue regions correspond to plane waves that can couple to propagating modes in the layers with an imaginary Bloch wave number.

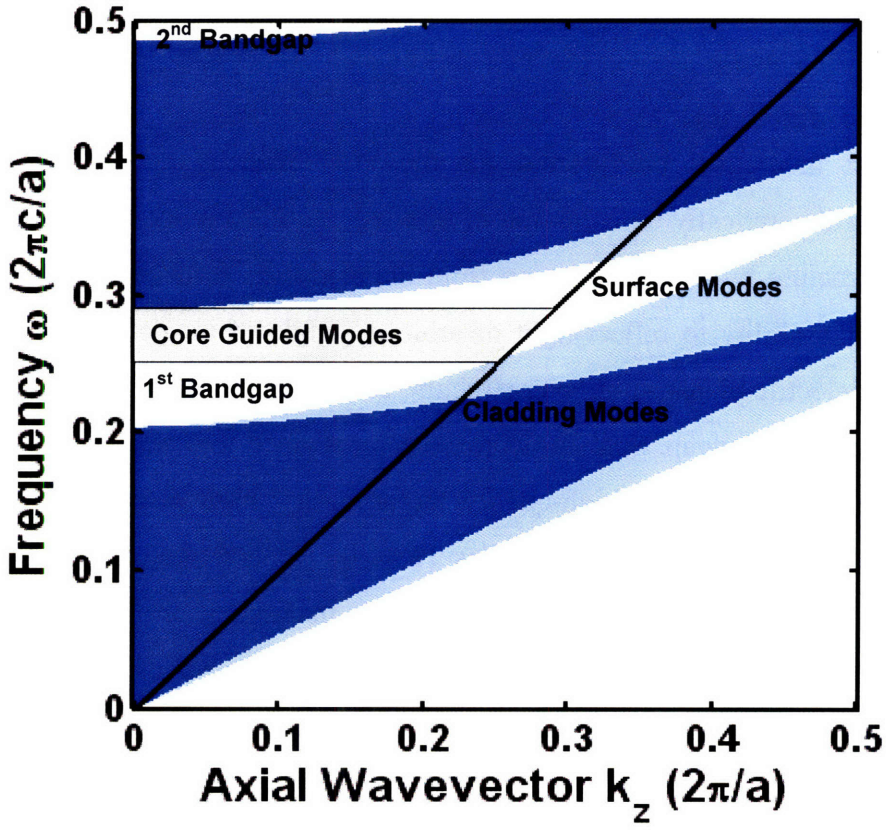

Figure 1.1: Projected band diagram associated with infinite planar multilayer structure. Blue (light blue) regions correspond to TE (TM) polarized light that can propagate through the mirror. White regions correspond to the band gap frequency range in which light reflects back from the mirror. The diagonal black line represents the light line ($\omega=ck_z$). In a fiber with cylindrical geometry, having a multilayer cladding structure with identical layers (thickness and refractive index) to the planar structure, we would expect to find the core propagating modes inside the bandgap and above the light-line, the cladding modes below the light-line and out side of the band gap, and surface modes inside the bandgap but below the light-line.

1.3 Multilayer Cylindrical Photonic Bandgap Fiber

1.3.1 The Electromagnetic Field and Power Flow in a PBG Fiber

In a finite cylindrical structure (Fig. 1.2), the translation symmetry in the direction parallel to the layers, z, is preserved, hence k_z remains a conserved quantity and can be used to label solutions. The cylindrical symmetry results in additional conserved quantity, the "angular momentum" integer m with a wavevector in the azimuthal direction $k_\theta = m/r$. The relevance of the band diagram to cylindrical structures is that in the limit of $r>>m$ the azimuthal wavevector goes to zero and we expects the modes to be confined in the core in a frequency range that corresponds to the band gap of a planar structure having the same structural parameters (i.e., same refractive indices and layers thickness).

Figure 1.2: Hollow-Core Photonic Bandgap Fiber (PBG) constructed from two alternating materials with large refractive index contrast forming an omni-directional reflecting cladding that confined light with frequency inside the bandgap to the core region.

The electric and magnetic fields of waveguides possessing continues translational symmetry along their main axis of propagation can be expressed in the following sep arable form

$$\mathbf{E}(r,\theta,z) = \mathbf{E}(r,\theta)\exp(ik_z z)$$
$$\mathbf{H}(r,\theta,z) = \mathbf{H}(r,\theta)\exp(ik_z z) \tag{1.1}$$

It is convenient to decompose the fields into their transverse and longitudinal components:

(1.1)
$$\mathbf{E} = \left(\mathbf{E}_t + E_z\hat{\mathbf{z}}\right)\exp(ik_z z)$$
$$\mathbf{H} = \left(\mathbf{H}_t + H_z\hat{\mathbf{z}}\right)\exp(ik_z z)$$

The transverse field components can then be expressed in terms of the axial field components

(1.2)
$$\mathbf{E}_t = \frac{i}{k_t^2}\left(k_z\nabla_t E_z - \omega\mu_0\hat{z}\times\nabla_t H_z\right)$$
$$\mathbf{H}_t = \frac{i}{k_t^2}\left(k_z\nabla_t H_z + \omega\varepsilon_0 n^2\hat{z}\times\nabla_t E_z\right)$$

where $k_t^2 = n^2\omega^2/c^2 - k_z^2$ and the axial wave components can be obtained from

(1.3)
$$\left[\nabla_t^2 + \omega^2\mu\varepsilon - k_z^2\right]E_z = 0$$
$$\left[\nabla_t^2 + \omega^2\mu\varepsilon - k_z^2\right]H_z = 0$$

which in cylindrical coordinates takes the form

(1.4)
$$\left(\frac{\partial^2}{\partial r^2} + \frac{1}{r}\frac{\partial}{\partial r} + \frac{1}{r^2}\frac{\partial^2}{\partial\theta^2} + \left(\frac{\omega^2 n^2}{c^2} - k_z^2\right)\right)\begin{pmatrix}E_z\\H_z\end{pmatrix} = 0$$

The general solution of the wave equation in a region of uniform refractive index is given by

(1.5)
$$\begin{pmatrix}E_z\\H_z\end{pmatrix} = \begin{pmatrix}AH_m^{(1)}(k_T r) + BH_m^{(2)}(k_T r)\\CH_m^{(1)}(k_T r) + DH_m^{(2)}(k_T r)\end{pmatrix}e^{\pm im\theta}e^{i(k_z z - \omega t)}$$

where the constants A, B, C, and D are determined by the boundary conditions of the layer. The transverse field components can then be obtained using equation 1.3

(1.6)
$$E_r = \frac{i}{k_t^2}\left(Ak_z k_t H_m^{(1)'}(k_t r) + Bk_z k_t H_m^{(2)'}(k_t r) + C\frac{im\omega\mu_0}{r}H_m^{(1)}(k_t r) + D\frac{im\omega\mu_0}{r}H_m^{(1)}(k_t r)\right)$$
$$E_\theta = \frac{i}{k_t^2}\left(A\frac{imk_z}{r}H_m^{(1)}(k_t r) + B\frac{imk_z}{r}H_m^{(2)}(k_t r) - C\omega\mu_0 k_t H_m^{(1)'}(k_t r) - D\omega\mu_0 k_t H_m^{(2)'}(k_t r)\right)$$
$$H_r = \frac{i}{k_t^2}\left(-A\frac{im\omega\varepsilon_0 n^2}{r}H_m^{(1)}(k_t r) - B\frac{im\omega\varepsilon_0 n^2}{r}H_m^{(1)}(k_t r) + Ck_z k_t H_m^{(1)'}(k_t r) + Dk_z k_t H_m^{(2)'}(k_t r)\right)$$
$$H_\theta = \frac{i}{k_t^2}\left(A\omega\varepsilon_0 n^2 k_t H_m^{(1)'}(k_t r) + B\omega\varepsilon_0 n^2 k_t H_m^{(2)'}(k_t r) + C\frac{imk_z}{r}H_m^{(1)}(k_t r) + D\frac{imk_z}{r}H_m^{(2)}(k_t r)\right)$$

where $\exp\left[i(k_z z - \omega t + m\theta)\right]$ was omitted from each component of the field. For the purpose of matching boundary conditions, it is convenient to express the tangential field components in the following matrix form

$$\begin{pmatrix} E_z^{(n)}(r) \\ E_\theta^{(n)}(r) \\ H_z^{(n)}(r) \\ H_\theta^{(n)}(r) \end{pmatrix} = M^{(n)} \begin{pmatrix} A^{(n)} \\ B^{(n)} \\ C^{(n)} \\ D^{(n)} \end{pmatrix} \tag{1.7}$$

where the 4x4 matrix is given by

$$M^{(n)} = \begin{pmatrix} H_m^{(1)}(k_t r) & H_m^{(2)}(k_t r) & 0 & 0 \\ \frac{\omega\varepsilon_i}{k_z k_t} H_m^{(1)'}(k_t r) & \frac{\omega\varepsilon_i}{k_z k_t} H_m^{(2)'}(k_t r) & \frac{im}{rk_t^2} H_m^{(1)}(k_t r) & \frac{im}{rk_t^2} H_m^{(2)}(k_t r) \\ 0 & 0 & H_m^{(1)}(k_t r) & H_m^{(2)}(k_t r) \\ \frac{im}{rk_t^2} H_m^{(1)}(k_t r) & \frac{im}{rk_t^2} H_m^{(2)}(k_t r) & -\frac{\omega\mu}{k_z k_t} H_m^{(1)'}(k_t r) & -\frac{\omega\mu}{k_z k_t} H_m^{(2)'}(k_t r) \end{pmatrix} \tag{1.8}$$

Boundary conditions require that the tangential fields are continues along the interfaces what yields the 4x4 *transfer* matrix that relates the field coefficient of two adjacent layers

$$\begin{pmatrix} A^{(n+1)} \\ B^{(n+1)} \\ C^{(n+1)} \\ D^{(n+1)} \end{pmatrix} = \left[M^{(n+1)}(r_n)\right]^{-1} M^{(n)}(r_n) \begin{pmatrix} A^{(n)} \\ B^{(n)} \\ C^{(n)} \\ D^{(n)} \end{pmatrix} \equiv M^{i,i+1} \begin{pmatrix} A^{(n)} \\ B^{(n)} \\ C^{(n)} \\ D^{(n)} \end{pmatrix} \tag{1.9}$$

Explicitly, the elements of the matrix $M^{i,i+1}$ are given by

$$m_{11} = H_m^{(2)'}(k_{t,i+1}r)H_m^{(1)}(k_{t,i}r) - \frac{k_{t,i+1}\varepsilon_i}{k_{t,i}\varepsilon_{i+1}} H_m^{(2)}(k_{t,i+1}r)H_m^{(1)'}(k_{t,i}r)$$

$$m_{12} = H_m^{(2)'}(k_{t,i+1}r)H_m^{(2)}(k_{t,i}r) - \frac{k_{t,i+1}\varepsilon_i}{k_{t,i}\varepsilon_{i+1}} H_m^{(2)}(k_{t,i+1}r)H_m^{(2)'}(k_{t,i}r)$$

$$m_{13} = \frac{imk_z k_{t,i+1}}{r\omega\varepsilon_{i+1}}\left(\frac{1}{k_{t,i+1}^{\ 2}} - \frac{1}{k_{t,i}^{\ 2}}\right) H_m^{(2)}(k_{t,i+1}r)H_m^{(1)}(k_{t,i}r)$$

$$m_{14} = \frac{imk_z k_{t,i+1}}{r\omega\varepsilon_{i+1}}\left(\frac{1}{k_{t,i+1}^{\ 2}} - \frac{1}{k_{t,i}^{\ 2}}\right) H_m^{(2)}(k_{t,i+1}r)H_m^{(2)}(k_{t,i}r)$$

$$m_{21} = -H_m^{(1)'}(k_{t,i+1}r)H_m^{(1)}(k_{t,i}r) + \frac{k_{t,i+1}\varepsilon_i}{k_{t,i}\varepsilon_{i+1}} H_m^{(1)}(k_{t,i+1}r)H_m^{(1)'}(k_{t,i}r)$$

$$m_{22} = -H_m^{(1)'}(k_{t,i+1}r)H_m^{(2)}(k_{t,i}r) + \frac{k_{t,i+1}\varepsilon_i}{k_{t,i}\varepsilon_{i+1}} H_m^{(1)}(k_{t,i+1}r)H_m^{(2)'}(k_{t,i}r)$$

$$m_{23} = -\frac{imk_z k_{t,i+1}}{r\omega\varepsilon_{i+1}}\left(\frac{1}{k_{t,i+1}^{\ 2}} - \frac{1}{k_{t,i}^{\ 2}}\right) H_m^{(1)}(k_{t,i+1}r)H_m^{(1)}(k_{t,i}r)$$

$$m_{24} = -\frac{imk_z k_{t,i+1}}{r\omega\varepsilon_{i+1}}\left(\frac{1}{k_{t,i+1}^{\ 2}} - \frac{1}{k_{t,i}^{\ 2}}\right) H_m^{(1)}(k_{t,i+1}r)H_m^{(2)}(k_{t,i}r)$$

$$m_{31} = -\frac{imk_z k_{t,i+1}}{r\omega\mu}\left(\frac{1}{k_{t,i+1}^{\ 2}} - \frac{1}{k_{t,i}^{\ 2}}\right) H_m^{(2)}(k_{t,i+1}r)H_m^{(1)}(k_{t,i}r)$$

$$m_{32} = -\frac{imk_z k_{t,i+1}}{r\omega\mu}\left(\frac{1}{k_{t,i+1}^{\ 2}} - \frac{1}{k_{t,i}^{\ 2}}\right) H_m^{(2)}(k_{t,i+1}r)H_m^{(2)}(k_{t,i}r)$$

$$m_{33} = H_m^{(2)'}(k_{t,i+1}r)H_m^{(1)}(k_{t,i}r) - \frac{k_{t,i+1}}{k_{t,i}} H_m^{(2)}(k_{t,i+1}r)H_m^{(1)'}(k_{t,i}r)$$

$$m_{34} = H_m^{(2)'}(k_{t,i+1}r)H_m^{(2)}(k_{t,i}r) - \frac{k_{t,i+1}}{k_{t,i}} H_m^{(2)}(k_{t,i+1}r)H_m^{(2)'}(k_{t,i}r)$$

$$m_{41} = \frac{imk_z k_{t,i+1}}{r\omega\mu}\left(\frac{1}{k_{t,i+1}^{\ 2}} - \frac{1}{k_{t,i}^{\ 2}}\right) H_m^{(1)}(k_{t,i+1}r)H_m^{(1)}(k_{t,i}r)$$

$$m_{42} = \frac{imk_z k_{t,i+1}}{r\omega\mu}\left(\frac{1}{k_{t,i+1}^{\ 2}} - \frac{1}{k_{t,i}^{\ 2}}\right) H_m^{(1)}(k_{t,i+1}r)H_m^{(2)}(k_{t,i}r)$$

(1.10)

$$m_{43} = -H_m^{(1)'}(k_{t,i+1}r)H_m^{(1)}(k_{t,i}r) + \frac{k_{t,i+1}}{k_{t,i}} H_m^{(1)}(k_{t,i+1}r)H_m^{(1)'}(k_{t,i}r)$$

$$m_{44} = -H_m^{(1)'}(k_{t,i+1}r)H_m^{(2)}(k_{t,i}r) + \frac{k_{t,i+1}}{k_{t,i}} H_m^{(1)}(k_{t,i+1}r)H_m^{(2)'}(k_{t,i}r)$$

The relation between the field coefficients at the center of the fiber ($r = 0$) and the outermost layer can then be expressed by multiplication of transfer matrices

$$\begin{pmatrix} A^{(N)} \\ B^{(N)} \\ C^{(N)} \\ D^{(N)} \end{pmatrix} = M^{N+1,N} \cdots M^{1,0} \begin{pmatrix} A^{(0)} \\ B^{(0)} \\ C^{(0)} \\ D^{(0)} \end{pmatrix} \equiv M^{T} \begin{pmatrix} A^{(0)} \\ B^{(0)} \\ C^{(0)} \\ D^{(0)} \end{pmatrix} \tag{1.11}$$

The problem of identifying the modes of this fiber reduces to setting boundary conditions at the center of the core and at the outermost layer and finding pairs of (w, k_z) that solve the above equation. We expect to find the solutions for the core propagating modes within the bandgap of the one-dimensional structure and above the light-line. Such modes must have exponentially decaying solutions in the cladding. The modes in such dielectric structure resemble those of a metallic waveguide in which light is strongly confined in the core by the reflection from the metallic walls (for optical frequencies however metal absorption results in higher propagation losses). In the band-gap region of the dielectric structure we expect the mode properties of the two types of waveguides to be similar because in both cases the mirror is a very good reflector for all angles of incident and polarization.

The PBG fiber also supports other categories of modes. One category includes modes that are index guided in the dielectric mirrors. These modes are located below the light line outside of the bandgap (Fig. 1.1) and their field decays exponentially in the air region but extends throughout the dielectric region. Another category includes modes that decay both in the air regions and in the dielectric layers and they are located under the light line but inside the band-gap. These can exist as a surface state between the core and the multilayer cladding or as a defect state inside the multilayer structure incase a defect is introduce to one (or more) layers.

For the remain of this section, we chose to demonstrate the transmission properties of a PBG fiber that has a core diameter of 10λ (Fig 1.3a), 10 bilayers of alternating As_2Se_3 and PES having a refractive indices of 2.8 and 1.6, respectively, and material losses of 35dB/m and 3500dB/m, respectively. The layers thicknesses are determined by the

quarter wave condition along the light line [21] $d_{hi}/d_{lo} = \sqrt{n_{lo}^2 - 1}/\sqrt{n_{hi}^2 - 1}$ to be d_{As2Se3}=0.33a and d_{PES}=0.67a, where a is a bilayer thickness. In this structure the first glass layer surrounding the air-core has thickness of $d_{hi}/2$ in order to suppress coupling to surface states – we discuss this possibility further below.

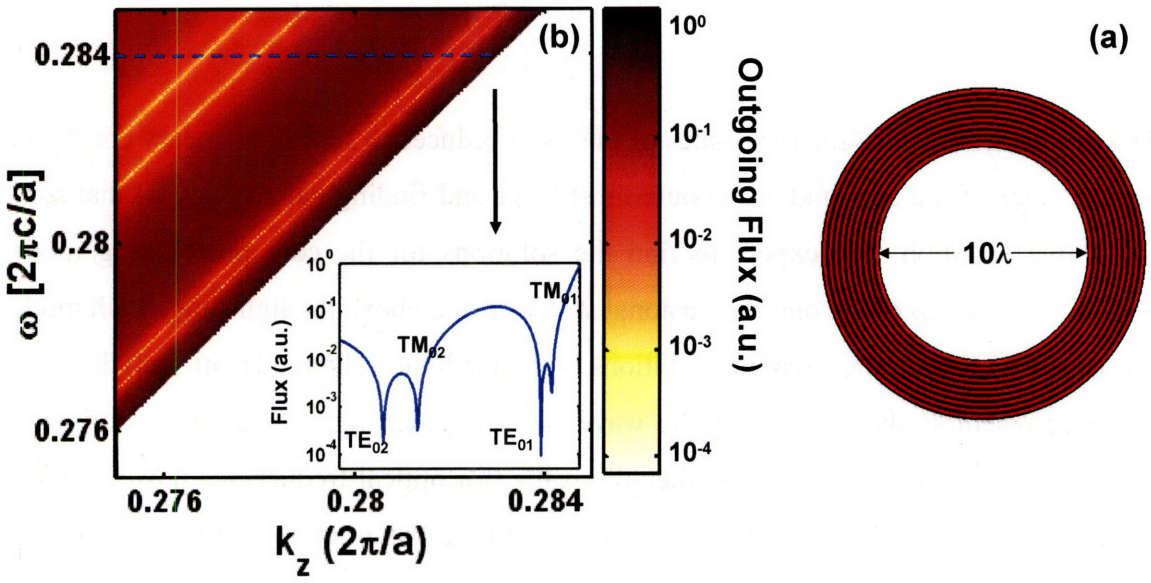

Figure 1.3: (a) A PBG fiber with core diameter of 10λ and 10 bilayers of alternating As_2Se_3 and PES having refractive indices of 2.8 and 1.6, respectively. **(b)** Outgoing radial flux of modes with m=0 for (k_z,ω) pairs in the center of the band-gap near the light-line. The inset shows a cross section where the core-guided modes can be identified by the minima in the flux.

The guided modes can then be found by simply finding the values of (k_z,ω) that minimize the total outgoing flux in the radial direction, $S_{r,outward}$, at the outermost layer

$$\int_0^{2\pi} S_{r,outward} d\theta = \frac{\omega}{k_T^2 r}\left(\varepsilon |A_N|^2 + \mu |C_N|^2\right) \tag{1.12}$$

This is by noting that in the limit of $k_T r \to \infty$ the first and second Hankel functions get the form of outgoing and incoming plane waves, respectively. Figure 1.3b depicts a calculation of the outgoing flux in a small range of frequencies in the center of the band gap close to the light-line for modes with angular momentum of zero. The minima in flux, as discerned from the inset of Fig. 1.3b, corresponds to the first four lowest energy core-propagating modes with $m=0$. Unlike truly guided modes of infinite structure, these

modes are leaky resonances and are characterized by a continuum of k_z values centered on $k_{z,n}$ having a width of $\Delta k_{z,n}$ proportional to the radiative loss.

1.3.2 The Leaky Mode Technique

A somewhat more powerful technique for the calculation of guided modes is the leaky mode method [20] in which an eigenvalue k_z is expanded to the complex plane, allowing to satisfy the boundary condition of no electromagnetic sources outside the waveguide. For a PBG fiber this method is employed by setting the boundary condition of zero incoming radial flux at the outermost layer

$$\begin{pmatrix} A^{(N+1)} \\ 0 \\ C^{(N+1)} \\ 0 \end{pmatrix} = M^T \begin{pmatrix} a_0 \\ a_0 \\ \left(0.5-a_0^2\right)^{0.5} \\ \left(0.5-a_0^2\right)^{0.5} \end{pmatrix} \tag{1.13}$$

where the choice of $A^{(0)}=B^{(0)}$ and $C^{(0)}=D^{(0)}$ is necessary to obtain finite field amplitudes at the center of the core, a is a constant that can be written as a function of the matrix elements M^T such that the outgoing flux is minimized, and the coefficient vector in the core is normalized. The choice of zero incoming flux, $B^{(N+1)}=D^{(N+1)}=0$, is satisfied for those pairs of w and complex k_z that solves [18]

$$\det\begin{pmatrix} M_{2,1}^T + M_{2,2}^T & M_{2,3}^T + M_{2,4}^T \\ M_{4,1}^T + M_{4,2}^T & M_{4,3}^T + M_{4,4}^T \end{pmatrix} = 0 \tag{1.14}$$

The solution obtained is of leaky modes with complex wave vectors. These modes are resonant modes that have most of their energy traveling within the hollow core, and a field that decays exponentially in the radial direction in the dielectric layers. Their k_z and ω situate them inside the band-gap of the planar structure and above the light line. The axial wavevector, k_z, has an imaginary part that is proportional to the radiative loss of the mode, $\alpha_n=2\mathrm{Im}\{k_{z,n}\}$. We calculate the modes properties for the azimuthally polarized TE_{01}, radially polarized TM_{01}, and linearly polarized HE_{11} for the suggested structure. Figure 1.4 depicts the dispersion curves of the three modes overlapped with the band diagram while the inset shows an enlarged section near the light line. Since the core is

much larger then the wavelength the modes become TEM-like in the sense that their field components are mostly in the transverse plane (small E_z and H_z components) and their dispersion curve is nearly parallel to the light line. To provide a better understanding of the field pattern in such fiber we plotted the time average energy density in Fig. 1.4b at a frequency of $\omega = 0.284$ ($2\pi c/a$). The three modes are very well confined within the core as evident from the unnoticeable energy density in the cladding. Unlike the other modes, the TE_{01} has a node near the core cladding-interface what contribute significantly to the lower losses of these modes comparing to the TM or mixed polarized modes [18].

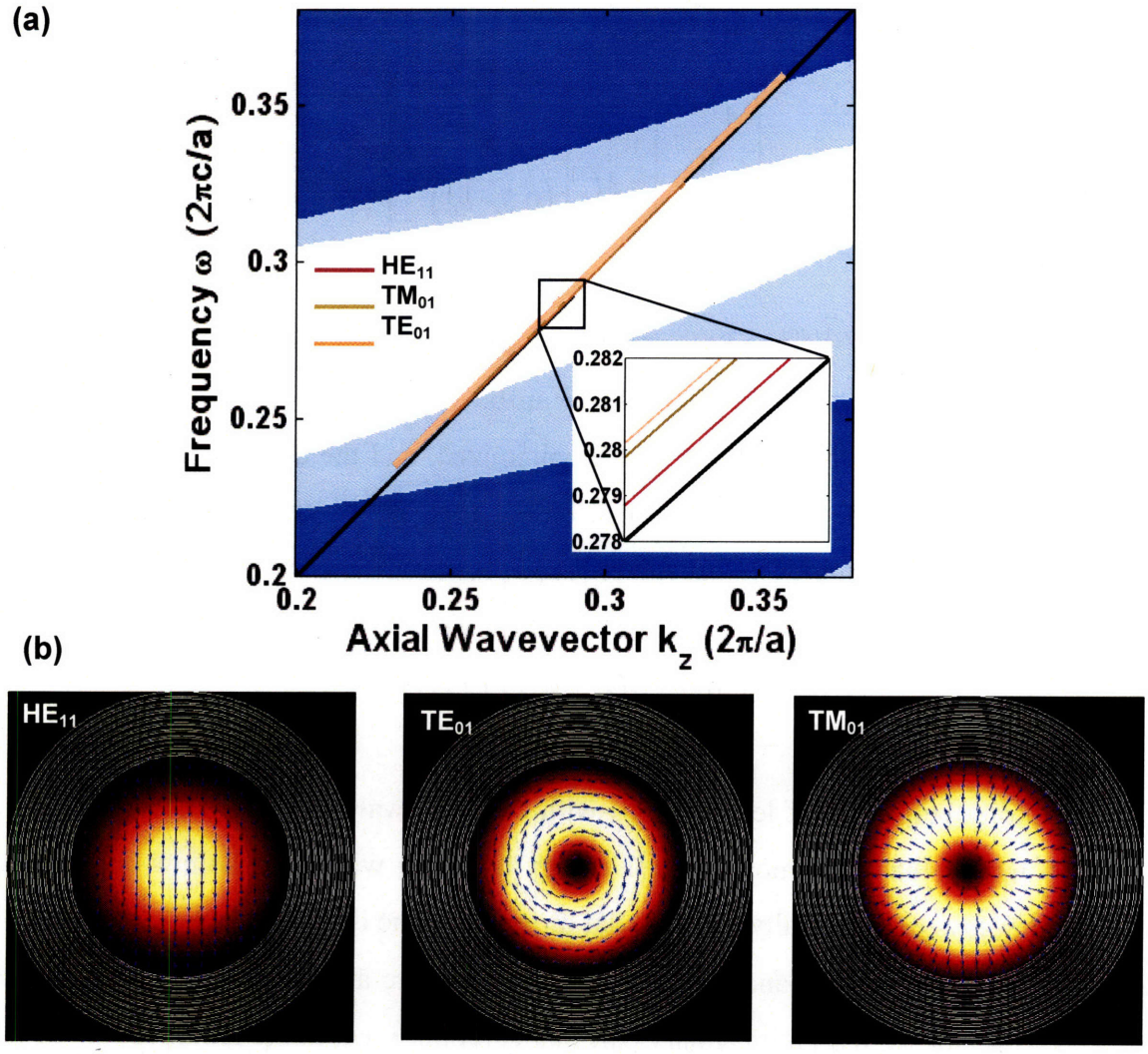

Figure 1.4: (a) Dispersion curves of the TE_{01}, TM_{01}, and HE_{11} overlapped with the band-gap diagram of the planar infinite structure. The inset shows an enlarged portion near the light-line where these three modes can be resolved. **(b)** Intensity mode profiles of the three modes.

1.3.3 Modal Losses

In Fig. 1.5a, we display the computed losses due to radiation and material losses for the three discussed modes. The narrower TM band gap results in higher losses for the pure TM modes, with the TM_{01} having losses almost two orders of magnitude higher then the TE_{01}, the lowest loss mode. The wider TE band gap results in wider bandwidth for the pure TE modes, while the pure TM modes are confined to the narrower TM band gap. Modes with $m>0$, as the HE_{11}, have mixed polarization (called hybrid modes) and therefore their losses, as well as their bandwidth, are eventually dominant by their less confined TM component. These differential losses create a mode-filtering effect that allows the TE_{01} to operate as in a single mode regime, despite the core diameter of many wavelengths. However, as the core size increase, fiber perturbations results in stronger mode coupling and therefore higher effective modal losses [18].

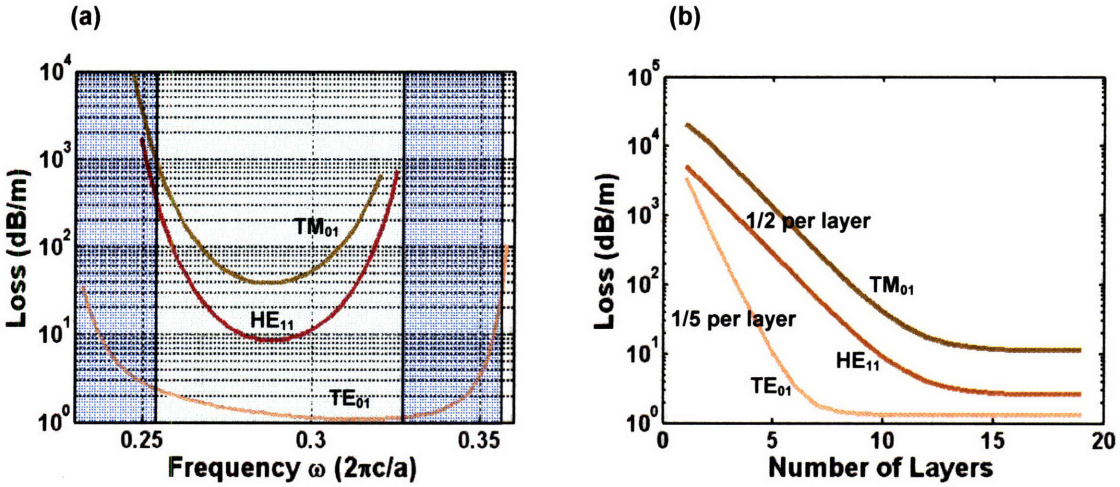

Figure 1.5: (a) Losses for the three lowest energy modes of a PBG fiber (including material losses). The TE_{01} is the lowest loss modes, while the TM_{01} has losses almost two order of magnitude higher due to the narrower TM band gap. The HE_{11}, being a hybrid mode, has losses that are dominated by the TM component. **(b)** Losses as function of bilayer number. The TE_{01} radiation loss decreases by a factor of 5 per bilayer while the TM_{01} and HE_{11} by a factor of 2. The TE_{01} as smaller number of effective layers.

For all modes, radiation losses decrease exponentially with increasing numbers of layers thank to the reflection from the band gap, until the point where material losses become more dominant. For our structure, the radiation losses for the pure TE modes decrease by a factor of 5 per bilayer (Fig. 1.5b) while for the pure TM and hybrid modes by a factor

of 2. The material losses for each mode are proportional to the field amplitude in the cladding and determine the number of effective bilayers. It turns out that for the TE_{01} this number of layers is smaller then for the other modes.

The possibility of having a single mode regime in a PBG fiber that is much larger then the wavelength suggests that it would be advantages to use larger core fibers in order to reduce the modal losses. S.G. Johnson *et al* [18] studied the scaling trends of modes with respect to the core radius and showed that the losses of a pure TE-polarized mode reduces faster for increasing core radii then of any other mode due to a node in the electric field near the core-cladding interface. A calculation of the modes losses as a function of the core radii (Fig. 1.6) suggests that for small core radii the losses of the TE_{01} indeed decreases faster then any other mode. However, for larger core radii, the scaling of the losses for the different modes becomes comparable.

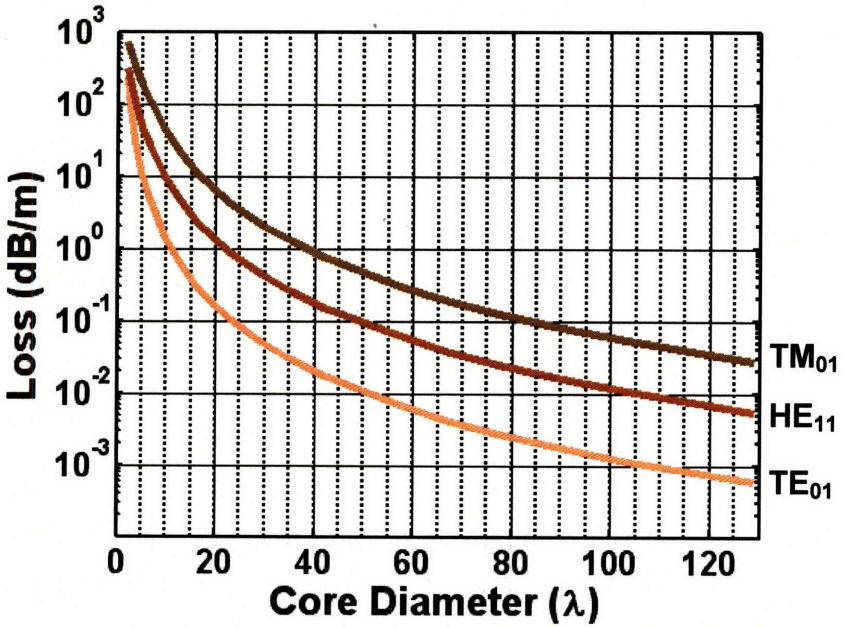

Figure 1.6: The losses of the PBG fiber modes decreases with an increase of the core size due to better confinement of the modes in the core (higher portion of the mode travels in the core). The lower losses of the TE_{01} mode suggests that this fiber, although having core size much larger then the transmitted wavelength, can operate in a single mode regime.

Ultra low loss propagation can be obtained for the TE_{01} mode for larger core radii with structure parameters that are practical in terms of fabrications. For example, a 110

wavelength core diameter can be easily fabricated and has losses smaller then 1dB/km for the TE_{01}. However, for larger core radii the mode spacing in phase space decreases (scales with the core area) and structural perturbations, such as fiber bends, induce mode coupling that results in higher effective losses.

1.3.4 Group Velocity Dispersion in PBG Fiber

For a large core fiber the core-guided modes become TEM-like in the sense that the electric field is predominantly in the transverse direction, with only a small component in the axial direction. Accordingly, the dispersion curves, as plotted in Fig. 1.4, are parallel to the light line with a group velocity approaching the speed of light inside the band gap. At the edges of the band gap the group velocity decreases as a result of the gradual loss of confinement within the core (larger portion of the field travels in the cladding), as depicted in Fig. 1.7a. The group velocity dispersion is positive near the lower edge of the band gap, positive in the upper edge and transitions through zero. Inside the band gap, the dispersion slope increases for smaller core radii, however the bandwidth of the (relatively) flat region decreases.

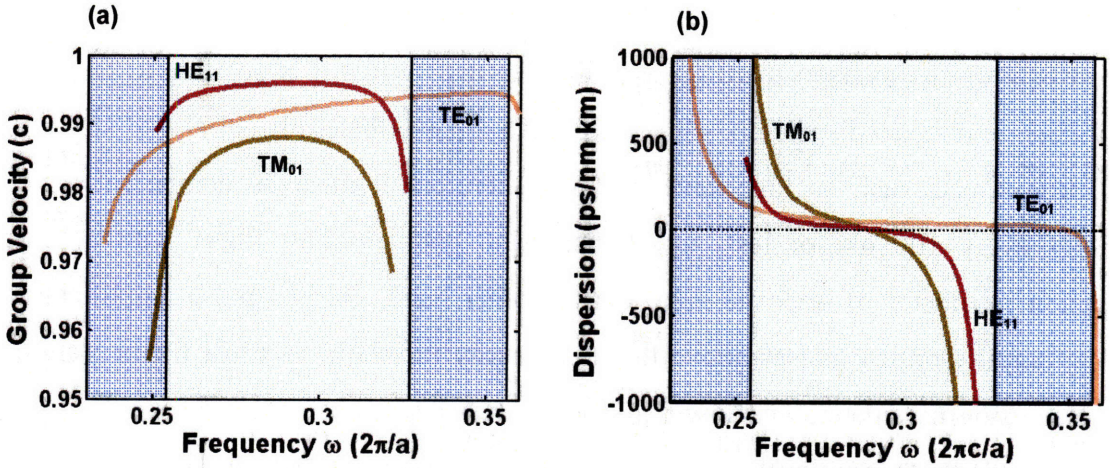

Figure 1.7: (a) the group velocity within the band-gap approaches the speed of light, while at the edges it becomes smaller due to the gradual increase in the portion of the field that travels in the cladding. **(b)** The group velocity dispersion is positive near the lower edge of the band gap, positive in the upper edge and transitions through zero.

1.3.5 Defect and Surface States

The periodic Bragg structure that lines the hollow core of the PBG fiber and is responsible for the omnidirectional reflectivity offers flexibility in integrating defect layers or microcavities that in turn can be used to precisely control the loss, dispersion and non-linearities of resonant transmitted modes [21]. We have previously demonstrated that the resonance frequency of microcavities embedded in fibers designed for external reflection can be reversibly tuned through mechanical and all-optical tuning schemes [22]. By intentionally introducing such microcavities in PBG fibers, one can achieve very large dispersion as a result of interactions between core-guided modes and cavity-resonant modes, independently of the materials intrinsic dispersion. In addition, because the dispersion is controlled primarily by geometric parameters, mechanical tuning can be employed to fine-tune the value of the dispersion coefficient at a given wavelength and even switch its sign. While these fibers can be used for dynamic dispersion compensation, they can also be used for zero-dispersion transmission or all-fiber chirped pulse amplification.

Depending on the application pursued, dispersion can be a limitation or a benefit. In telecommunication applications, dispersion leads to a degradation of the optical signal at high bit rates or over long distances. For a given distance, the dispersion tolerance is proportional to the inverse square route of the bite rate. While it is possible to fabricate silica fibers with zero dispersion, some dispersion is nevertheless beneficial to suppress non-linear effects such as four-wave mixing. Therefore it must be compensated for, typically every 100 km or less, using dispersion compensating fibers with a large dispersion parameter of opposite sign. On the other hand, chirped pulse amplification used to amplify optical pulses above the nonlinearity threshold of silica fibers requires high dispersion parameters and low non-linearities, which is achieved using diffraction gratings, fiber Bragg gratings and more recently hollow core photonic band-gap fibers [23,24]. High dispersion parameters have been reported in photonic band-gap optical fibers (e.g. 1150 ps/nm/km at 1560 nm) [23] but to this date only at the edge of their photonic band-gaps where propagation losses are high and little control over the dispersion of individual propagating modes can be achieved. Here we demonstrate that by intentionally introducing micro-cavities in such fibers, one can achieve much higher

normal and anomalous dispersion parameters within their photonic band-gaps as a result of interactions between core-guided modes and resonant cavity modes, thus combining controlled dispersion with the advantages of fiber waveguiding. We show that there exists a strong correlation between the dispersion's amplitude and bandwidth and the different fiber design parameters. In addition, because the dispersion is controlled primarily by geometric parameters, mechanical tuning can be employed to dynamically fine-tune the value of the dispersion coefficient and even switch its sign. While these fibers could be used for precise dispersion compensation in telecommunication applications and enable dynamic allocation of bit rates, they could also be used for all-fiber chirped pulse amplification and enable peak powers thought unreachable, beyond the damage threshold of most materials, for virtually any desired wavelength of operation.

Theoretically, by varying the thickness or refractive index of a single layer in the multilayer structure a defect is introduced in the periodic structure that may permit localized modes to exist with frequencies inside the photonic bandgap. The multilayer film surrounding the defect behave like frequency-specific mirrors in which light bounces back and forth between the two sides with exponentially decaying electromagnetic fields in the multilayer structure. The core of a PBG fiber can also be regarded as a "defect" to the multilayer cladding. The previous section provided a detailed description of the states that are confined in the core region. In both cases the surface between the periodic structure and the defect can support *surface* states that are confined to the interface and decays exponentially in both the defect region and in the periodic structure.

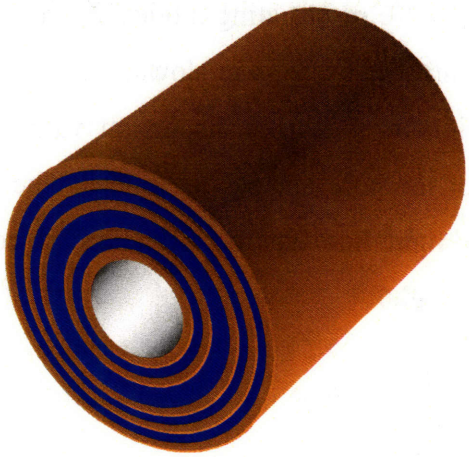

Figure 1.8: PBG fiber with a double thickness layer of the high-refractive index glass forming a λ/2 defect state.

The characteristics of a defect state within the multilayer cladding can be studied conveniently when it is decoupled from the core modes. Consider a PBG fiber with a defect introduced to the cladding in the form of thickness variation of one of the high-index layers as shown in figure 1.8. Since the field of the defect state decay exponentially within the multilayer structure, it is sufficient to locate the defect only few bilayers away from the core such that the mode profile is only weekly altered due to the break of periodicity of the core. Of most interest are defect structures that can support only one or not more then few defects states. It is therefore sufficient to consider defects sizes that are less then twice the original layer size. Figure 1.9 depicts the "band diagram" of the cylindrical structure having a defect layer thickness twice its original size overlapped with the bandgap diagram of the infinite periodic planer structure. Few salient features of the mode structure can already be pointed. First, the dispersion curves of the different fiber modes appear in the corresponding areas of the infinite planar structure. The core modes appears in the bandgap above the light line, while the index guided modes in the high-index layers appears between the light lines of the two cladding materials. The defect state appears in the center of the band gap extending from normal incident angle all the way to the high-index material light line. Lastly, a surface state emerges from the lower edge of the bandgap near the light line. We note that both the defect and the surface states exist within the bandgap. Second, the dispersion curve of the defect state indicate slower group velocity then core propagating modes due to the higher refractive index as well as smaller cavity volume that results in slower axial propagation. This difference in group velocity is the origin of the high dispersion values obtained in the frequency vicinity of the crossing of the core and defect modes. The defect state itself is nearly-degenerate above the air light line but the TE and TM component of it splits when approaching the Brewster angle.

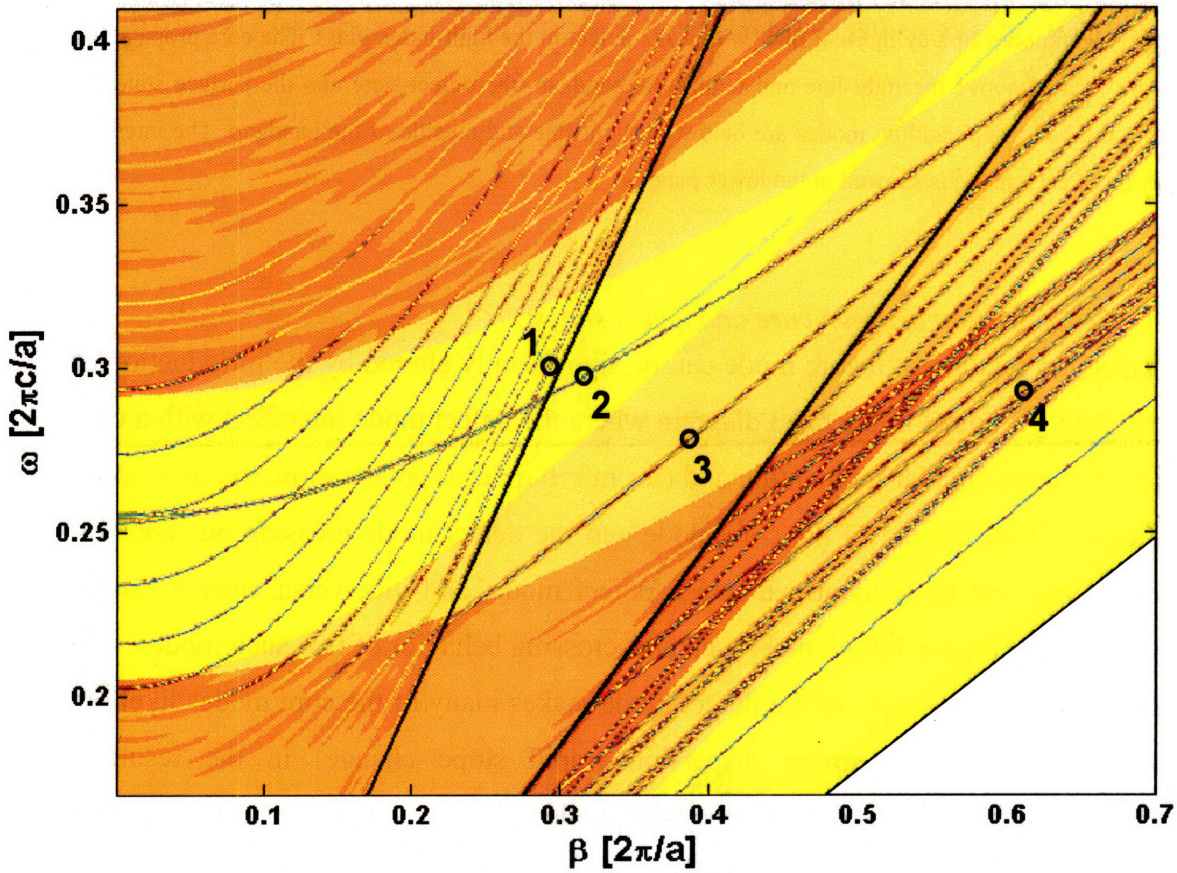
0.4
0.35
0.3
0.25
0.2
ω [2πc/a]
0.1
0.2
0.3
0.4
0.5
0.6
0.7
β [2π/a]
1
2
3
4

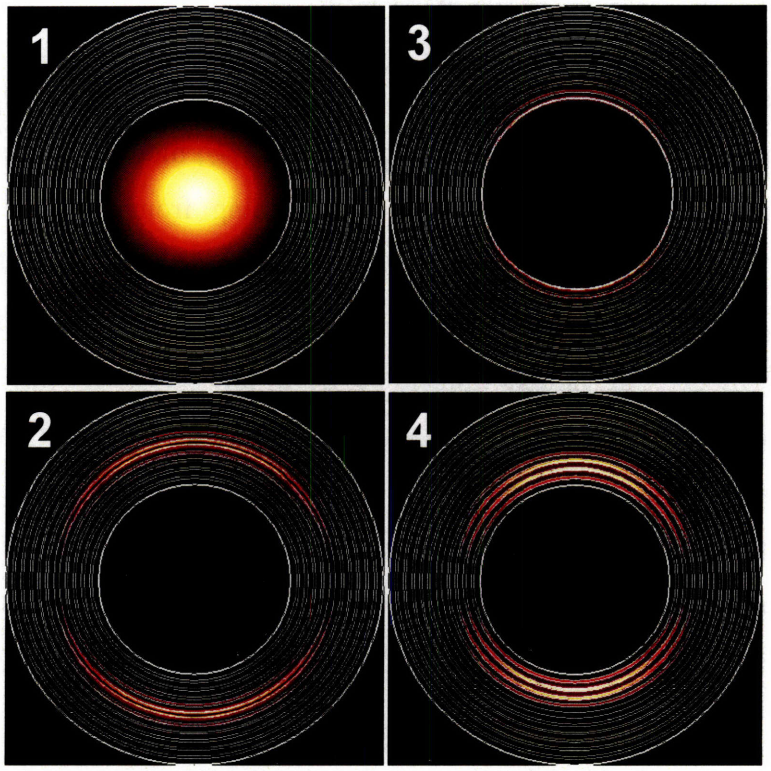
1
3
2
4

Figure 1.9: Upper panel: Band-diagram of an infinite planar multilayer structure projected on the calculated eigenmodes of a cylindrical fiber with a λ/2 defect in the high-index glass. The core propagating modes are located above the light-line and within the bandgap, the defect-state and the surface state are located in the bandgap, cladding modes are below the light line and outside of the bandgap. The intensity distribution of each mode is showed in the lower panel.

1.3.6 The interaction between core and defect states

The dispersion relation of a core mode can be significantly altered by the introduction of a defect state. At points in the band diagram where the defect mode intersects with a core mode of the same angular momentum and (for m = 0 modes) polarization, the two modes can interact. Thus, instead of the core mode and the defect mode crossing one another, the core mode will be transformed into a defect mode, and vice-versa, over a certain frequency range. Figure 1.10 depicts such anti-crossing behavior of two such modes. The much smaller group velocity of the defect mode makes many of the core modes likely to intersect, and implies a strong dispersion (rapid slope change) in the resulting anticrossing. In the transition region, the core mode radically changes its group velocity which is synonymous with that mode having a large dispersion parameter in that frequency range. The lower panel of Fig. 1.10 illustrates the transition of an HE_{11} from core-confined to a resonant cavity mode (transforming from A to C). Around the transition frequency the next lowest ($m = 1$) mode, the EH_{11} mode, changes its character, and it starts to resemble he HE_{11} mode (transforming from B to D). For higher frequencies, the mode which at lower frequencies was almost identical to the EH_{11} mode is now almost completely identical to the HE_{11} mode of the defect-free fiber. We thus see that the defect mode can induce transition from one core-confined mode to its neighboring core-confined mode. This change continues for all higher modes, and we therefore see that the presence of the defect makes all the core-confined modes take a step down around the frequencies where the defect mode crosses the dispersion curve of the core-confined modes. Transitions between core-confined modes can give large dispersion values with frequency region of large negative dispersion followed by a region of large positive dispersion.

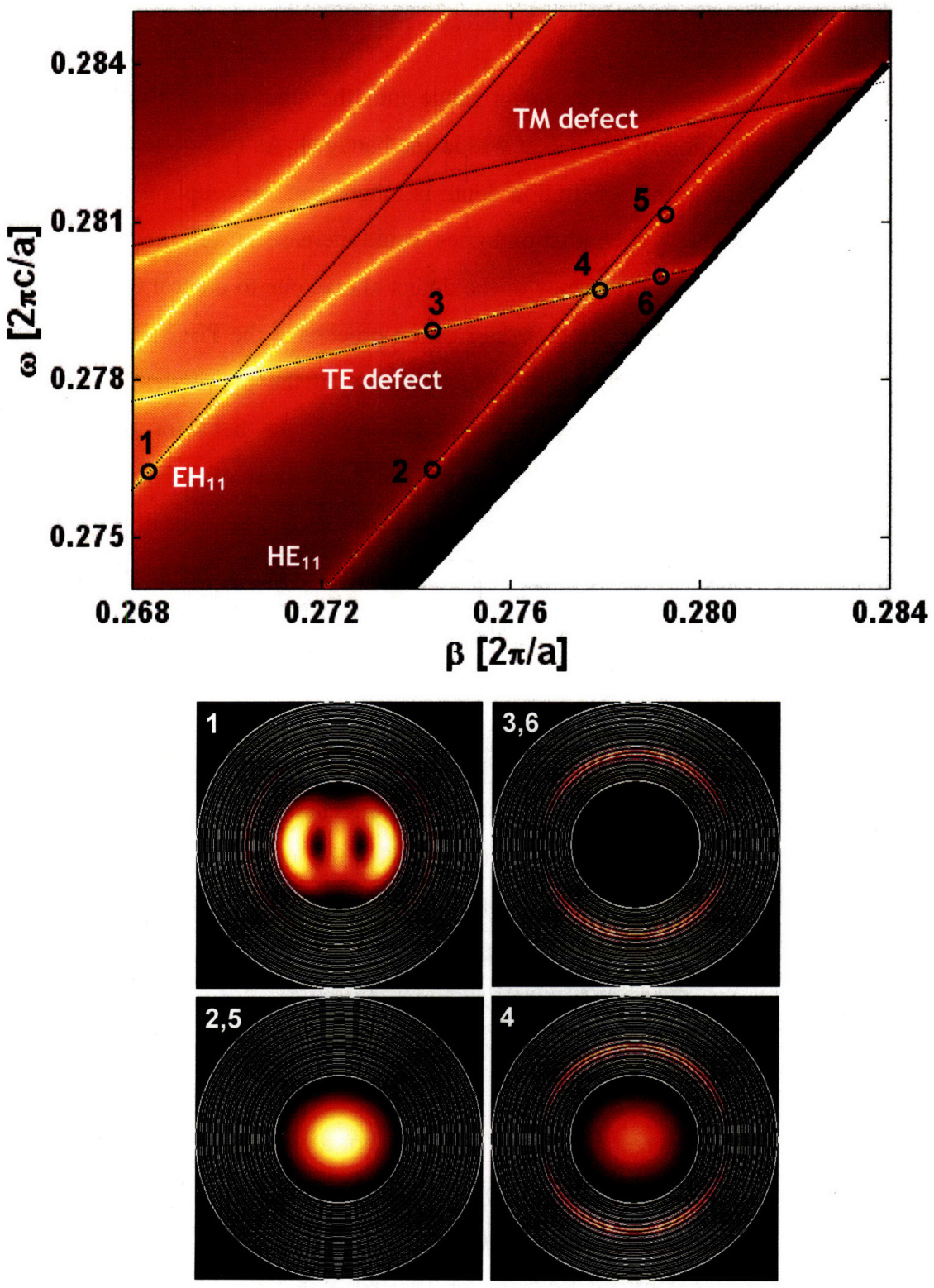

Figure 1.10: (upper panel) Magnified section of the band-diagram showing the interaction of defect state with core modes (modes appear in brighter colors). The TE-defect mode is better confined to the defect layer and therefore the coupling coefficient with the core mode is smaller then of the TM-defect. (lower

panel) Mode profiles of four points on the band-diagram depicting the step-down transition of the HE_{11} mode after the interaction with the defect state and the transition of the EH_{11} to the HE_{11}.

The field penetration depth of the defect mode into the surrounding Bragg mirror is determined by the location of the defect within the bandgap. As the mode gets closer to the edges of the bandgap the penetration depth is longer and the coupling with the core mode is stronger. Obviously the radiation losses would increase as well; nevertheless, the ability to tune the resonance frequency of the defect allows one to control the interaction frequency, strength and bandwidth. The fabrication process of the PBG fiber allows the simple introduction of defects with varying thickness in the high-index glass at any location of the multilayer cladding. Figure 1.11 depicts the behavior of the defect resonance frequency as a function of its thickness in the vicinity of the light line. Since the dispersion curve of the lowest energy core modes for such large core fiber is, to good approximation, parallel to the light line. The upper panel shows that a defect state is pushed into the bandgap from the high-dielectric band when the thickness of the defect layer ($d_{high} < 1$) is reduced. On the other hand, when increasing the thickness of the defect layer a defect state leaves the low-index band and pushed into the bandgap. This behavior is due to the fact that for increasing defect size the field fraction in the high-index region is larger and therefore the energy of the mode is lower. That can also explained by using the electromagnetic variational theorem that shows that the lowest frequency mode is the field pattern that minimizes the electromagnetic energy functional. It can be showed [25] that the minimum value is obtained when the displacement field **D** is concentrated in the high dielectric. That explains why the lowest energy modes are concentrated in the high dielectric region and the higher energy modes are concentrated in the low dielectric region. The bottom panel of figure 1.11 shows the **D** field distribution in the radial direction of the different defect modes for $\omega = 0.28$. For a given thickness of defect state there are two modes, one TE-like with a dominant field in the azimuthally direction and a TM-like with a dominant field in the radial direction. The narrower bandgap of the TM modes results in a less confined field of the TM-like mode as evident from the right panels of figure 1.11. For values of d_{high} much smaller then 1 (quarter wavelength) the field is mostly concentrated in the low-dielectric polymer and practically can be regarded

as a low-dielectric defect, the boundary conditions in such case force nodes in the field on the interface between the "defect" and the higher-index mirrors. On the other hand, for defect size greater then unity the boundary conditions require anti-nodes on the surface as evident from the insets of the figure 1.11.

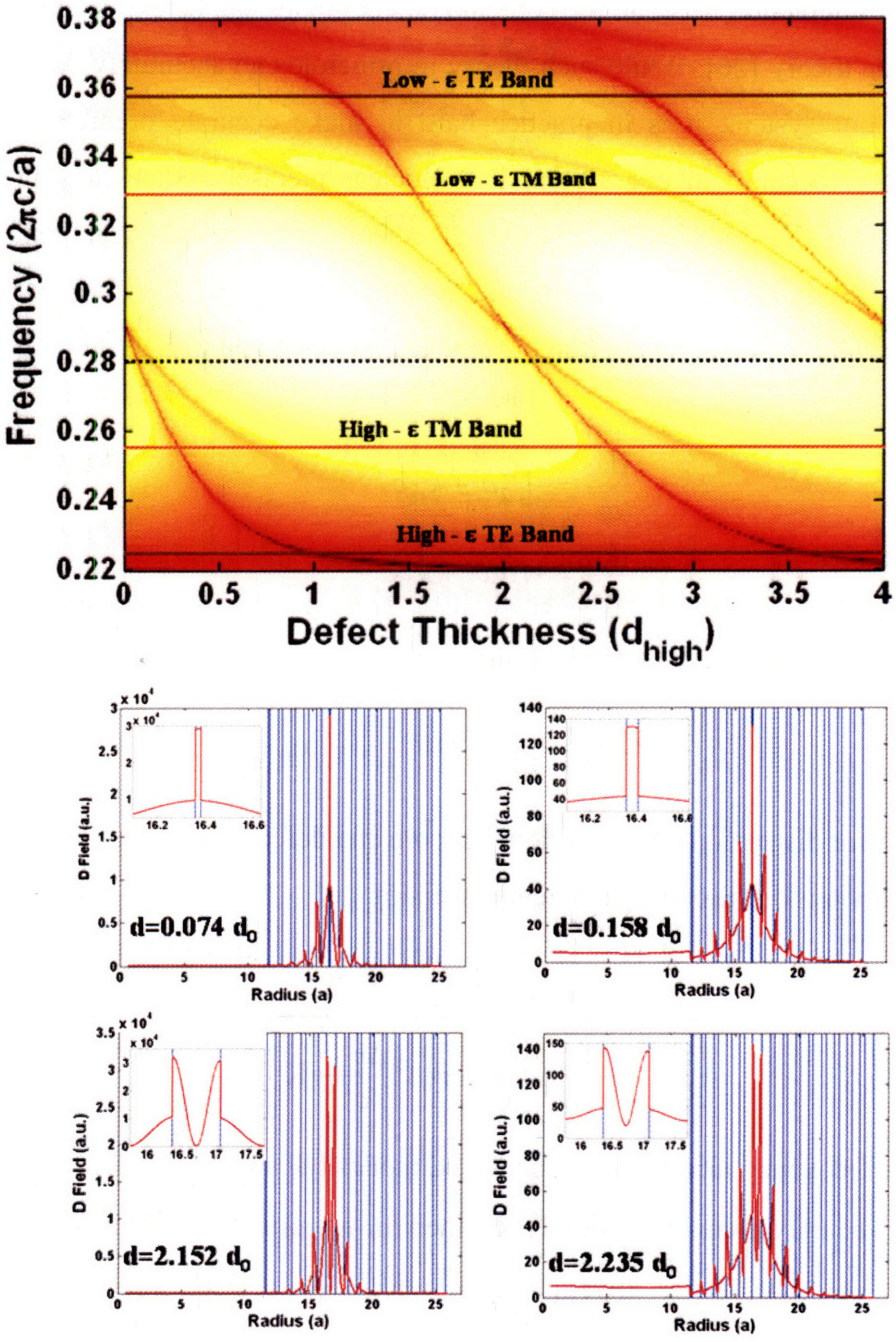

Figure 1.11: Upper panel depicts the energy behavior of both the TE- and TM- defect states for varying thicknesses of the defect layer. The weaker confinement of the TM-defect mode is expressed by the broader

spectrum when compared to the TE-defect. Also, it is evident that the TM (TE) defect modes exist only within the TM (TE) gap. Lower panel shown the D-field intensity distribution for ω=0.28.

1.3.7 The interaction picture via mode-coupling theory

Analytically the interaction between the core and defect modes can be explained in terms of coupled-mode theory [26]. While such theory in principle can accurately describe the interactions of our system, it is in practice hard to make accurate predictions about dispersion values, because in our system it is unclear precisely what constitutes the uncoupled systems. Nevertheless, coupled-mode theory may be of great benefit for predicting changes in dispersion values due to modifications to the fiber structure. Explicitly in the limit of weak interaction the coupled mode equations between a core and a defect mode

$$\begin{aligned} \frac{da_1}{dz} &= -i\beta_1 a_1 + \kappa_{12} a_2 \\ \frac{da_2}{dz} &= -i\beta_2 a_2 + \kappa_{21} a_1 \end{aligned} \tag{1.15}$$

The new eigenvalues of the coupled system are

$$\beta_{\pm} = \frac{\beta_1 + \beta_2}{2} \pm \sqrt{\left(\frac{\beta_1 + \beta_2}{2}\right)^2 + \kappa_{12}\kappa_{21}} \tag{1.16}$$

By assuming linear dispersion curve for both the core and defect modes we can obtain the following expression for the coupled system dispersion

$$D = -\frac{\omega^2}{2\pi c}\frac{\partial^2 \beta}{\partial \omega^2} = \frac{\frac{\omega^2}{8\pi c}\Delta n^2 \mathrm{K}}{\left[(\omega-\omega_0)^2 \frac{\Delta n^2}{4c^2} + \mathrm{K}\right]^{3/2}} \tag{1.17}$$

where ω_0 is the frequency in which the uncoupled modes (β_1 and β_2) intersects, $\Delta n = n_{eff} - 1$ and $\mathrm{K} = \kappa_{12}\kappa_{21}$. The maximum dispersion is obtained for $\omega = \omega_0$ and it value is

$$\left|D_{\max}\right| = \frac{\omega_0^2 \Delta n^2}{8\pi c}\frac{1}{\sqrt{\mathrm{K}}} \tag{1.18}$$

The interaction bandwidth (the frequency range in which the dispersion drop to half the maximum value) is

(1.19) $$\Delta\omega_{1/2} \approx 1.53\frac{c}{\Delta n}\sqrt{\mathrm{K}}$$

Figure 1.12 shows a comparison between an exact calculation using the leaky mode technique and coupled-mode theory of a fiber with a defect in the 9th layer. The dispersion curve of both the core and defect modes of the uncoupled system was assumed to be linear. The waveguide dispersion was then calculated using Eq. 1.17

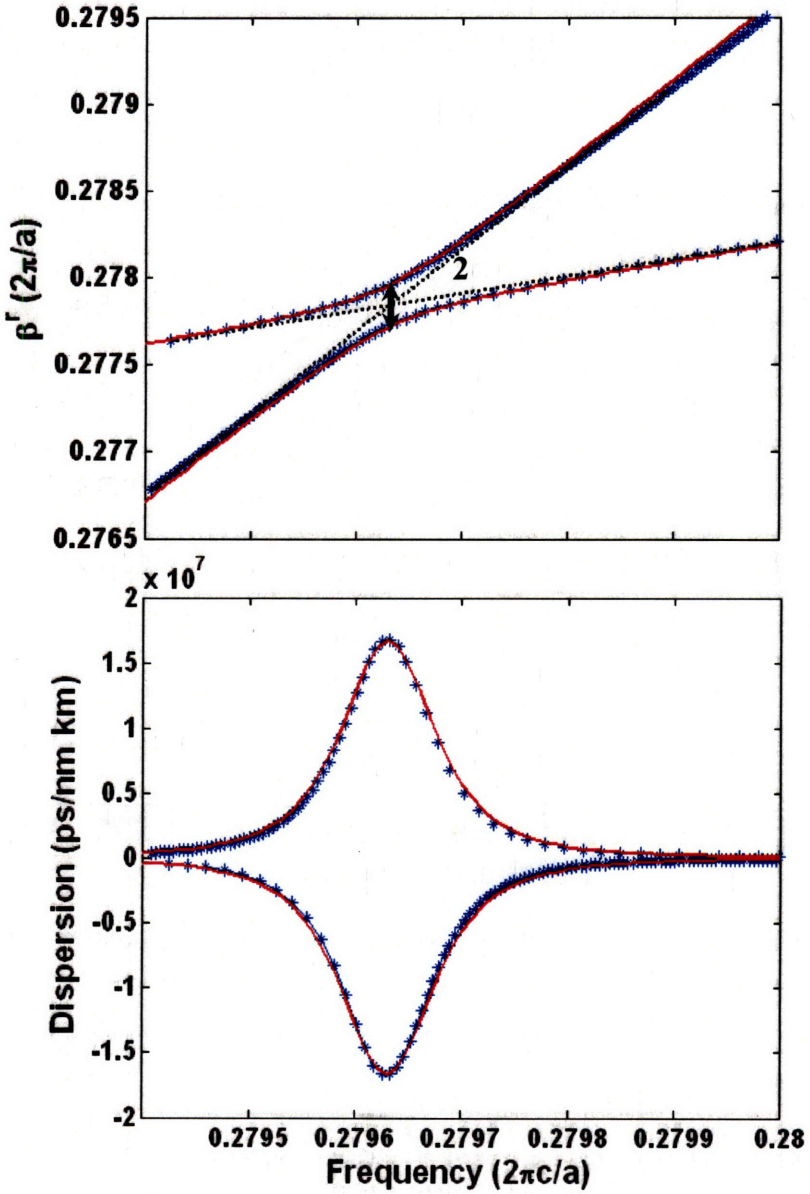

Figure 1.12: Comparison between coupled-mode theory and exact calculation using the leaky-mode technique. The upper panel shows the dispersion curve of a defect and a core mode in the vicinity of the interaction, while the lower panel shows their dispersion.

The magnitude of the frequency range over which the transformation takes place depends on the strength of the interaction between the fiber mode and the defect mode, or in other words the degree of overlap between the fields of the two modes. If the interaction is weak, which is the case for defect located far from the core and well within the bandgap, the frequency range over which the transition occurs will be narrow, resulting in sharp kinks in the dispersion relation for the given mode (Fig. 1.13). On the other hand, if the interaction is strong, the transition will take place over a broader frequency range and the kinks will be smoothed.

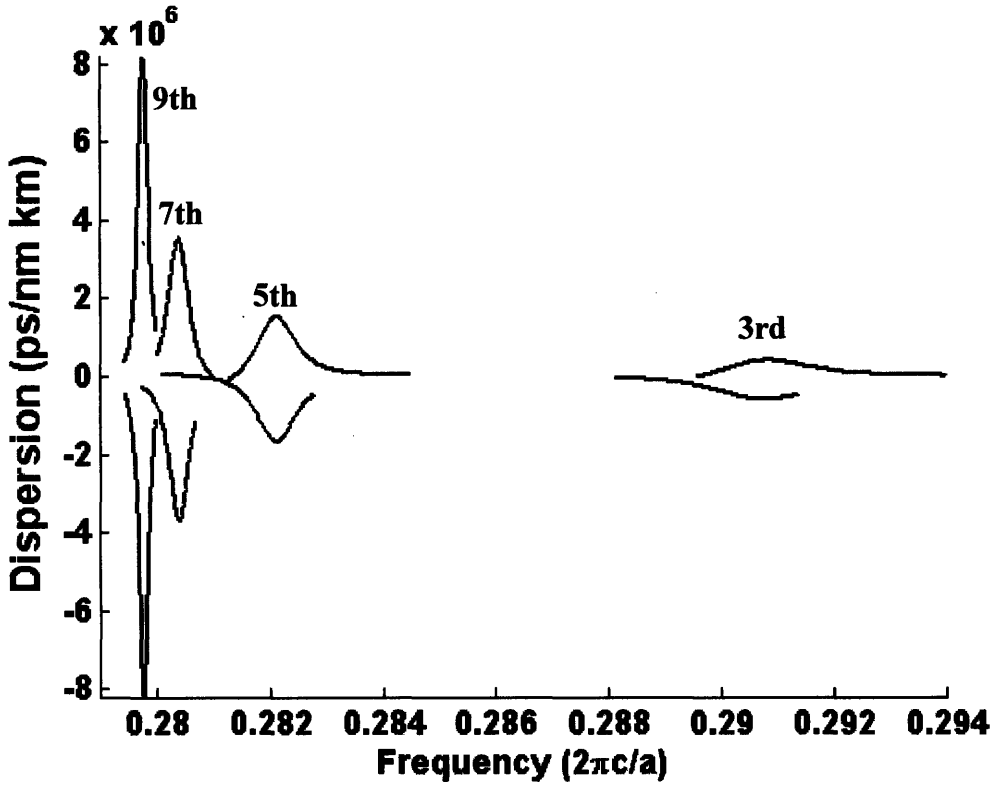

Figure 1.13: Dispersion calculations for defects located in the high-dielectric layer from the 3rd to the 9th layer. The coupling coefficient between the defect and the core modes for defect layer located away from the core is smaller and therefore the interaction takes place in a narrower frequency range and result in higher peak dispersion.

Independent of the interaction strength, the product of maximum dispersion and interaction bandwidth is only a function of the difference between the effective refractive indices of the defect and the core

$$|D_{\max}|\Delta\omega_{1/2} \approx 0.06\omega_0^2\Delta n \tag{1.20}$$

which is equivalent to the difference in the inverse group velocity. This result can be obtained by directly integrating over the dispersion curve [32] around the antocrossing

$$A = \int_1^2 D d\lambda = \int_1^2 \frac{\partial}{\partial\lambda}\left(\frac{1}{v_g}\right) d\lambda = \frac{1}{v_{g,1}} - \frac{1}{v_{g,2}} \tag{1.21}$$

This equation allows one to make simple predictions about the attainable dispersion characteristics by estimating the group velocities of the uncoupled system modes.

Mode coupling theory can also provide an insight into the losses of the coupled system by expanding the axial wavevector into the complex plain. The imaginary part of the wavevector is then proportional to the propagation loss of the mode along the axial direction

$$\beta_{\pm}^i = \bar{\beta}^i \pm \frac{\Delta n \Delta\beta^i(\omega-\omega_0)/c}{2\sqrt{(\omega-\omega_0)^2\Delta n^2/c^2 - \Delta\beta^{i2} + 4K}} \tag{1.22}$$

where $\bar{\beta}^i = \left(\beta_1^i + \beta_2^i\right)/2$ and $\Delta\beta^i = \beta_1^i - \beta_2^i$. At the interaction frequency, ω_0, where the dispersion is maximum, the losses of the coupled system are just the average of the uncoupled system.

In conclusion, we find that the degree of freedom in controlling the size and location of the defect can be used to tailor the dispersion properties of the fiber in intuitively predictable ways. Through the use of more complex defects, we can further modify the properties of the fiber. This could be accomplished by using multiple defects or by using a single defect that supports multiple defect modes. Using a rather large defect would enable the interaction with core-confined modes at multiple wavelengths.

The model for modal interactions presented here is only exact in the limit of weak interactions. For systems with stronger interactions between the modes it is imprecise to

consider the fiber and the defect as two separate systems whose resulting band diagram is the sum of the band diagram of the fiber and the defect separately. Furthermore, the simultaneous interaction between the defect and multiple bands may also alter the entire band diagram. In those cases, the real band diagram for the fiber with a defect must be calculated using the exact method described in the previous section. Nevertheless, the qualitative features of the anticrossing model remain.

2 Mode Decomposition for optical Waveguide

2.1 Introduction

Eigenmode decomposition of the field at the output of waveguides can provide fundamental insights into the nature of electromagnetic-wave propagation. The comparison of the modes present at the input to those exiting the structure enables the elucidation of loss mechanisms on the one hand and quantitative analysis of modal coupling on the other. The prospect of performing modal decomposition is of importance to several recent experimental efforts in atom guiding [7], high-harmonic generation in atomic gases [8], supercontinuum generation [9], and others. Nevertheless, a practical route to comprehensive modal decomposition, one that yields the full complex expansion coefficients of the vectorial field in the eigenmode basis, has not yet been achieved. Here we introduce a novel, rapidly converging, method based on the phase-retrieval algorithm together with intensity measurements at two planes, that yields a unique modal decomposition. An experimental validation is performed by decomposing the guided field in a photonic bandgap fiber. Both the amplitudes and phases of the 16 lowest-energy vectorial modes are obtained. The efficient convergence enables, for the first time, the quantitative analysis of bend-induced interactions in a many-mode system.

The objective of a non-interferometeric modal decomposition is to use intensity measurements and *a priori* knowledge of the waveguide eigenfunctions in order to deduce the weight of each mode at the output of the waveguide. Figure 2.1 depicts an example in which the modal content of an intensity pattern at the output of a PBG fiber is decomposed into three eigenmodes. While the eigenfunctions, e_n, can be calculated using the leaky-mode technique described in the previous chapter, to obtain the complex expansion coefficients, c_n, information on the (complex) field distribution of the measured intensity is necessary. With complete information of the field, $E_t = \sum_n c_n e_n$ in hand, c_n can be obtained by simply projecting the total field E_t onto the known eigenmodes e_n of the waveguide.

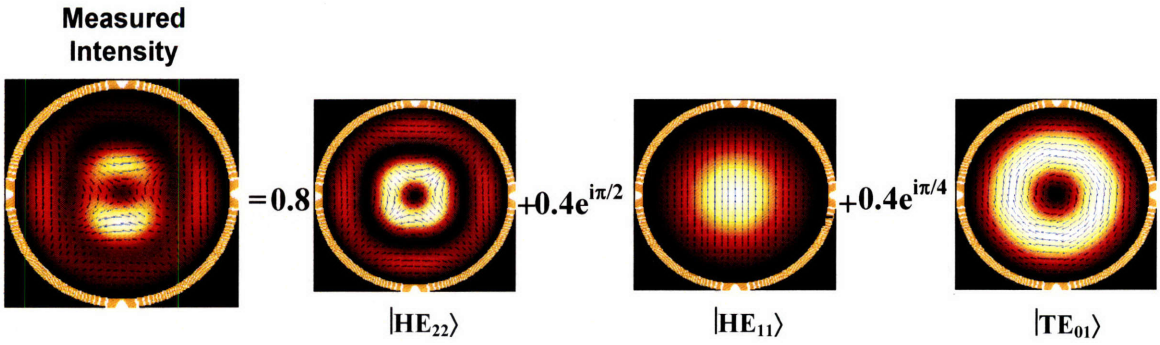

Figure 2.1: The objective of mode decomposition is to extract the expansion coefficients of the eigenfunctions from measured intensity distributions. The eigenfunctions can be calculated by solving the eigenvalue problem of the given waveguide structure.

Indeed, research on the transmission properties of waveguides supporting a multiplicity of modes spans many decades, from millimeter waves in the seminal work of G. C. Southworth in the 1930s [27] through ultraviolet transmission [28] in recent experiments. Modal decomposition approaches based on single-intensity measurements in the Fourier plane have been known (Refs. [29,30], for example). It is important to note that without any other a priori known constraints of the complex field distribution, the solution of such an inverse problem is not unique [31-34]. An example for such ambiguity is demonstrated in Fig. 2.2 where we plot the measured intensity at the output of a PBG fiber. Two possible amplitude decompositions (amongst many other) are provided, both of which yield a reconstruction that fits the measured intensity distribution.

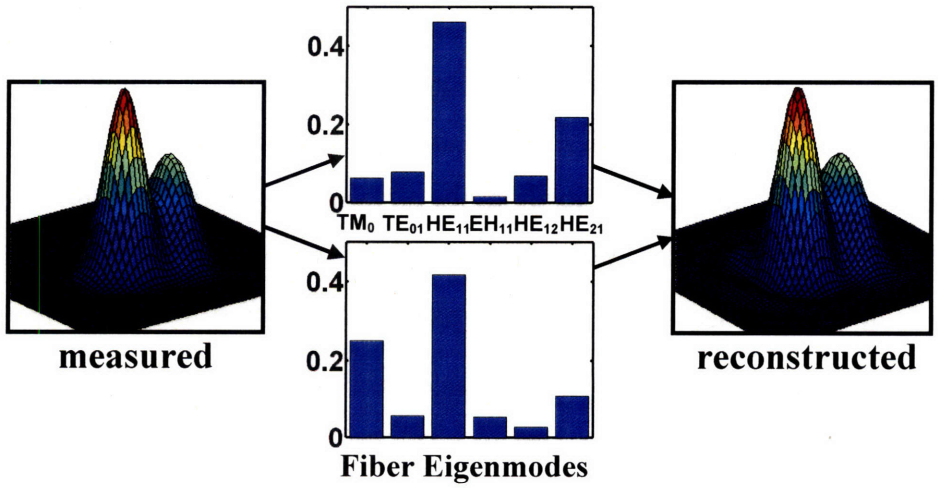

Figure 2.2: amplitude decompositions, in the waveguide eigenmode basis, for a far-field intensity measured at the waveguide output. Both yield a reconstruction that fits the measured intensity.

2.2 On the Uniqueness of Phase Retrieval Reconstructions

The above exemplify a general problem that arises in many phase retrieval problems: is the a priori knowledge given on the object (e.g. its support) together with intensity measurements sufficient to obtain a unique solution? The aim of this section is to find the necessary conditions for a unique reconstruction of an object given partial information on its Fourier transform (the far-field of the object). Although there is a one-to-one correspondence between a signal and its Fourier transform, there are many applications in which some of the Fourier domain information is either degraded or missing (usually phase information). In order to restore the signal, therefore, it is desirable to either restore or recover the missing spectral information. The primary problem of concern in this chapter is recovery of the phase of the Fourier transform given the magnitude. Clearly, in the absence of any underlying signal model or constraints, the loss of phase information of a complex function is irreversible. Surprisingly however, under some fairly general conditions it is possible to recover a signal from its magnitude [35]. In fact, for a useful class of signals it is almost always possible to recover one from the other; i.e., the phase and the magnitude constitute redundant pieces of information. The recovery of spectral phase information from only spectral magnitude information, generally referred to as the phase retrieval problem, arises in a variety of different contexts and applications. In x-ray crystallography, for example, the molecular structure of a crystal is to be inferred from the observed diffraction pattern of x-rays [36]. Although the diffraction pattern is related to the scattering density of the crystal by a Fourier transform, only the intensity of the diffraction pattern may be measured. Since knowledge of the phase of the diffracted wave is indispensable for determination of the crystal structure, the phase retrieval is particularly important. A similar problem arises in optical and electron microscopy when, for example, the index of refraction of a thin object or the height distribution of a surface is to be determined from the intensity of the wave distribution in the image plane or some other plane in the microscope [37]. Again, in order to determine the object structure, phase information of the wave is required.

2.2.1 The fundamental theorem of algebra and irreducible polynomials

In each of the applications above as well as in the discussions which follow, there are two distinct sets of problems. These are the problems of synthesis and reconstruction. The synthesis problem is concerned with the determination of a signal, such as an image, which is consistent with the known constraints. The reconstruction problem, on the other hand, is concerned with the *unique* recovery of a signal given a partial Fourier domain description along with a signal model or asset of signal constraints. Here there are separate issues related to the conditions under which exact reconstruction is theoretically possible and the development of practical algorithms for performing the reconstruction. We consider here signals with finite support, therefore, for convenience it will be assumed without any loss in generality that the discrete signal $x(m,n)$ is zero outside the rectangle $0 \leq m < M$ and $0 \leq n < N$. In such case $x(m,n)$ will be said to have support $R(M,N)$. It is important to note that a one-dimensional (1-D) sequence with finite support $R(N)$ has a z-transform which is polynomial in z^{-1} of degree $N-1$. Since the *fundamental theorem of algebra* states that any polynomial in a single variable may always be uniquely factored into a product of first-order polynomials, it follows that any 1-D sequence with support $R(N)$ has a z-transform which may be written in the form

$$X(z) = \sum_{n=0}^{N-1} x(n) z^{-n} = \alpha z^{-n_0} \prod_{k=1}^{p} A_k(z) = \alpha z^{-n_0} \prod_{k=1}^{p} (1 - a_k z^{-1}) \tag{2.1}$$

The polynomials $A_k(z)=(1-a_k z^{-1})$ are the irreducible factors of $X(z)$ and the constants a_k are the zeros of $X(z)$. As a result, any 1-D signal with finite support is uniquely characterized (to within a scale factor) by the distribution of the zeros of its z-transform. In other words, a 1-D sequence is uniquely defined to within a scale factor by the coefficients a_k and the value of n_0.

The z-transform of a 2-D sequence $x(m,n)$ with support $R(M,N)$ is a polynomial in the two complex variables z_1 and z_2. Therefore, $X(z_1,z_2)$ may always be written uniquely (to within factors of zero degree) as a product of polynomials which are irreducible over the field of complex numbers

$$Z(z_1, z_2) = \sum_{m=0}^{M-1} \sum_{n=0}^{N-1} x(m,n) z_1^{-m} z_2^{-n} = \alpha z_1^{-n_1} z_2^{-n_2} \prod_{k=1}^{p} A_k(z_1, z_2) \tag{2.2}$$

where α is a real number and n_1 and n_2 are nonnegative integers. The polynomials $A_k(z_1,z_2)$ are the irreducible factors of $Z(z_1,z_2)$. Therefore, for both 1-D and 2-D signals, the z-transform may always be written as a product of irreducible factors. Important difference follows from the fact that the fundamental theorem of algebra is not valid for polynomials in two or more variables. In particular, whereas this theorem guarantees that the irreducible factors of 1-D polynomials will always be of first order, the irreducible factors of 2-D polynomials may be of arbitrary large degree.

Since polynomials in two variables of arbitrary large degree may be irreducible, it is of interest to determine the likelihood that an arbitrary 2-D signal with support $R(M,N)$ will have an irreducible z-transform. More specially, given an arbitrary signal $x(m,n)$ with support $R(M,N)$, is it more likely that $X(z_1,z_2)$ is reducible (factorable) or irreducible? In order to address this question, note that it is possible to make a correspondence between the polynomials which are z-transforms of sequences having support $R(M,N)$ and an ordered sequence (vector) of length $L=M\times N$ real numbers. This correspondence consists of arranging the coefficients $x(m,n)$ of the polynomial $X(z_1,z_2)$ into a vector in some fixed order. Since the set of reducible polynomials may be identified in a one-to-one manner with a subset S of the L-dimensional Euclidean $\boldsymbol{R}^L$, then it is possible to determine the Lebesque measure of the set S. It has been shown that this set has a measure zero [38]. Therefore, it follow that "almost all" polynomials in two or more variables are irreducible.

Since the set of reducible polynomials is a set of measure zero, it is of interest to determine whether geometrically it is sparse or dense. In particular, if it is dense in the set of all polynomials then it would be possible to find, for any given irreducible polynomials, a reducible polynomial which is arbitrary close to it. Practically speaking, this would imply that the irreducibility property of a given polynomial is extremely sensitive to noise since arbitrary small perturbations of the coefficients may lead to reducible polynomial. Fortunately this is not the case and it was found that the set of reducible polynomials is sparse [39]. In the reminder of this section we make use of the irreducibility of the z-transform in 2D to prove the uniqueness of the solution to the phase-retrieval problem.

2.2.2 Uniqueness of a signal with respect to its Fourier transform intensity

In most applications a shift, inversion, or reflection of the signal are of no concern since it is the relative amplitudes of the various samples within the signal that are of primary importance. Therefore, two signals will be said to be equivalent if they are related to one another by the combination of the previous relations. Excluding these trivial ambiguities, it is still not positive to uniquely define a signal in terms of its spectral magnitude because it is always possible to convolve a signal with an arbitrary *all-pass* signal (one which has a Fourier transform with unit modulus) to obtain another signal with the same spectral magnitude.

Let $x(n)$ be a 1-D sequence with $X(e^{i\omega})$ it Fourier transform having a support $R(N)$. Note that for any sequence $x(n)$ it is always possible to find another sequence which has a Fourier transform with the same magnitude by simply convolving $x(n)$ with all-pass sequence $g(n)$ where

$$y(n) = x(n) * g(n) \quad ; \quad \left|G(e^{i\omega})\right| = 1 \tag{2.3}$$

it is important in the phase retrieval problem to examine the z-transform of an all-pass sequence. Note that if $g(n)$ is an all-pass sequence, then by definition $\left|G(e^{i\omega})\right|^2 = 1$ and since $g(n)$ is real $G(e^{i\omega})G^*(e^{-i\omega}) = 1$ and therefore $G(z)G^*(1/z^*) = 1$. It follows that the singularities of $G(z)$ must occur in conjugate reciprocal pole/zero pairs, so that if $G(z)$ has a zero (pole) at z=a the G(z) must also have a pole (zero) at z=1/a*. Therefore, if g(n) is an all-pass sequence then its z-transform must be of the form

$$G(z) = z^{-(n_0+p)} \prod_{k=1}^{p} \frac{1 - a_k z^{-1}}{z^{-1} - a_k^*} \tag{2.4}$$

Conversely, any rational all-pass signal has a z-transform which may be written in the form given in Eq, (2.4). Therefore, it follows that the effect of convolving a sequence $x(n)$ with an all-pass sequence $g(n)$ is to with add or delete conjugate reciprocal pole/zero pairs (all-pass factors), or to replace a zero (pole) at $z=a$ with a zero (pole) at $z=1/a^*$. With $x(n)$ a 1-D finite-length sequence with support $R(N)$, its z-transform is a product of $(N-1)$ linear factors of the form $(1-a_k z^{-1})$. If any of these factors are replaced with a factor of the form $(z^{-1}-a_k^*)$, then the corresponding sequence will still have a support $R(N)$ and the magnitude of its Fourier transform will be unchanged. Clearly, the same result applies

to the poles. Therefore, in order to guarantee a unique solution, it is necessary to place constraints on x(n) in order to resolve the ambiguity about the side of the unit circle on which each pole and each zero lies.

Note that if *x(n)* has a z-transform with all of its singularities (poles and zeros) inside the unit circle (minimum phase), then convolution with an all-pass sequence will always produce a sequence which has at least one singularity outside the unit circle. Similarly, if all of the singularities are outside the unit circle (maximum phase) then the convolution with an all-pass sequence will produce a sequence with at least one singularity inside the unit circle. Therefore any minimum or maximum phase sequence is uniquely defined (to within a sign and delay) by the magnitude of its Fourier transform.

For the case of 2-D sequences by following the same development it follows that two 2-D sequences have Fourier transforms with the same magnitude if and only if one is related to the other by convolution with an all-pass sequence. As in the case of 1-D sequences, any 2-D all-pass sequence *g(m,n)* has a z-transform satisfying

$$G(z_1, z_2)G^*(1/z_1^*, 1/z_2^*) = 1 \tag{2.5}$$

Therefore, it follows that any all-pass sequence which has a rational z-transform must have a z-transform of the following form

$$G(z_1, z_2) = \prod_{k=1}^{P} \frac{H_k(z_1, z_2)}{H_k^*(1/z_1^*, 1/z_2^*)} \tag{2.6}$$

Just as in the 1-D case, multiple solutions to the 2-D phase retrieval problem generally exist due to the possibility of zero contour flipping. Specifically, with *x(m,n)* a 2-D sequence with support *R(M,N)*, its z-transform may be written as a product of *p* irreducible polynomials $A_k(z_1,z_2)$. If any of these irreducible factors are replaced with the factor $A_k^*(1/z_1^*, 1/z_2^*)$, then the resulting 2-D sequence will also have a finite support and the magnitude of its Fourier transform will be proportional to that of *x(m,n)*. Note, however, that if $X(z_1,z_2)$ is irreducible, then the only other sequences which have the same Fourier transform magnitude as *x(m,n)* are those which are related to *x(m,n)* by a linear shift, multiplication by -1, or by reflecting the sequence about the origin. We can than conclude that a 2-D sequence with finite support which has an irreducible z-transform is uniquely defined by the magnitude of the Fourier transform. Since most polynomials in two or more variables are irreducible it follows that almost all 2-D sequences with finite

support are uniquely defined by the magnitude of the Fourier transform. Moreover, it can be showed that uniqueness still holds if only the magnitude of the discrete Fourier transform of $x(m,n)$ is known [40]

2.2.3 Considerations for complex object

Heretofore we assumed that the support of the object is known and finite and that the object is real (zero phases). However in many problems the objects may be complex and the reconstruction of both the amplitude and the phase of the object are of interest. If the image is an arbitrary complex function, the phase problem has a multitude of solutions since one can associate any phase function with the measured intensity to generate a different image. Walther [41] appear to have been the first to recognize that the problem posed in this way does not correspond to any real physical situation. In any practical case, there are constraints on the form of the image. For example, in an optical system the image has finite support and is square integrable. In general, applying any phase function to the amplitude will produce an image that violates these conditions. The important uniqueness question is therefore: is there more then one phase function that gives an image that satisfies the given conditions? Walther [41] showed that in the 1-D case there are multiple, but countable, phase functions that lead to images with the correct support. He pointed out that nonnegativity could be expected to restrict the number of solutions further. The quite different situation in two dimensions appears to have been noted first for the general complex image by Barakat and Newsam [42] in the sense that a multiplicity of solutions is pathologically rare using the theory of complex variables. Uniqueness was demonstrated in a more practical sense using the concept of zero sheets [43,44]. In 2-D, the Fourier transform of the image can be analytically continued into a space with complex dimensions, denoted by $F(z_1,z_2)$. Considering z_1, say, fixed, then $F(z_1,z_2)$ has point zeros in the z_2 plane. As z_1 is varied, these zeros migrate along smooth 2-D surfaces (zero-sheets) since F is analytic. Since in 2-D the z-transform of the image is almost always an irreducible polynomial, these sheets actually form a single sheet and the point zeros cannot be treated (and flipped) independently as in the 1-D case. Only in special cases, that occur with probability zero) do the zeros form more then one sheet. Since $|F(z_1,z_2)|^2$ has two factors, it contains two zero sheets, one corresponding to $F(z_1,z_2)$

and one for $F^*(z_1^*,z_2^*)$. Although 2-D surfaces in a 4-D space almost never intersect, these two surfaces, being interdependent, intersect whenever $(z_1,z_2)=(z_1^*,z_2^*)$, i.e., wherever one of them crosses the real axis. Since the Fourier transform is an entire function, continuity of the first derivative can be applied to distinguish between the two zero sheets. Algorithms have been developed and implemented to separate the zero sheets and reconstruct the image. However, these algorithms have been applied only to simulated data with small images, since they are sensitive to noise and computationally intensive [43,44].

Based on this underlying theory, several other attempts have been made to devise a complex image reconstruction algorithm that is both noise tolerance and computationally efficient [45-48] each of which requires either oversampling or additional constraints on the object.

2.3 The Mode Decomposition Algorithm

The previous chapter showed that while theoretically it is possible to obtain a unique reconstruction of a complex object from only the 2-D Fourier intensity, in practice phase retrieval algorithms are required to impose additional constraints in order to reconstruct the correct complex object with reasonable noise tolerance. Unlike x-ray microscopy and reconstruction problems in astronomy, mode decomposition for optical waveguides allows one to measure both the intensity at the output of the waveguide as well as in the diffracted Fourier plane. The problem of phase retrieval, given both the object intensity and the Fourier intensity, was treated first using the Gerchberg-Saxton (GS) algorithm [31]. This algorithm is known to be a particularly successful method for phase retrieval that results in a unique as well as noise tolerant solution [33] by iterating back and forth between the two-dimensional (2D) field distributions of the object and the Fourier planes. This algorithm requires however the calculations of both the Fourier transform and its inverse in any iteration and thus might be quite computationally intensive. The decomposition of a field in a waveguide, on the other hand, requires the reconstruction of only the mode expansion coefficients since the field distribution is constrained to be a linear superposition of the waveguide eigenfunctions that can be determined from the waveguide structure. The only unknowns are thus the expansion coefficients in this

superposition, rather then the set of pixels in the image [49]. By mapping the problem from the 2D image space into this abstract space of waveguide eigenmodes we reduce significantly the number of independent variables, and also completely remove the dependency on the number of pixels in the iterative process. Furthermore, since higher-order modes in multimode waveguides tend to have higher losses, one can set a modal cutoff, depending on the specifics of the waveguide, and deal with only a small number of modes. It is noteworthy that this approach applies to *any* waveguide, whether or not it possesses any symmetry.

In Ref. [34], Fienup established that iterative methods, such as the GS algorithm, are related to gradient search methods. Following suit, we construct our algorithm to minimize an error function with respect to a set of independent variables representing the expansion coefficients of a basis set constructed of the waveguide eigenmodes. Since the vectorial aspect of the waveguide modes is essential we define four squared-error functions for two orthogonally polarized components in both the near- and far-fields

$$\Delta_{a,b} = \int_{core} \left[I_r^{a,b}(r) - I_{me}^{a,b}(r) \right]^2 dA \tag{2.7}$$

where $a = 1, 2$ defines the plane of measurement (near- or far-field), $b = 1, 2$ defines one of two perpendicular polarizations, I_{me} is the *measured* intensity, while I_{r} is the intensity of a *reconstructed* estimate of this field. We then define an overall error function $\Delta = \sum_{a,b} \Delta_{a,b}$. We used an unconstrained optimization routine that employs the subspace trust region method from MATLAB© to perform the minimization of this error function over the space of expansion coefficients.

If the electric and magnetic field vectors of the nth waveguide mode are $\vec{\varphi}_n^{(E)}$ and $\vec{\varphi}_n^{(H)}$, respectively, and their scalar projections in a fixed direction are e_{n} and h_{n}, then the total field vectors are $\vec{E}(r) = \sum_n c_n \vec{\varphi}_n^{(E)}(\mathbf{r})$, $\vec{H}(r) = \sum_n c_n \vec{\varphi}_n^{(H)}(\mathbf{r})$, where $c_n = |c_n| e^{i\psi_n}$ are the expansion coefficients. Using this notation, the reconstructed intensity is $I_r(\mathbf{r}) = \frac{1}{N} \mathrm{Re} \sum_{i,j} c_i c_j^* e_i(\mathbf{r}) h_j(\mathbf{r})$, where N is a normalization factor, and we note that e_i

and h_j may be chosen to be real functions in two dimensional structures. By rearranging, we may write any of the four error functions, $\Delta_{a,b}$, as follows

$$\frac{1}{N^2}\sum_{ijpq} c_i c_j c_p^* c_q^* \Lambda_{ijpq} - \frac{2}{N}\sum_{ij} c_i c_j^* \Gamma_{ij} + P \tag{2.8}$$

where P is the integral over space of I_{me} squared, $\Lambda_{ijpq} = \int e_i(\mathbf{r}) e_j(\mathbf{r}) h_p(\mathbf{r}) h_q(\mathbf{r}) dA$, and $\Gamma_{ij} = \int I_{me}(\mathbf{r}) e_i(\mathbf{r}) h_j(\mathbf{r}) dA$. The tensors Λ and Γ may be contracted significantly by exploiting the symmetry of the waveguide modes. Furthermore, the tensor elements are computed once prior to the optimization of Δ, leading to a pixel-invariant iterative process.

For the sake of demonstrating a concrete application of our algorithm, we restrict ourselves for the remainder of the paper to circularly symmetric waveguides. The cylindrical structure results in three conserved quantities that characterize the vectorial eigenmodes: the frequency ω, the axial wave vector (eigenvalue) k, and the angular momentum m. For a large core fiber (with respect to the transmitted wavelength) the components of an eigenfunction with eigenvalue k can be expressed as $R_{ml}(r)\cos(m\theta + \phi)\exp\left[i(kz - \omega t)\right]$. The phase ϕ, which we henceforth call the degeneracy phase, is required by the degeneracy of the $\sin m\theta$ and $\cos m\theta$ solutions of the wave equation. Modes with m = 0 are non-degenerate TE and TM, while modes with non-zero m are doubly degenerate hybrid modes. The radial factor, $R_{ml}(r)$, can be obtained using the transfer-matrix method [18].

2.4 Experimental Mode Decomposition for a PBG Fiber

We confirmed the validity of this algorithm by applying it to the problem of mode decomposition in a multimode cylindrical photonic bandgap fiber [5]. The fiber (Fig. 2.3) has a 533 μm-diameter hollow core surrounded by a multilayer structure that results in a fundamental bandgap ranging from 9.5 to 11.2 μm. Since the core diameter is approximately 50 wavelengths, the fiber is highly multimoded and can in theory support thousands of modes. In practice, however, the strong mode-filtering mechanism

characteristic of this fiber [18], as well as the input coupling, result in only a few low-loss, low-energy modes remaining with considerable power after one meter of fiber. We used a linearly polarized CO_2 laser at 10.6 μm to excite the fiber, and carried out three sets of measurements that we refer to as the long-fiber, bent-fiber, and short-fiber cases (Fig. 2.3e). In the long-fiber case, we carried out measurements for a 1.5-m long straight fiber; in the bent-fiber case, the first 1.1 m of the same fiber was kept straight while the rest is bent (radius of curvature R_b = 0.3 m, length d = 0.4 m); and in the short-fiber case, the bent part was cut off, leaving a 1.1-m-long straight fiber. In each case we captured the near-and far-field intensity images (using 4-f and 2-f lens configurations, respectively) of two orthogonal polarizations with a Spiricon pyroelectric camera preceded with a linear polarizer.

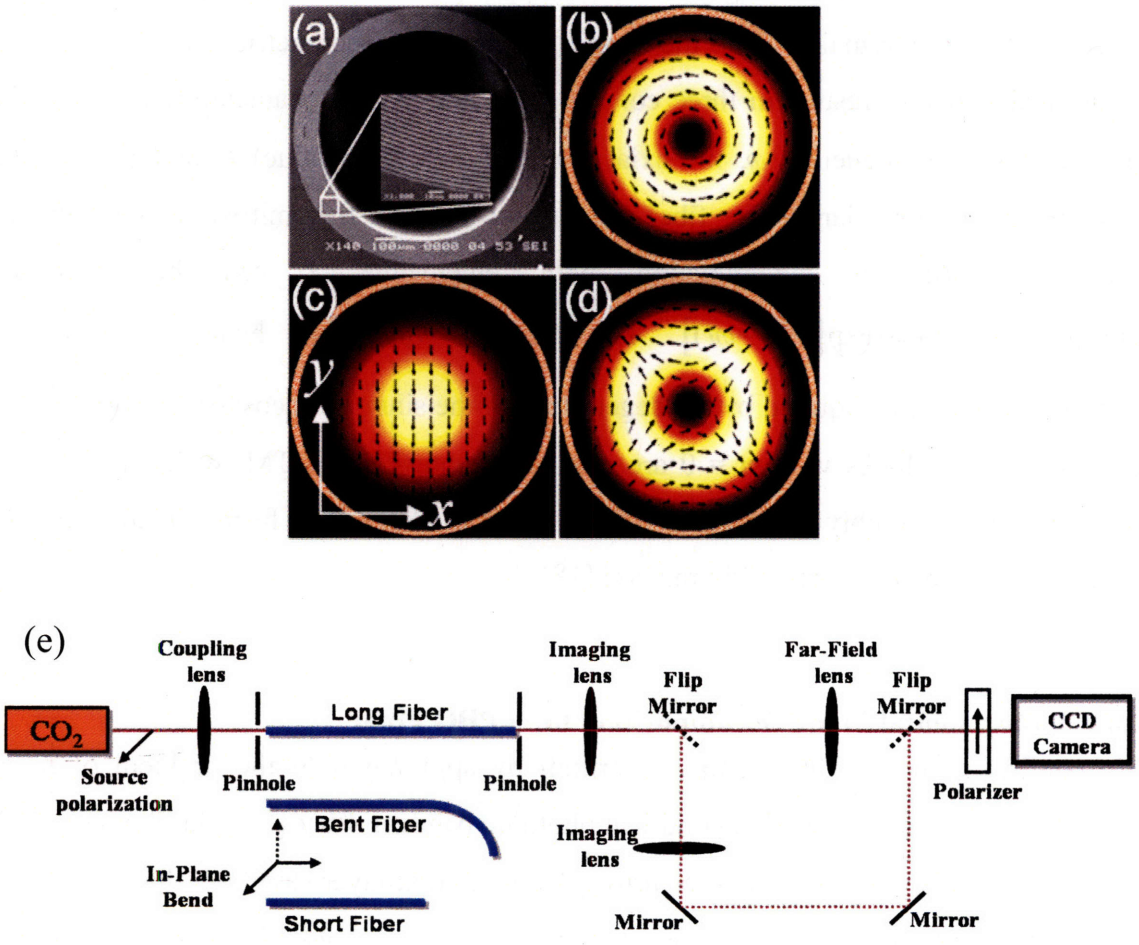

Figure 2.3: a, SEM image of the PBG fiber cross section. Calculated intensities and vector field distributions for the **b,** TE01, **c,** HE11 and **d,** HE21. All plotted with the degeneracy phases set to 0. **e,** experimental setup for mode decomposition.

We performed the decompositions using a basis consisting of the 16 lowest-energy modes with angular momentum $m<4$. We checked convergence by increasing the number of eigenfunctions in the chosen basis to incorporate higher order modes and found no measurable improvement. The fidelity of the decomposition results to the measured intensity distributions is demonstrated in Fig. 2.4, for the short-fiber case. To further confirm the validity of this decomposition, all measurements were repeated for five distinct pairs of orthogonal polarization directions, and the correlation coefficients between the decomposition results exceeded 0.98. To verify convergence of the error-function to its global minimum, we repeated the process for 50 different random initial conditions, and the correlation between the results was greater then 0.999.

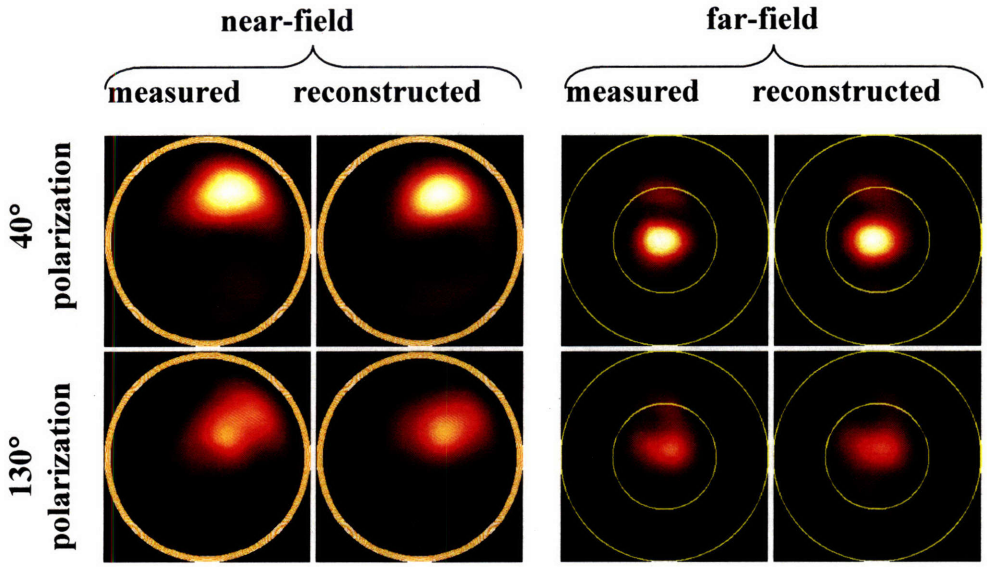

Figure 2.4: Measured and reconstructed intensity distributions for the short-fiber case. The circle in the near-field images represents the location of the fiber core-cladding interface. The two circles in the far-field images represent the location of the first and second zeros of a far-field image of a uniformly distributed field having the shape and extent of the fiber core.

2.4.1 Results for the uncoupled case

Numerous salient features of wave propagation in the fiber may be discerned from the decomposition results of the three cases by virtue of unveiling the values for the

amplitudes $|c_n|$, relative phases ψ_n, and degeneracy phases ϕ_n of the guided modes. We note that phase values are not reliable for modes with negligible amplitudes. We start by examining the short-fiber case (Fig. 2.5), in which HE_{11} is the dominant mode (due to the strong overlap between the laser Gaussian-beam profile and the HE_{11} profile as shown in Fig. 2.3c), with contributions from other modes, most significantly TE_{01} and HE_{21}. The polarization of the output field was found to conserve the horizontal (x) polarization of the input field, as expected by the circular symmetric structure. Inspection of the values of $|c_n|$, ψ_n, and ϕ_n for the 3 above mentioned dominant modes confirms this experimental observation. This can be shown by first noting that in a large-core fiber the degeneracy phase ϕ_n of any mode manifests itself as a rotation of the mode field lines by an angle ϕ_n. In the case of HE_{11}, $\phi_{HE11} \approx \pi/2$ [upper panel of Fig. 4(a)], corresponding to a rotation of the field lines (Fig. 2.3c) to the horizontal. The TE_{01} and HE_{21} modes (Fig. 2.3b and 2.3d), on the other hand, have y-polarized components, but it is straightforward to show that the relative amplitude, phase, and degeneracy phase revealed by the decomposition ensure their cancellation.

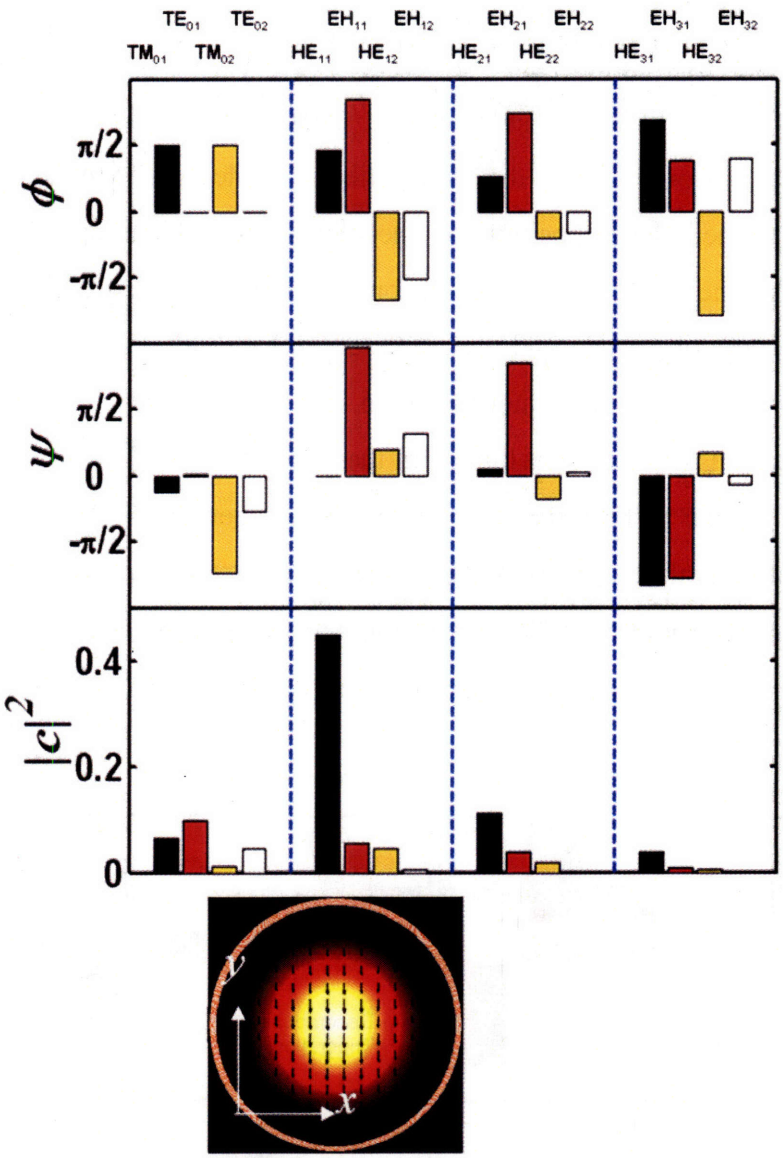

Figure 2.5: Complete modal decomposition of the 16 lowest-energy modes, with angular momentum $m < 4$ for the short-fiber case. The lower, middle, and upper panels depict the expansion coefficients modulus squared $|c_n|^2$ (normalized such that $\Sigma|c_n|^2 = 1$), the relative phases ψ_n, and the degeneracy phases ϕ_n, respectively.

In a straight fiber, the orthogonal modes propagate with no mutual interaction, thus, any changes in the modal distribution along its length are due to losses and dispersion. The amplitude of a mode in the output of the long fiber is related to that of the same mode in the short fiber by a factor of $\exp(ik_n - \alpha_n)d$. Moreover, in the absence of structural perturbations we expect the degeneracy phases ϕ_n to retain their values. We theoretically

calculated the axial-wavevectors k_n and loss coefficients α_n for our structure using the leaky-mode technique [16]. Figure 2.6a depicts a comparison between two modal decompositions for the long fiber for modes with $|c|^2>0.05$. The first is obtained directly from measurements performed on the long fiber, while the second uses the experimentally determined decomposition of the short fiber as initial condition for numerically evaluating the decomposition of the long fiber. The good agreement between the two cases is easily observed, and the correlation for both the amplitudes and degeneracy phases was found to be greater then 0.95. We attribute the small variations in the results to deviation of the fiber structure from the ideal cylindrical structure assumed by our theoretical model. While the amplitudes and degeneracy phases are quite insensitive to such structural deviations, accurate theoretical determination of the rapidly varying phases ψ_n require precise knowledge of both the wavevectors k_n and the absolute fiber length. A detailed experimental study on relative-phase reconstruction will be presented elsewhere.

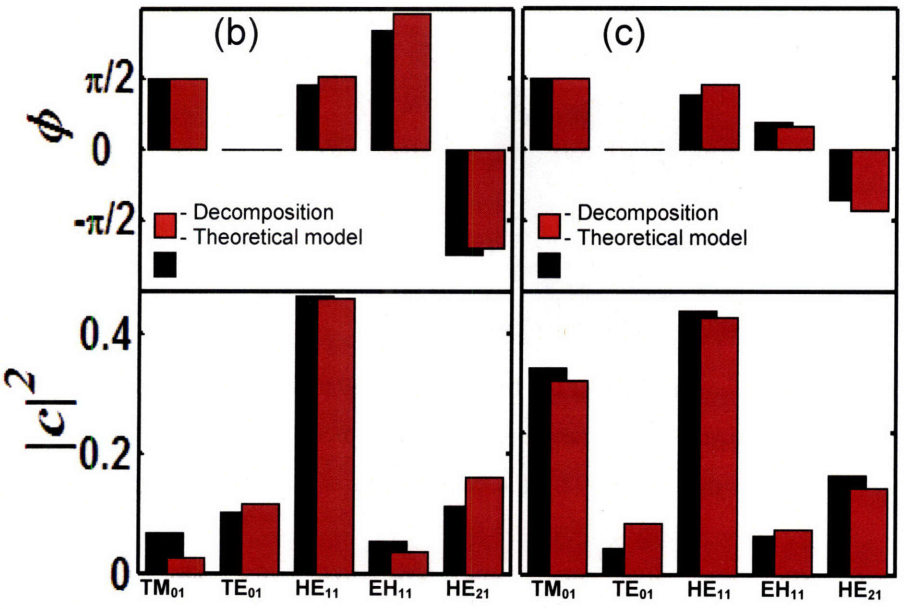

Figure 2.6 a, The decomposition results of the long fiber (red bars) and a theoretical estimation (black bars). **b,** The decomposition results of the bent fiber (red bars) and the calculated results based on a mode-coupling model (black bars). Both theoretical estimates shown in (b) and (c) use the results in (a) as initial conditions.

2.4.2 *Results for the perturbed system*

The rapid convergence of our scheme and complete phase and amplitude information allows for the study of systems with a large number of interacting modes as is the case in a waveguide bend. Here we compare the modal content in a bent fiber obtained by direct experimental observation and subsequent modal decomposition at the fiber output to the predicted output based on coupled mode theory assuming identical initial conditions established by the modal decomposition of a short fiber. Theoretically, bends with unchanged cross section and radius R_b much larger then the core radius, are treated as a perturbation to the fiber axis [18]. The field at the output of the bent fiber can then be represented by a linear superposition of the unperturbed fiber eigenmodes, with the coefficients satisfying:

$$\frac{dc_n}{dz} = ik_n c_n + i\sum_{n' \neq n} \gamma_{nn'} c_{n'} \tag{2.9}$$

where the matrix elements $\gamma_{nn'}$ representing the coupling between the n and n' modes and couples directly only those pairs of modes with $\Delta m = \pm 1$ [18], due to the nature of the perturbation. The degeneracy of modes with $m>0$ is lifted under this perturbation, giving rise to a change in the degeneracy phases. Furthermore, the first non-zero correction to the coefficients in perturbation theory is inversely proportional to $\Delta k_{nn'} = k_n - k_{n'}$, thus we expect only those modes that are close in k space to be strongly coupled. Evaluation of k_n for the various modes identifies TM_{01}, TE_{01}, and HE_{21} as the closest neighbors of HE_{11}. However, since the fiber bend was in the x - z plane, reflection symmetry around the y axis must be conserved. Consequently, the x-polarized HE_{11} will not couple to TE_{01} due to their different symmetry under reflection in the y axis (Fig. 2.3). We solve Eq. (2.9) numerically for the modes shown in Fig. 2.5, taking the decomposition results for the short-fiber case as initial conditions. Figure 2.6b depicts the solution of the coupled-mode equations thus obtained alongside the decomposition results for the bent-fiber case and good agreement is observed with correlation coefficients for both amplitudes and degeneracy phases greater then 0.96. The expected coupling to TM_{01} is clear, while the ostensibly weaker coupling to HE_{21} can be understood from examining the dependence of the solution of Eq. (2.9) on the length of the bend. The modes exchange power back and forth along the bend due to interference of the scattered waves, and the length of the bend

in our experiment fortuitously corresponds to a point at which the HE_{21} coefficient returns to its initial value. Lastly we note that if the polarization of the field lies in the plane of the fiber bend, the mode coupling results in a field that conserves the original polarization, otherwise energy is transferred to the orthogonal polarization. For that reason the HE_{11} mode retains its polarization along x, as indicated by ϕ_{HE11} (upper panel of Fig. 2.6b). On the other hand, the degeneracy phase for the HE_{21} mode, which has both *x*-polarization and *y*-polarization components (see Fig. 2.3d) changes in order to maintain the overall *x*-polarization while accommodating changes in the amplitudes of the other modes. The modal content as obtained by the two independent approaches is in close agreement as evident in Fig. 2.6b.

2.5 Mode synthesis

2.5.1 Objective

In the first chapter we studied the transmission properties of the few lowest energy modes in a large core PBG fiber. In particular, it has been predicted that the zero-angular-momentum mode TE_{01} will have the lowest transmission losses. The reliable and controllable transmission of TE_{01} mode in an optical fiber in the near infrared has not, to the best of our knowledge been previously reported. The TE_{01} mode has several unique advantages and features, most notably that it is completely circular symmetric, and hence truly non-degenerate (in contrast to the linearly polarized HE_{11} mode), thus alleviating polarization mode dispersion. Moreover, the transmission bandwidth of the TE_{01} mode is predicted to be wider than that of the HE_{11} mode. Furthermore, the ability to excite different core modes is expected to enhance our understanding of the propagation characteristics of the different modes of a PBG fiber. The ability to generate and excite the propagation of any mode will enable us to identify the mode with the lowest loss and further study its characteristics and related scaling laws. The challenge is to excite only the desired mode (or a superposition of modes). This can be done in two ways. The first is to generate the field of a given mode using spatial modulator and then couple it into the fiber. The second is to use perturbation to the fiber, such as fiber bands, that would couple energy to the desired modes. Here we focus on the first technique.

2.5.2 Mode Synthesis using Programmable Phase Modulator

This technique involves the use of a Programmable Phase Modulator (PPM). The PPM is an electrically-addressed phase modulator the employs an optical image transmitting element to couple an optically-addressed PAL-SLM (Parallel Aligned Nematic Liquid Crystal Spatial Light Modulator) with an electrically addressed intensity modulator. The PPM uses an LCD to allow computer control and also employs an optical system to eliminate diffraction noise originating from the LCD pixel structure. This unique configuration allows easy computer-controlled pixel manipulation.

We note however, that with a single PPM it is impossible to generate an arbitrary field distribution since only the amplitude or phase can be modulated at the same time, but not both. Additionally, in general, the PBG modes have more then one polarization component (vector field), while the PPM operates only one polarization component. In spite of these two restrictions, most of the interesting properties of the fiber modes can be studied from the linearly polarized HE_{11} mode, the azimuthally polarized TE_{01} mode and the radially polarized TM_{01}. Yet, we need to demonstrate that effective coupling for these three modes can be obtained by only phase modulation of a single polarization. Figure 2.7 depicts the coupling coefficients of two scalar beams with identical Gaussian amplitude distribution but opposite symmetry in phase. Fig. 13a shows that for uniform phase distribution the beam would couple mostly to the HE_{11} mode. By changing the phase symmetry of that beam, by introducing a π phase shift between two halves of the beam, the coupling is now mostly to the TE_{01} and HE_{21}. While this might not be an ideal coupling, in practice since the radiation losses of the HE_{21} are much higher then of the TE_{01}, after a short segment of fiber only the lower loss TE_{01} would survive.

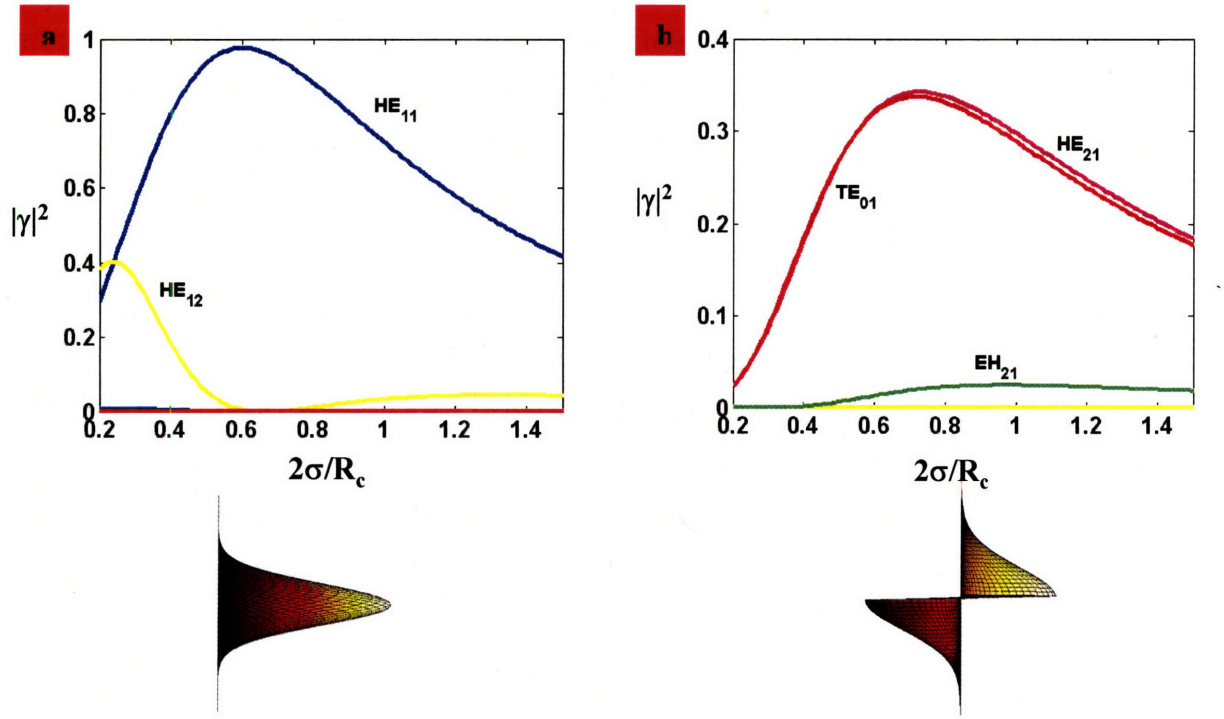

Figure 2.7: The coupling coefficients between the fiber modes and a Gaussian beam having a uniform phase (a) and π phase shift between two halves of the beam (parallel to the beam polarization). The coefficients are plotted as a function of the ratio between the Gaussian beam size and the core radius.

Figure 2.8 depicts the phase distribution on the PPM required in order to obtain significant coupling to the different modes. A constant phase would result in coupling mostly to the HE_{11} mode. Phase shift of π between two halves of the array in the direction parallel to the polarization would result in coupling to the TE_{01}. A phase shift of π in the plane perpendicular to the polarization would result in coupling to the TM_{01} (here however the losses of the TM_{01} are no longer smaller then the HE_{21}).

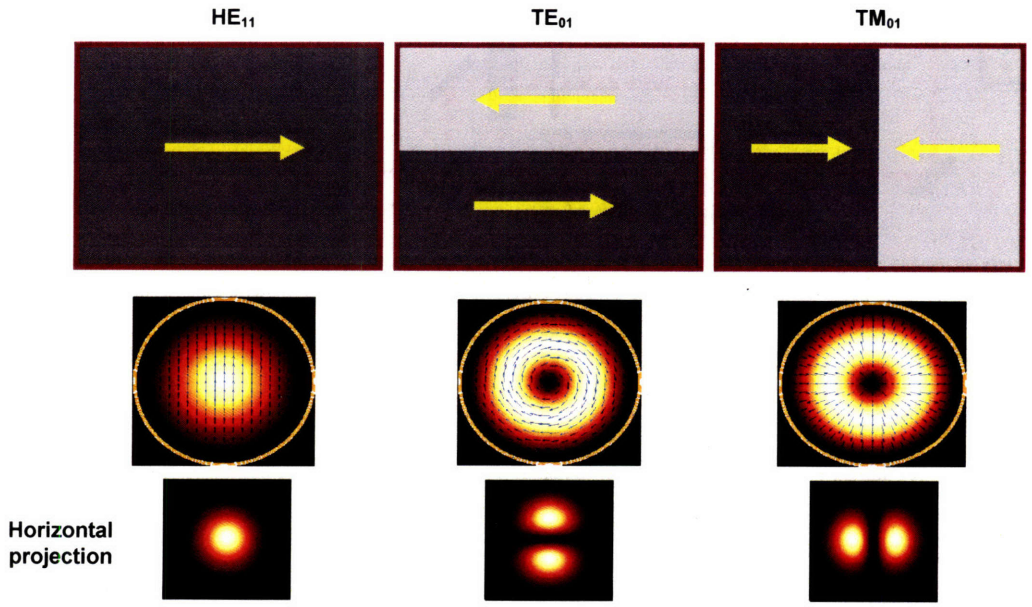

Figure 2.8: Phase distribution of the PPM array for the generation of the linearly polarized HE_{11} mode, the azimuthally polarized TE_{01} mode and the radially polarized TM_{01} mode.

Figure 2.9 shows the setup for generating and coupling the spatially modulated beam. A laser beam from a Ti:Sa is converted to higher wavelength using an optical parametric oscillator (OPO) to generate a 1500 nm beam that in turn expanded and collimated to match the size of the PPM array. The horizontally polarized laser beam is then incident on the PPM that is rotated in 45°. The phase modulated beam reflected from the PPM then passes through a polarizer that is oriented in the vertical and then minifies to match

the fiber core diameter. The input and output beam are imaged using a Vidicon and InGaAs CCD cameras.

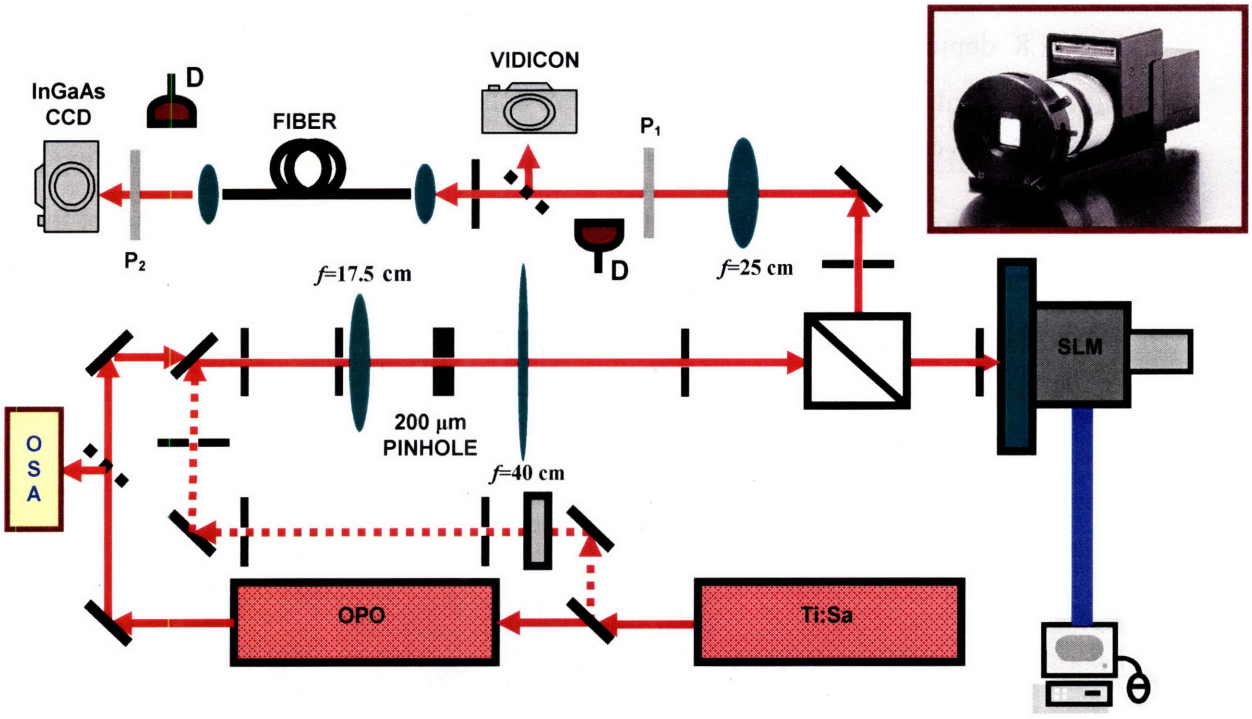

Figure 2.9: Optical setup for the generation of eigenmodes using a spatial light modulator and their coupling to the fiber.

2.5.3 Experimental results

We have experimentally demonstrated the excitation and transmission of the HE_{11} and TE_{01} modes. Figure 2.10a-b shows images of the optical field at the output of the fiber for the two modes at 1540 nm. Figure 2.10z shows the total intensity distribution of the output field, while Fig. 2.10b shows the field after passing through a polarization analyzer rotated to a set of different angular settings to confirm that we are observing the intended modes. We have produced these modes in two different ways: (1) by displacing the fiber input with respect to the input optical beam; and (2) by modulating the optical wave front at the input to the fiber using a spatial light modulator (SLM). While we have reported previously our work on analysis of the modal structure of the fiber output field [49], we here report on the tailored synthesis of the transmitted field.

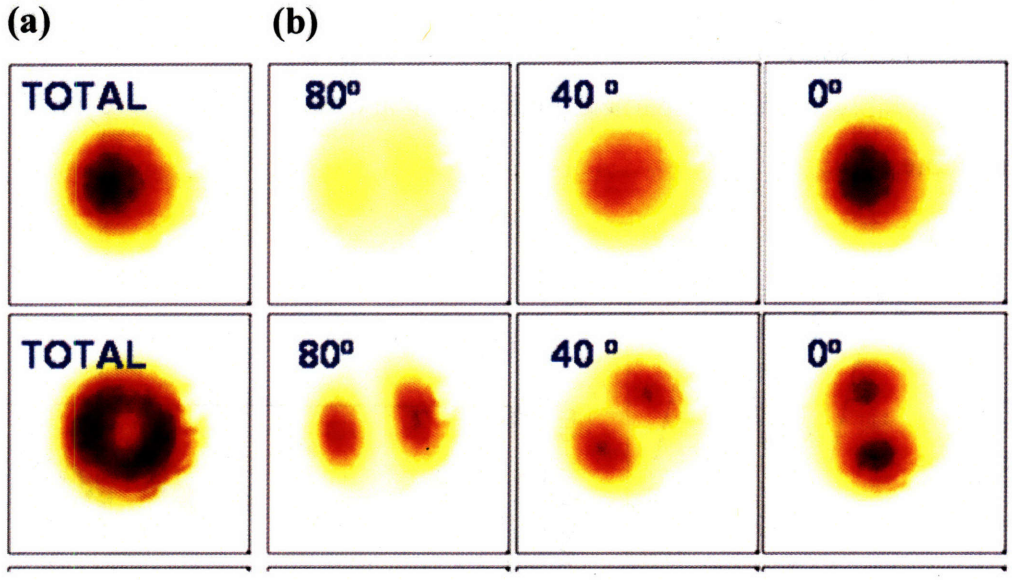

Figure 2.10 (a) Total power and (b) polarization projections along three directions for the HE_{11} mode (top row) and TE_{01} mode (bottom row) at 1540 nm.

In Fig. 2.11a we show the total power at the output of the fiber as a function of the polarization analyzer setting for the two modes at 1540 nm. We have measured the transmission spectra of these two modes and we plot the data in Fig. 2.11b-c. The losses were estimated by scanning the fiber with an integrating sphere and recording the decay in radiated power along the length of the fiber (the optical source was a tunable OPO: Mira, Coherent). Figure 2.11b shows the decay in power radiated from the fiber as a function of propagation distance from the end of the fiber at a fixed wavelength (1505 nm), and the different slopes (corresponding to decay lengths along the fiber) indicate the relative losses of the two modes. We note that the HE_{11} mode has a shorter decay length (higher losses) than the TE_{01} mode. Furthermore, we were not able to excite the HE_{11} mode outside the spectral range depicted in Fig. 2.11, while we observed the TE_{01} mode (albeit with high losses) over a very wide range of wavelengths. We also observe that the transmission bandwidth of the TE_{01} mode is indeed wider than that of the HE_{11} mode.

We have also observed the transmission of the TE_{02} mode. Furthermore, using the SLM we have been able to produce linear superpositions of the TE_{01} and HE_{11} modes with controllable relative complex weights. This new observations have many implications for using these modes as information carriers in optical communications and are also possibly useful for particle guidance in the hollow fiber core under optical radiation pressure.

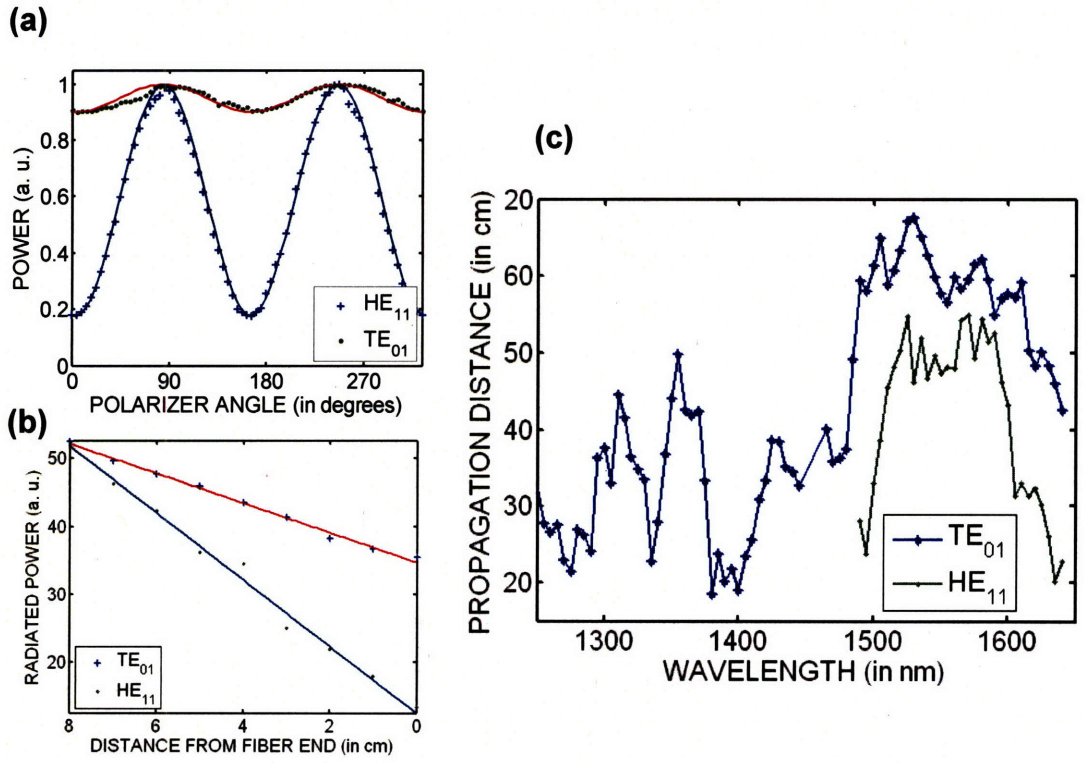

Figure 2.11 (a) Power as a function of polarization angle for the HE_{11} and TE_{01} modes. (b) The decay of radiated power from the fiber when HE_{11} and TE_{01} modes propagate at 1505 nm. (b) Propagation distance for the HE_{11} and TE_{01} modes as a function of wavelength.

3 Active Photonic Bandgap Fibers: Surface Emitting Fiber Lasers

3.1 Introduction

Although laser technology is seen by some as a mature field, innovative structures with exciting new applications do occasionally emerge. A phone conversation with a friend across the Atlantic, storage of memorable pictures to a CD-ROM, or the removal of damaged retinal tissue to restore a patient's vision – at the heart of all this lies a man-made manipulator of light, the laser. The laser is made of three components – gain medium, optical cavity, and pumping process. Since the development of the first laser in 1960 these three elements have come in great variety to address the wide range of needs in science and technology. Fiber lasers [50] and the vertical-cavity surface-emitting lasers (VCSELs) [51] are two types of lasers that have emerged in the past two decades which have found use in many fields, including telecommunication, spectroscopy, medicine, and data storage. Here we present a new type of laser that combines some of the key advantages of both fiber lasers and VCSELs, which we believe could provide enhanced capabilities for diverse technologies, including medical imaging [52-53], explosive vapor and chemical detection [54], photodynamic therapy [55], and fabric displays [56]. Furthermore, this structure enables the study of the fascinating regime of strong coupling in which high quality cavity and matter exchange energy repeatedly [57].

The laser is comprised of a hollow core fiber structure, with the gain medium introduced into the hollow core. The walls of the fiber contain a dielectric omnidirectional reflector, consisting of a multilayer structure running along the entire fiber length. In addition to facilitating guidance of the pump light along the fiber core, this multilayer structure provides the optical resonant cavity required for the build up of laser modes in the radial direction resulting in radiation emission from an extended surface of the fiber (Fig. 3.1a). We coin this laser, the Surface-Emitting Fiber Laser (SEFL).

3.1.1 Surface Emitting Fiber Laser

Heretofore emission from fiber lasers originated solely from the fiber ends in the axial direction with a spot size dictated by the core radius. This is typically achieved by doping glass fibers with rare earth ions such as erbium that serves as a gain medium. The fibers are pumped optically by a co-propagating laser (Fig. 3.1b) and the resonant cavity is provided by Bragg gratings along the axis of the fiber. These lasers are renowned for their high powers, low loss, small size, flexibility, and simple thermal drawing fabrication process. The emission wavelength range of these fiber lasers is limited due to the few elements which can produce gain in these structures. SEFLs on the other hand, while sharing all the listed advantages of ordinary fiber lasers, have no intrinsic limitation to the range of laser emission. The fabrication process allows for easy control of the dielectric layer thicknesses, which in turn permits tuning the bandgap wavelength of the mirror structure to any desired reflection wavelength. Since the hollow core can host practically any gain medium, laser emission can be obtained by simply overlapping the reflection bandgap of the fiber to the emission spectrum of the gain material. Indeed, we have already demonstrated surface-emitting fiber lasers that lase at nine distinct wavelengths in the visible and near infra-red.

The evolution of fiber laser technology from the conventional on-axis emission to surface- emission resembles the evolution of semiconductor wafer based laser technology from edge-emitting lasers to the VCSELs. The latter are made by sandwiching a light emitting layer between highly reflective mirrors (Fig. 3.1c), usually made from dielectric multilayered or epitaxially grown mirrors of distributed Bragg reflectors. Light is emitted perpendicularly from the surface of the mirrors. The SEFL geometry is the cylindrical counterpart of the planar VCSEL with a cylindrical cavity that is encapsulated by multilayered dielectric ring that also results in emission through the surface.

New means to control the light–matter interaction in solids have resulted from the advances in fabrication of semiconductor microcavities and the related VCSELs. In the same manner SEFLs would enable the study of interaction between matter and cavity modes that exhibit fascinating behavior when the rate at which they exchange energy (the Rabi frequency) is greater then the combined decay rate of the matter polarization and the light in the cavity [58]. When this condition is satisfied the system is said to operate in

the strong coupling regime. The ability to fabricate high quality cavities and to introduce a wide variety of matter into the cavities makes SEFL especially good candidate for the study of cavity quantum electro dynamics (QED).

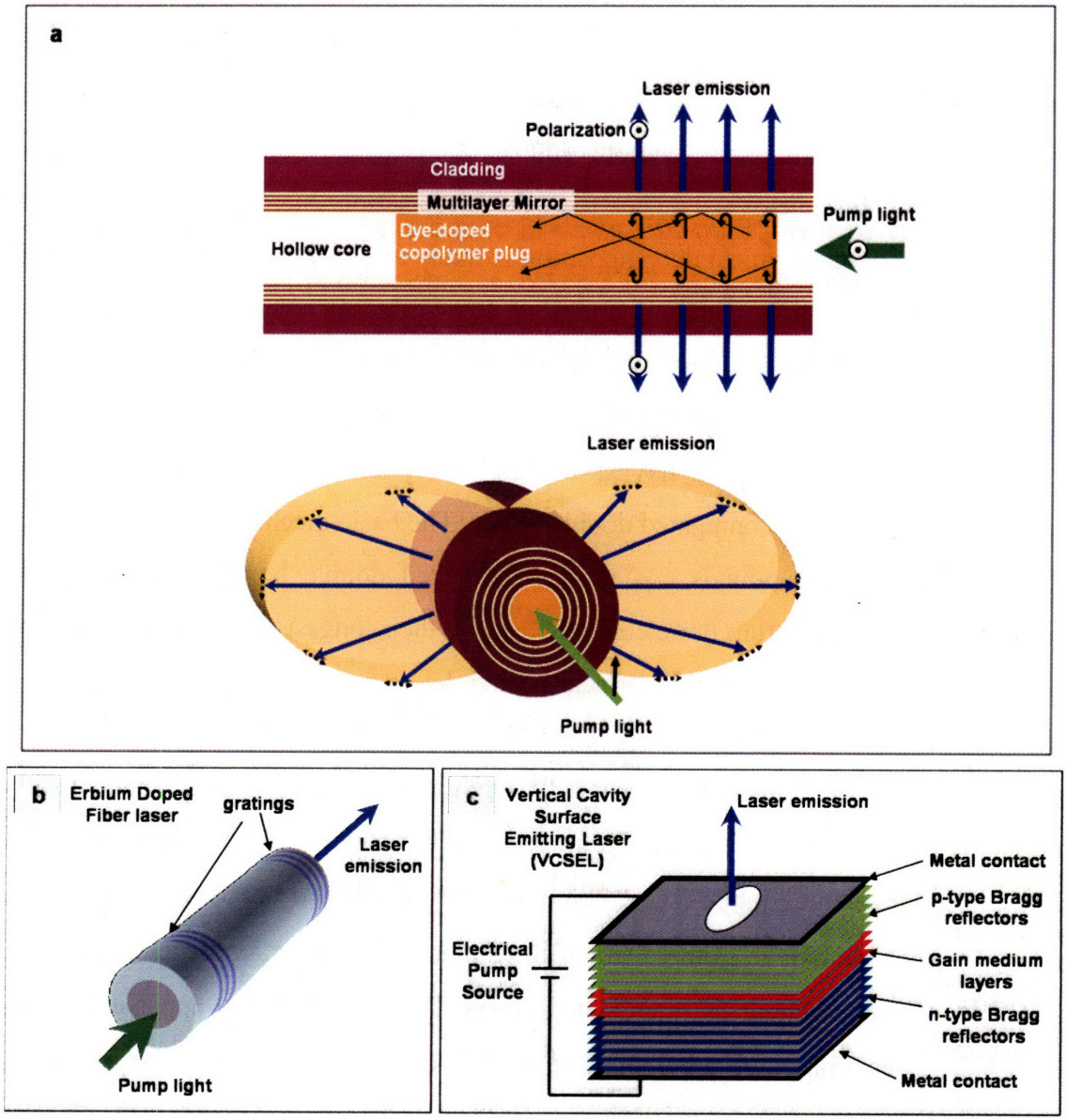

Figure 3.1: Photonic bandgap fiber laser. The fiber laser emits light in the transverse direction (propagation and polarisation vectors shown as solid arrows and dashed lines, respectively) having a dipole-like wavefront from an extended length of the fiber.

3.2 General Properties of Organic Dyes

Organic compounds are defined as hydrocarbons and their derivatives. They can be subdivided into saturated and unsaturated compounds. The latter are characterized by the fact that they contain at least one double or triple bond. These multiple bonds not only have a profound effect on chemical reactivity, they also influence spectroscopic properties. Organic compounds without double bonds usually absorb at wavelengths below 160 nm. This energy is higher than the dissociation energy of most chemical bonds, therefore photochemical decomposition is likely to occur, so such compounds are not very suitable for active materials on lasers. If two double bonds are separated by a single bond, the two double bonds are called conjugated. Compounds with conjugated double bonds absorb light at wavelengths above 200 nm. All dyes in the proper sense of the word, meaning compounds having a high absorption in the visible part of the spectrum, possess several conjugated double bonds. The basic mechanism responsible for light absorption by compounds containing conjugated double bonds is the same, in whatever part of the spectrum these compounds have their longest wavelength absorption band, whether near-infrared, visible, or near-ultraviolet.

The light absorption of dyes can be understood on a semi-quantitative basis if we take a highly simplified quantum-mechanical model, such as the free-electron gas model [59]. This model is based on the fact that dye molecules are essentially planar, with all atoms of the conjugated chain lying in a common plane and linked by σ bonds. By comparison, the π electrons have a node in the plane of the molecule and form a charge cloud above and below this plane along the conjugated chain. The centers of the upper and lower lobes of the π-electron cloud are about one half bond length distant from the molecular plane. hence, the electrostatic potential for any single π electron moving in the field of the rest of the molecule may be considered constant, provided all bond lengths and atoms are the same (Fig. 3.2). Assume that the conjugated chain which extends approximately one bond length to the left and right beyond the terminal atoms has length L. Then the energy E_n of the nth eigenstates of this electron is given by $E_n=h^2n^2/8mL^2$, where is the mass of the electron and n is the quantum number giving the number of antinodes of the eigenfunction along the chain. Thus, if we have N electrons, the lower $N/2$ states are

filled with two electrons each, while all higher states are empty. The absorption of one photon of energy $\Delta E=hc/\lambda$ raises one electron from an occupied to an empty state. The longest wavelength absorption band then corresponds to a transition from the highest occupied to the lowest empty state with $\lambda_{max}=8mcL^2/h(N+1)$. This indicates that to the first approximation the position if the absorption band is determined only by the chain length and by the number of π-electron N.

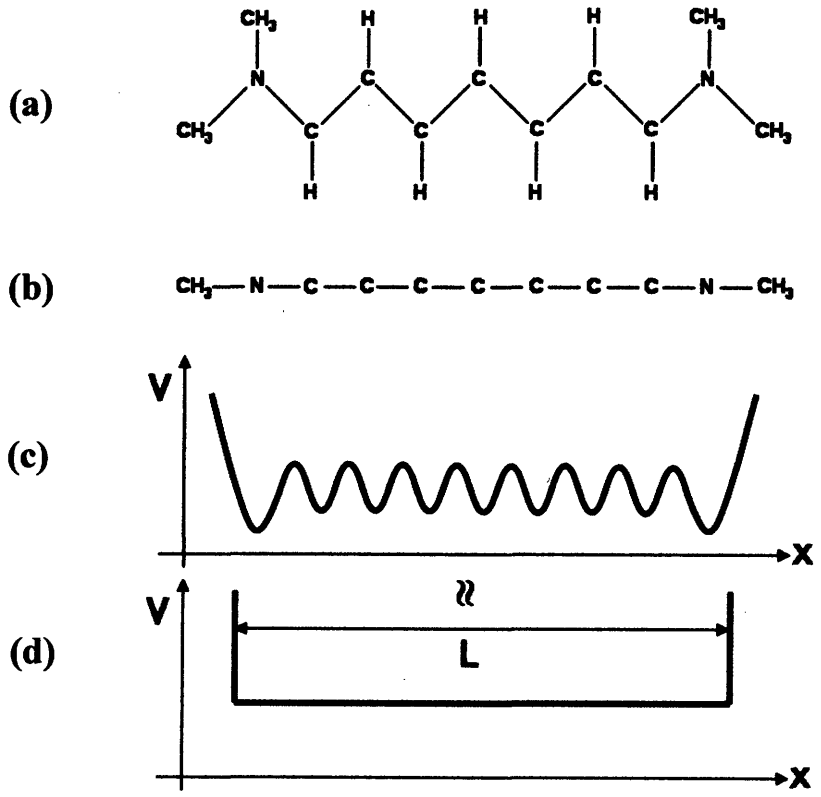

Figure 3.2: a. simple cyanine dye as seen from above the molecular plane; **b.** the same as seen from the side; **c.** potential energy of a π-electron moving along the carbon atoms; **d.** simplified potential energy.

A peculiarity of the spectra of organic dyes as opposed to atomic or ionic spectra is the width of the absorption bands, which usually covers several tens of nanometers. This is immediately comprehensible when one recalls that a typical dye molecule may possess fifty or more atoms, giving rise to about 150 normal vibrations of the molecular skeleton. Many of these vibrations are closely coupled to the electronic transitions by the change in electron densities over the bonds constituting the conjugated chain. Furthermore, collisional and electrostatic perturbations, caused by the surrounding solvent molecules, broaden the individual lines of such vibrational series. As a further complication, every

vibronic sublevel of every electronic state, including the ground state, has superimposed on it a ladder of rotationally excited sublevels. There are extremely broadened because of the frequent collisions with the solvent molecules which hinder the rotational movement so that there is a quasicontinuum if states superimposed on every electronic level.

The free-electron modal can also provide a simple explanation for another important property of the energy levels of organic dyes, namely the position of the triplet levels relatively to the singlet levels. It can be shown [59] that for every excited singlet state there exists a triplet state of somewhat lower energy. Direct observation of absorptive transitions from the singlet ground state into triplet states is very difficult since the transitions are spin-forbidden. Fig 3.3 depicts the eigenstates of the dye molecule in which a ladder of singlet states S_i containing also the ground state G. Somewhat displaced towards lower energies there is the ladder of triplet states T_i. The longest wavelength absorption is from G to S_1, the next absorption band from G to S_2, etc. By contrast the absorption from G to T_i is spin-forbidden.

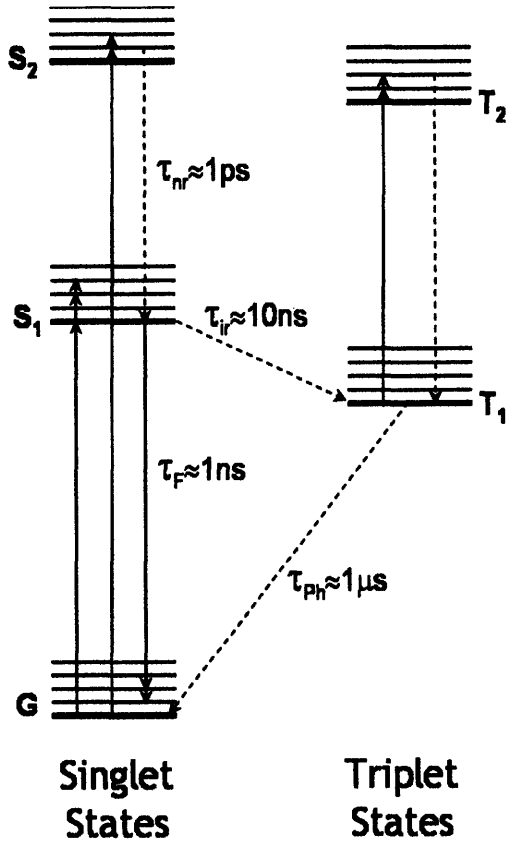

Figure 3.3: energy levels of typical dye molecule with radiative (solid lines) and nonradiative (broken lines) transitions with the intersystem crossing between the singlet and triplet and phosphorescence transition between the lowest energy triplet state to the ground state of the singlet.

There are many processes by which an excited molecule can return directly or indirectly to the ground state. Some of these are schematically depicted in Fig. 3.3. It is the relative importance of these which mainly determines how useful a dye will prove in dye lasers. The one process that is directly used in dye lasers is the radiative transition from the first excited singlet state S_1 to the ground state G. There also exist the possibility that the energy hypersurface of the excited state will approach closely enough to the ground state for the molecule to tunnel through the barrier between them. It is then found in a very highly excited vibronic level of the ground state. This process is generally termed "internal conversion". The internal conversion between S_2 and S_1 is usually extremely fast, taking place in less than 10^{-11} s. This is the reason why fluorescence spectra of dyes generally do not depend on the excitation wavelength. The radiationless transition from an excited singlet state to a triplet state can be induced by internal perturbations (spin-orbit coupling, substituents containing nuclei with high atomic number) as well as by external perturbations (paramagnetic collision partners, like O_2 molecules in the solutions or solvent molecules containing nuclei of high atomic number). These radiationless transitions are usually termed "intersystem crossing".

The radiative transition from T_1 o G is termed "phosphorescence". As expected for spin-forbidden transitions, it is extremely long, ranging from milliseconds to many seconds for molecules with small spin-orbit coupling. The lowest singlet and triplet states can also be deactivated by a long-range radiationless energy transfer to some other dye molecule. For this to happen, the absorption band of the latter "acceptor" molecule must overlap the fluorescence or phosphorescence band of the "donor" molecule.

3.2.1 Dye Lasers

In principle, there are two possible ways of using an organic solution as the active medium in a laser: One might utilize either the fluorescence or the phosphorescence emission. At first sight the long lifetime of the triplet state makes phosphorescence look

more attractive. On the other hand, due to the strongly forbidden transition, a very high concentration of the active species is required to obtain an amplification factor large enough to overcome the inevitable cavity losses. In fact, for many dyes this concentration would be higher than the solubility of the dyes in any solvent. A further unfavorable property of these systems is that there will almost certainly be losses due to triplet-triplet absorption. It must be remembered that triplet-triplet absorption bands are generally very broad and diffuse and the probability they will overlap the phosphorescence band is high.

If the fluorescence band of a dye solution is utilized in a dye laser, the allowed transition from the lowest vibronic level of the first excited singlet state to some other higher vibronic level of the ground state will give a high amplification factor even at low dye concentrations. The main complication in these systems is the existence of the lower-lying triplet states. The intersystem crossing rate to the lowest triplet state is high enough in most molecules to reduce the quantum yield of fluorescence to values substantially below unity. This has a two-fold consequence: Firstly, it reduces the population of the excited singlet state and hence the amplification factor; and secondly, it enhances the triplet-triplet absorption losses by increasing the population of the lowest triplet state. The problem of intersystem crossing can be solved if the pumping light flux density rises fast enough such that the population of the triplet level is held small, i.e. if the pump flux reaches threshold in a time which is small compared to the reciprocal of the intersystem crossing rate. For a typical value of 10^7 s^{-1} the rise time should be less than 100 ns which is much longer then sub-nanosecond rise time of the Nd:YAG and therefore we can restrict our analysis to the singlet state.

Molecules that take part in the dye laser operation have to fulfill the following cycle: Absorption of pump radiation at ν_p and with cross-section σ_p lifts the molecule from the ground state with population n_0 into a higher vibronic level of the first (or second) excited singlet state S_1 (or S_2) with a population n_1 (or n_2). Since the radiationsless deactivation to the lowest level of S_1 is so fast, the steady state population n_1 is negligibly small, provided the temperature is not so high that this vibronic level is already thermally populated by the Bolzmann distribution of the molecules in S_1. Stimulated emission then occurs from the lowest vibronic level of S_1 to higher vibronic levels of G. Again the

population n_0 of this vibronic level is negligible since the molecules quickly relax to the lowest vibronic levels of G.

It is then possible to write the oscillation condition for a dye laser. In its simplest form a dye laser consist of a cavity of length L with dye concentration of n and of two mirrors of reflectivity R for the laser resonator. With n_1 molecules excited to the first singlet state, the dye laser start oscillating at frequency ν, if the overall gain is equal to or greater than one:

$$\exp\left[-\sigma_a(\nu)n_0L\right]R\exp\left[+\sigma_f(\nu)n_1L\right]\geq 1 \tag{3.1}$$

Here $\sigma_a(\nu)$ and $\sigma_f(\nu)$ are the cross-sections for the absorption and stimulated fluorescence, respectively, and n0 is the population if the ground state. The first exponential term gives the attenuation due to reabsorption of the fluorescence by the long-wavelength tail of the absorption band. The attenuation becomes the more important, the greater the overlap between the absorption and fluorescence bands.

Since the fluorescence band usually is mirror image of the absorption band, the maximum values of the cross-sections in absorption and emission are found to be equal, i.e., $\sigma_{a,max}=\sigma_{p,max}$. Taking the logarithm of (3.1) and rearranging leads to a form of the oscillation condition which makes it easier to discuss the influence of the various parameters

$$\frac{S/n+\sigma_a(\nu)}{\sigma_f(\nu)+\sigma_a(\nu)}\leq\frac{n_1(\nu)}{n} \tag{3.2}$$

where $S = (1/L)ln(1/R)$. The constant S only contains parameters of the resonator. Other types of losses, like scattering, diffraction, etc., may be accounted for by an effective reflectivety, R_{eff}. The value of n_1/n is the minimum fraction of the molecules that must be raised to the first singlet state to reach threshold. The absorbed power density W necessary to maintain a fraction n_1/n of the molecular concentration n in the exited state is $W=n_1h\nu_p/\tau_f$ where τ_f is the radiative lifetime of S_1. The power flux, assuming the incident radiation is completely absorbed in the dye sample, $P=W/n\sigma$ where σ is the total molecular absorption cross-section.

The polarization of the dye laser beam is determined mainly by the polarization of the exciting laser beam, the relative orientation of the transition moments in the dye molecule

for the pumping and laser transitions, and the rotational diffusion-relaxation time. The latter is determined by solvent viscosity, temperature and molecular size. The direction of the transition moments of the fluorescence and the long wavelength absorption is identical, since the same electronic transition is involve in both processes.

Most often the pump pulse is of approximately Gaussian shape and its FWHM power is less then the reciprocal of the intersystem-crossing transition rate. Thus, we can expect the following time behavior, neglecting finer detail for the moment. Shortly after the pump pulse reaches threshold level, dye-laser emission starts. The dye laser output power closely follows the pump power till it drops below threshold, when dye-laser emission stops. The dye-laser pulse shape should thus closely resemble that of the part of the pump pulse above the threshold level. A detailed treatment is due to Sorokin [60] who solved the rate equations for the excited state population in the dye and the photons in the cavity

$$\frac{dN_1}{dt} = W(t) - \frac{N_1}{N_t}\frac{Q}{t_c} - \frac{N_1}{\tau_f}$$
$$\frac{dQ}{dt} = \frac{Q}{t_c}\left(\frac{N_1}{N_t} - 1\right) \tag{3.3}$$

where N_1 is the excited state population, N_t is the threshold inversion, Q is the number of photons in the cavity, t_c is the cavity lifetime, τ_f is the fluorescence lifetime, and $W(t)$ is the pump pulse envelope normalized to the total number of pumping photons, i.e., $\int_{-\infty}^{\infty} W(t)dt = N_{pump}$

3.3 Photonic Bandgap Fiber Laser Structure

Here we report on the conceptual framework and development of a radially surface-emitting fiber laser that is capable of dynamic tuning of both the gain medium position along the fiber axis and the direction of emission. The design, fabrication and characterization of polymeric, photonic bandgap [16], *surface-emitting* fiber lasers which combine some of the key advantages of both vertical cavity [51] and fiber lasers [50] are reported. First, a cylindrical multilayer hollow-fiber structure with a fundamental photonic bandgap in the visible and near infrared is fabricated. A gain medium comprising an organic dye dispersed in a monomer solution is then introduced into a

desired location along the fiber axis and subsequently polymerized to form a line source of prescribed length. The photonic bandgap in this fiber plays a dual role. It both guides the optical pump along the fiber axis and acts as a laser resonator in the transverse direction. Consequently, radially directed lasing occurs from the fiber circumference, and light is emitted along an extended length of the fiber. Both the directionality and polarization of the emitted wavefront is controlled via the pump polarization. Lasing at nine different wavelengths spanning the visible spectrum is demonstrated. At the 652-nm line we obtained 37% efficiency, 1-nm linewidth, and 86-nJ lasing threshold.

The surface-emitting fiber laser structure and pumping arrangement are shown schematically in Fig. 3.1a. The structure comprises a gain medium in the core surrounded by a photonic bandgap (PBG) structure [16,18] made of 58 layers of a wide mobility gap amorphous semiconductor, As_2S_3, alternating with a high-glass-transition temperature polymer, poly(etherimide) (PEI). A scanning electron microscope micrograph of the multilayer structure (Fig. 3.4a) verifies the uniformity of the layer thicknesses throughout the fiber. The individual layer thicknesses are 59 nm (As_2S_3) and 89 nm (PEI), and the structure is terminated by a 29.5-nm thick layer to eliminate surface modes. The gain medium is pumped axially while the resonant cavity provided by the PBG ensures laser emission in the radial direction. The PBG structure performs a dual role enabled by the characteristic shift of the band edges to higher frequencies with increase in wave vector as depicted in Fig. 3.4b. The normal-incidence bandgap, defined for axial wave vector k = 0 (region A), provides the optical feedback necessary for achieving lasing action in the radial direction. Concurrently, the blue-shifted bandgap having axial wave vectors near the light line (region B) is responsible for guiding the pump frequency.

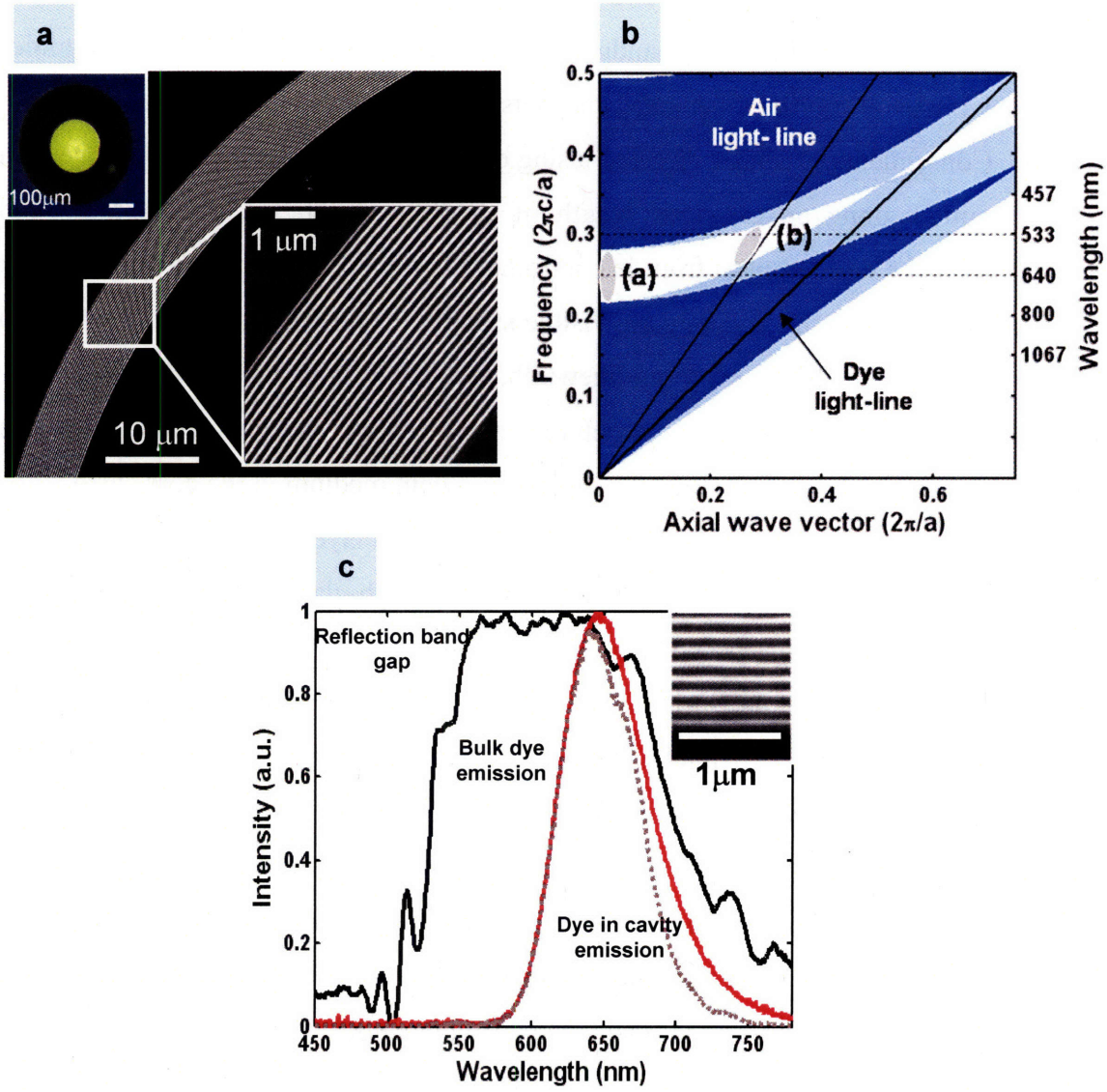

Figure 3.4: Structure of the fiber laser cavity. **a**, Cross-sectional SEM micrographs of the PBG multilayer structure at various magnifications. The PEI in the cladding and the layers appears black, and the As_2S_3 layers white. The PEI and As_2S_3 layers are 164 nm and 76 nm thick (except for the first and last As_2S_3 layers which are 38 nm thick; the first layer is not visible). The top left inset shows a cross-sectional fluorescence micrograph of the full cross-section of a PBG fiber with an R590 organic dye in the core and enveloped by a thick PEI protective cladding. **b**, Projected band structure of a one dimensional photonic crystal consisting of alternating layers of As_2S_3 and PEI. Transverse-electric (TE) and transverse-magnetic (TM) propagating modes are in dark and light blue, respectively; evanescent modes are in white. Light incident normally to the structure (k=0) and axially propagating modes through the hollow core are shown as regions A and B, respectively. **c**, Measured reflection band gap centred around 620nm (see 'Optical characterization' in methods) in black; fluorescence spectrum of LDS698 (500 ppm concentration) in red; and calculated dye-in-cavity emission obtained by multiplying the last two, dashed line.

While different types of gain media may be used in conjunction with the fiber, for simplicity we chose an organic laser dye [59] incorporated into a copolymer matrix. The upper inset in Fig. 3.4a is a fluorescence micrograph of the fiber cross section. An organic dye, LDS698, having a fluorescence peak at 645 nm was dispersed in a copolymer and inserted into the otherwise hollow core of a PBG fiber. Since the normal-incidence PBG is 26% of its centre-frequency, it encompasses the entire fluorescence spectrum as shown in Fig. 3.4c. This same fiber supports the propagation of a pulsed optical pump at 532 nm traveling through the fiber core.

3.4 Laser Emission Characteristics

We observe broad fluorescence emission from the above described fiber laser at pump-pulse energies lower than the 86 nJ threshold, while radially directed lasing occurs with sharp peaks at 652 nm above threshold (Fig. 3.5a). To confirm that the emitted radiation is indeed laser light and not amplified spontaneous emission, we show in Fig. 3.5a the emission spectra of the fiber for three different pump energies: below (A), near (B) and above (C) threshold. The lasing threshold occurs at pump energies of 86 nJ and 110 nJ for dye concentration of 500 ppm and 50ppm, respectively. The dependence of the emission bandwidth (Fig. 3.5a inset) and energy (Fig. 3.5b) on the pump energy for both 500 ppm and 50 ppm dye concentrations are shown. Both clearly demonstrate laser thresholds. The slope efficiencies are 37.5% and 16.5% for the 500 ppm and 50 ppm concentrations, respectively.

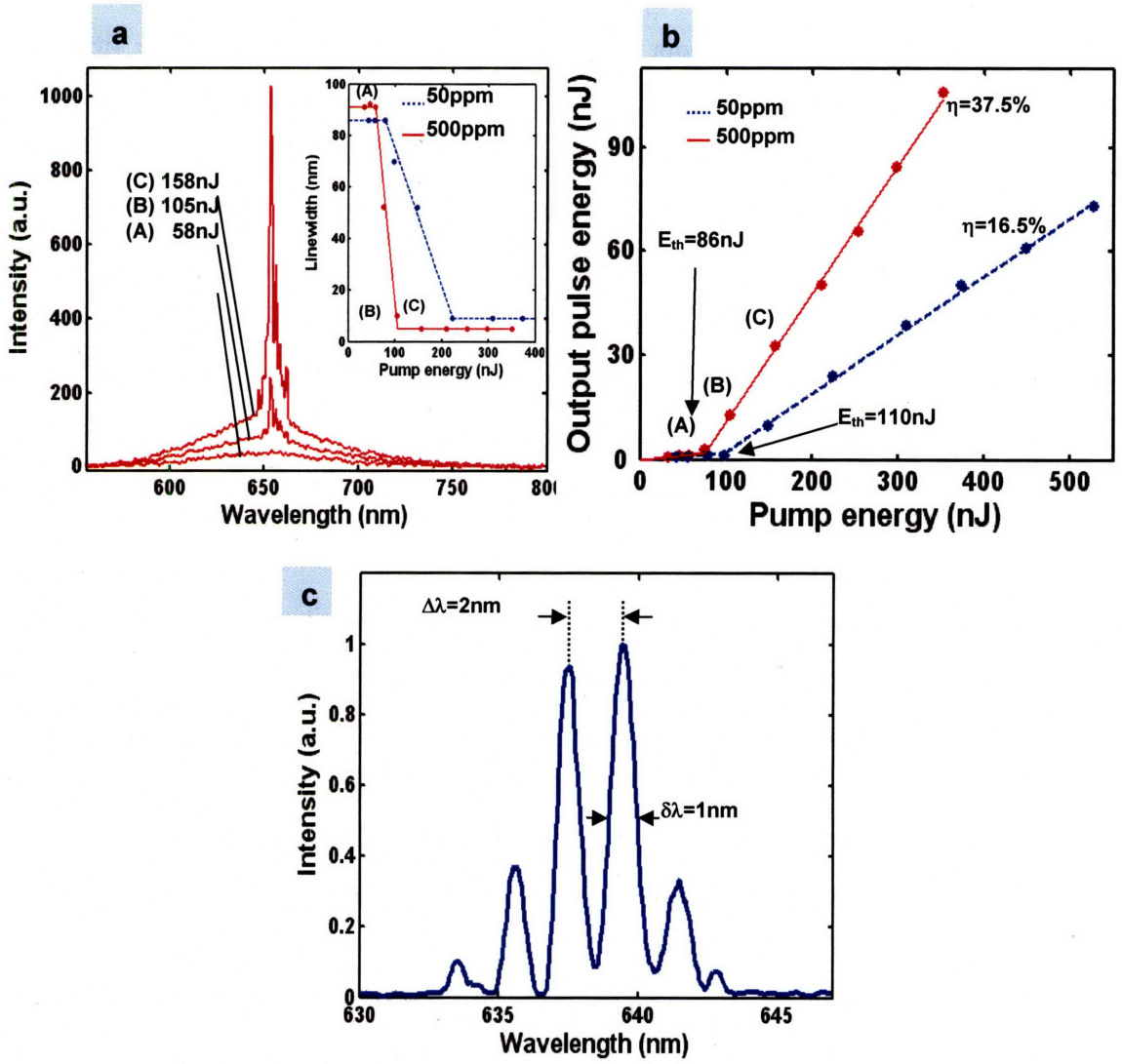

Figure 3.5: Lasing characteristics of an LDS698-doped PBG fiber. **a,** Emission spectra of the fiber laser for a dye concentration of 500 ppm and pump energy below threshold (A), $1.2E_{th}$ (B) and $1.8E_{th}$ (C), where E_{th} is the lasing threshold energy. Inset shows the spectral full-width at half-maximum as a function of input energy for 500 ppm (red line) and 50 ppm (dashed blue). **b,** Dependence of the laser energy on the pump energy showing threshold values of E_{th} = 86 nJ and E_{th} = 100 nJ for the 500 ppm and 50 ppm, respectively. **c,** High resolution spectral measurement reveals mode spacing of 2 nm and quality factor of 640.

The PBG fiber (core diameter d_c = 70 μm) supports many longitudinal cavity modes in the transverse plane having a free spectral range $\Delta\lambda \approx \lambda_0^2 / 2nd_c$, where n is the core refractive index and λ_0 is the lasing centre wavelength. The lasing spectrum was resolved into its modes, as shown in Fig. 3.5c, using an optical spectrum analyzer (ANDO

AQ6317), and the 2-nm mode spacing (corresponding to a 68-μm core diameter) is in good agreement with the expected value. The measured $\delta\lambda$, the spectral width of one mode, is lower than theoretically expected. Possible reasons for this discrepancy are the losses arising from an imperfect cavity structure and the limited spectral resolution of the measurement setup.

The optical wavefront emanating from the fiber laser has several unusual characteristics that stem from the combination of the emission properties of the dye and the resonant cavity design. First, the emitted laser wavefront has a surprising dipole-like radiation pattern, shown in Fig. 3.6b. This measurement was done in two different ways. First the orientation of the pump polarization at the input to the fiber was rotated while a probe recorded the emitted intensity in the x-polarization at a fixed location along the y-axis (Fig. 3.6a). This measurement was then corroborated by physically rotating the probe around the surface of the fiber laser while keeping the pump polarization fixed in the x-direction. Upon comparing the radiation pattern to that of a bulk dye-doped copolymer sample excited with the same pump, we find the dipole-like radiation pattern is not as pronounced as in the fiber laser (Fig. 3.6b). In a previous section dealing with the properties of dye lasers we showed that dye molecules that are aligned with the pump polarization contribute the most to the fluorescence. This may be confirmed by measuring the degree-of-polarization of the dye fluorescence for pump polarization fixed in the x-direction, shown in Fig. 3.6c (dotted line). This measurement was done by placing a polarizer along the y-axis, the direction of maximum emission, and recording the emitted intensity as a function of the polarizer orientation in the xz-plane (Fig. 3.6c). The dipole radiation patterns of the dye molecules combine to result in the radiation pattern shown in Fig. 3.6b where the strongest radiation is in the direction orthogonal to the pump polarization and the fiber axis. Since fluorescence polarized parallel to the pump is stronger, cavity modes with this polarization have lower thresholds. Consequently, the fiber laser has an enhanced degree-of-polarization compared to that of the bulk dye emission (Fig. 3.6c, solid line) and a more prominent dipole-like radiation pattern. This interesting result suggests that the direction of the laser beam can be controlled remotely just by rotating the pump polarization.

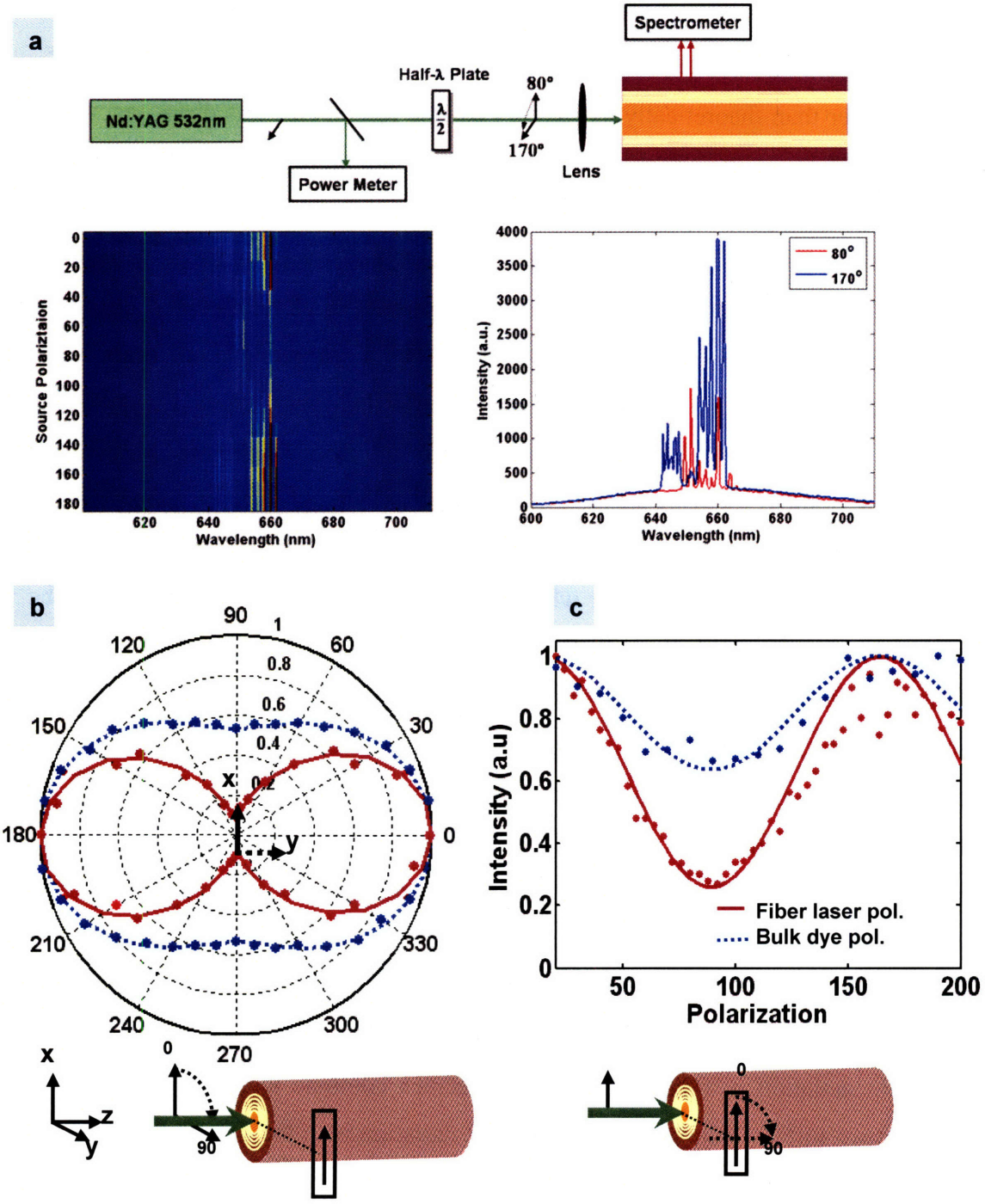

Figure 3.6 Geometric dependence of the emission for an LDS698-doped PBG fiber laser. **a,** schematic of the polarization measurement setup with the measured results showing the emission spectrum as a function of the pump polarization. **b**, Angular intensity pattern of the bulk dye and fiber laser emission at a fixed location along the *y*-axis measured by rotating the input polarisation. This measurement is equivalent to fixing the pump polarisation while measuring the emission intensity around the fiber. **c**, Polarisation of light emitted from bulk dye (dashed blue) and dye in a fiber cavity (red line) having a degree-of-

polarisation of 0.22 and 0.6, respectively, measured by fixing the pump polarisation in the x-direction and recording the intensity as a function of polariser rotation about the direction of maximum emission (y-axis).

A second unique feature of this laser is that emission occurs over a spatially extended region by virtue of the extended surface area of the fiber resonator walls. This is in contrast to semiconductor [61,62] and polymer [63] planar annular resonators in which the resonator thickness is on the order of the emission wavelength. Figure 3.7 shows the emission spectrum as a function of position along a large-core (d_c = 200 μm) PBG fiber. By moving a probe along its axis we observed laser radiation extending along ~ 5 mm of the fiber (measured at full-width-half-maximum). The upper panel of Fig. 3.7 shows a photograph of this operating laser. One may further increase the fiber length from which laser light is emitted by optimizing dye concentration, core size, and PBG structure.

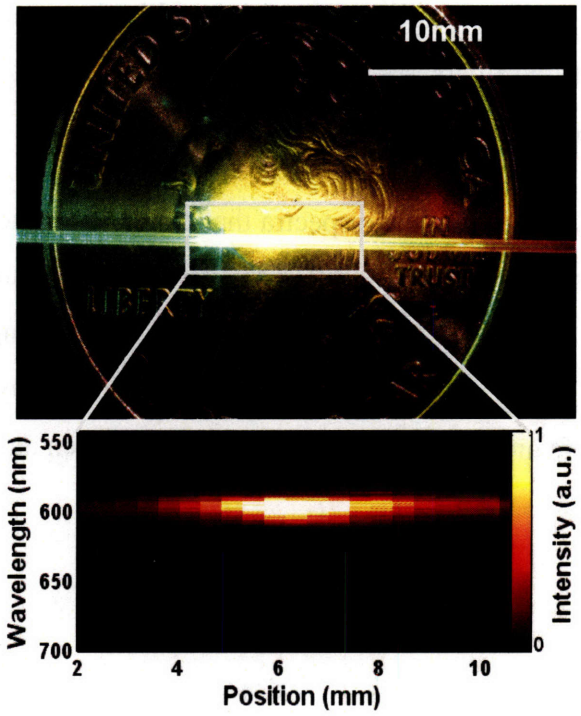

Figure 3.7 Emission spectra from large core (200-μm) PBG fiber laser measured along the fiber axis at 10-μJ pump energy measured by scanning a probe fiber along the fiber side. The upper panel shows a photograph of the fiber showing laser light emitted from a spatially extended region along the fiber (~ 5 mm).

The dual action of the PBG structure as both a transverse laser cavity and a transmission waveguide is highlighted in Fig. 3.8a. In this specific fiber, a short segment of Rhodamine 590 doped copolymer was introduced into a PBG fiber, leaving the rest of the core hollow. The photograph of the bent fiber displays both features: the hollow-core portion of the fiber transmits the pump light (green, $\lambda = 532$ nm, top of the photograph), and the dye-doped portion emits orange-coloured laser light ($\lambda = 576$ nm).

Furthermore, the placement of dye-doped segments along a fiber can be carefully controlled. A demonstration that highlights the ability to finely tune segment size, location, and composition is shown in Fig. 3.8b. A lasing display projects the letters "MIT" in two colours. All the lasing fibers contain copolymer segments doped with DCM (orange). Additionally, the "i"-fiber contains both DCM and LDS698 (red) demonstrating that more than one gain medium can be precisely placed in the same fiber. This specific display contains 12 dye-filled fibers that are pumped from both ends. The large segments contain less than 0.5 μl of dye-doped polymer.

Finally, the use of dyes with fluorescence spectra that extend over the visible and near-IR wavelengths is made possible by simply scaling the PBG structure and hence shifting the bandgap. Nine different dyes were inserted into separate fibers having bandgaps matched to their emission peaks. The lasing spectra of these fibers are displayed in Fig. 3.8c, and photographs of three lasers are shown depicting bright blue, green and red laser light.

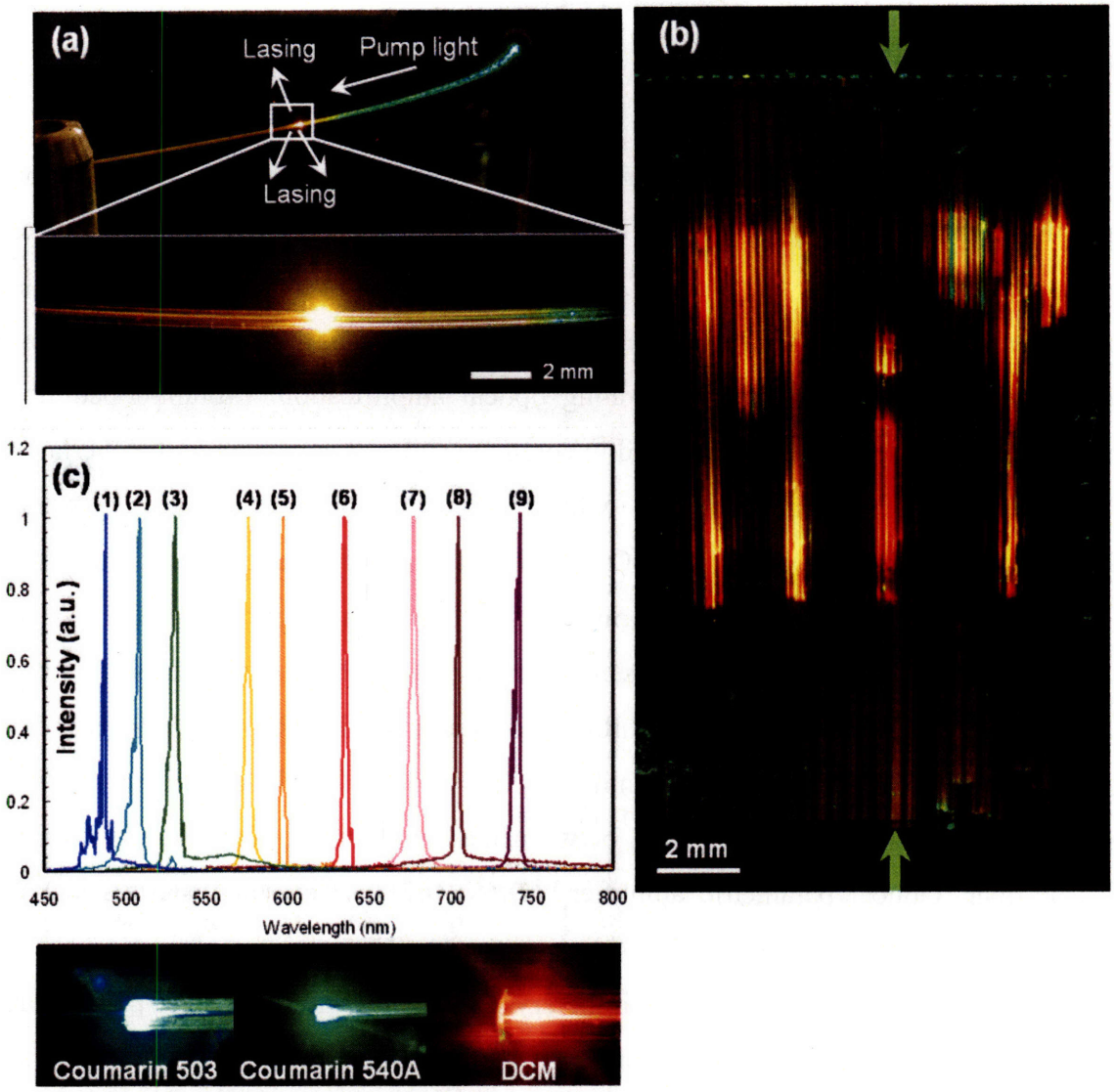

Figure 3.8: a, A photograph of an R590-doped PBG fiber showing the pump (532 nm, green) guided in the hollow-core PBG fiber. Lasing at 576 nm (orange) occurs in the R590-doped region. **b,** Lasing "MIT" made out of 12 PBG fibers doped with DCM (orange) and LDS698 (red) that are simultaneously pumped in both directions. This display design illustrates the ability to finely tune dye location, size, and concentration. **c,** Laser emission spectra from fibers doped with nine different dyes. The lasers producing emission spectra 1-3 are constructed using the same hollow-core PBG fibers having a fundamental reflection bandgap at 500 nm, and were pumped at 355 nm. The fibers used to produce emission spectrum 4 have a fundamental reflection bandgap at 600 nm, while those used for spectra 5-9 have a fundamental reflection bandgap at 690nm, and all were pumped at 532 nm. Photographs of the organic dye-doped PBG fiber lasers showing the individual laser colours (blue, green and red) emitting from the fiber surface.

3.5 Hollow Core Fiber Amplifier

3.5.1 Introduction

The development of optical amplifiers revolutionized the field of optical communications and has contributed enormously to the unprecedented expansion in optical communication networks. Furthermore, optical amplifiers are often used for short-pulse amplification and in general for the generation of high-power sources. There are predominantly four methods of generating optical amplification. Erbium-doped fiber amplifiers (EDFA) [64] are widely used in communication systems due to the overlap of the amplification spectrum window with the entire C-band of optical networks. Semiconductors Optical Amplifier (SOA) [65] are typically made from group III-V compound semiconductors. Their performance is still not comparable with the EDFA due to the short nanosecond or less upper state lifetime that results in higher noise and high nonlinearity with fast transient time. In Raman optical amplifier (ROA) [66] the signal is intensified by Raman amplification. Unlike the EDFA and SOA the amplification effect is achieved by a nonlinear interaction between the signal and a pump laser within an optical fiber. Optical parametric amplifiers (OPA) [67] use crystal materials lacking inversion symmetry that can exhibit $\chi(2)$ nonlinearity. Parametric amplification occurs when a signal beam propagates through the crystal together with a stronger pump beam of shorter wavelength. The pump is converted into lower-energy signal photons and the same number of so-called idler photons; the photon energy of the idler wave is the difference between the photon energies of the pump and signal waves.

3.5.2 Amplifier Structure and design considerations

Here we propose a new type of optical fiber amplifier that is constructed of a multilayer cylindrical photonic bandgap hollow fiber coated from the inside by a sub-wavelength layer of active material (Fig. 3.9). Several key advantages over the standard solid core EDFA and ROA can already be noticed. First, the signal propagates predominantly in the hollow core part of the fiber and therefore higher energy signals can be supported without reaching the limit of mechanical breakdown. Second, application dependent, strong suppression of non-linear processes compared to solid core fiber amplifiers. Third, the

recent use of hollow-core in applications such as atom-guidance, high harmonic generation, super continuum generation, and more allows one to study systems in which light can be amplified.

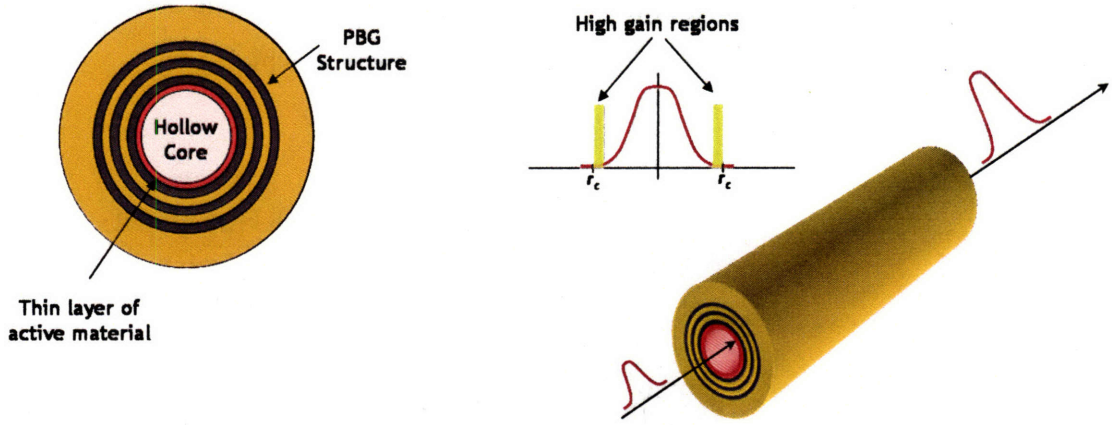

Figure 3.9: Hollow core photonic bandgap fiber amplifier constructed of hollow core cylindrical multilayer fiber with a sub-wavelength active material layer on the core-cladding surface that. The amplification of light that propagates along the fiber axis is due to the high gain experienced by the tails of the mode on the core-cladding interface.

The optical amplification experienced by a core propagating mode is due to the interaction of the mode tail on the core-cladding surface with the inverted population of the active material. The sub-wavelength thickness of this layer necessitates that the active material small signal gain would be large enough such that the core propagating mode would experience overall amplification. The finite thickness of the active material introduces a perturbation to the multilayer cladding and causes the lowest energy core-mode to cross the light line and to become a surface state. Figure 3.10 shows that frequency range of the projected band diagram in which this interaction occurs for active layer of 25 nm. The slow transmission between the two modes is due to the sub-wavelength thickness of the layer, the two insets in Figure 3.10a are showing the intensity pattern of the mode before and after the transition. When the field overlaps strongly with the active material we expect to obtain strong amplification as shown in Figure 3.10b. Here we calculated the gain as a function of frequency in the vicinity of the transition for several absorption coefficients of the active material. Below that frequency the mode

overlap with the active material is not sufficient to generate amplification, however for absorption coefficients of ~10^5 m^{-1} strong gain can be obtained for modes that are even below the transition frequency having their field concentrated predominantly in the center of the core. We should note that in practice the emission spectrum of the active material should overlap with that transition frequency in order to obtain this high gain.

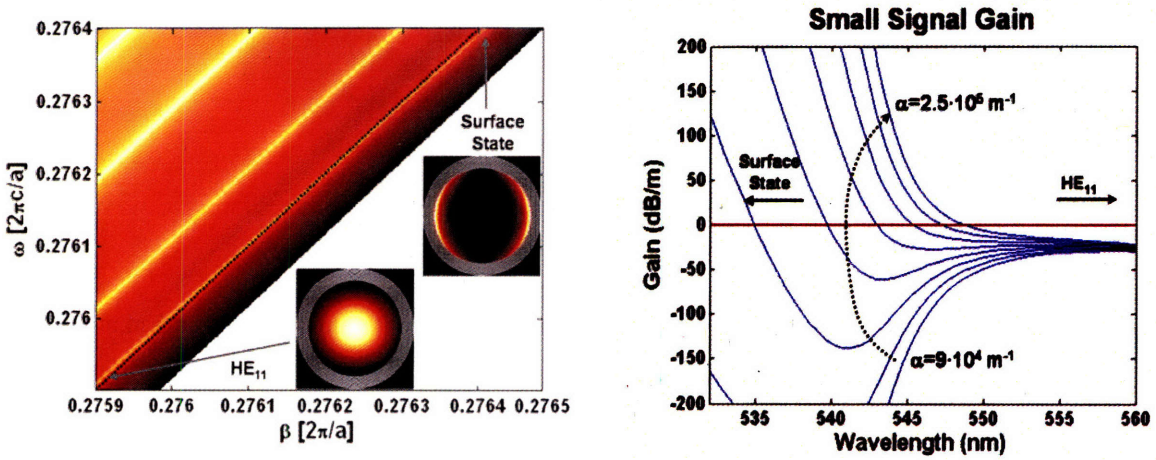

Figure 3.10: a. section of the band diagram showing a core propagating mode crossing the light-line to become a surface state. **b.** in the vicinity of the interaction the field distribution of the mode is still concentrated mostly in the hollow-core but with small portion in the active medium, if the absorption coefficient of the active material is large enough the small signal gain becomes positive.

3.5.3 Experimental results

We fabricated a cylindrical multilayer fiber and spin coated the core-cladding surface with a 25 nm thick layer of organic amplifying fluorescence polymer (AFP) [54,68]. This polymer has a peak absorption coefficient of $8 \cdot 10^6$ m^{-1}, an order of magnitude larger then the required calculated value, and an emission spectrum ranging from 500-550 nm. The fiber was designed to have a bandgap centered at 530 nm. In order to measure the small signal gain of such a system we used a Nd:YAG laser with the 532 nm second harmonic as signal and the 355 nm third harmonic as pump. Figure 3.11a depicts a schematic of the setup. The laser generates the two harmonics with a perpendicular polarization and therefore in order to make them interact in the fiber we needed to rotated the polarization of one of them. Furthermore it is necessary to control the intensity of each harmonic

separately. The beams were split using two dichroics and then were filtered in order to eliminate any residue of the other harmonic. The polarization of the 532 nm harmonic was rotated to the direction of the 355 nm pump and an attenuator was placed in its path. The beam were then combined and coupled into the fiber using a lens. The pump signal was filtered out at the output of the fiber using a high-pass filter and the transmitted signal along with the spontaneous emission from the fiber was collected using a lens and coupled into a spectrometer. Figure 3.11b shows a picture of the fiber when the pump beam propagates in it; the green emission from the sides is of the AFP. The emission spectrum measured with the spectrometer at the end of the fiber (Figure 3.11c) shows that the 532 nm signal is ~5dB stronger than when the pump is off.

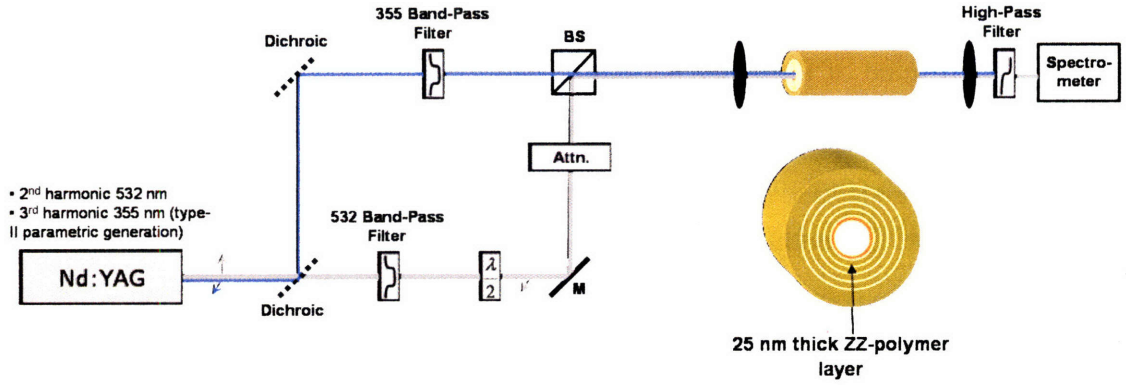

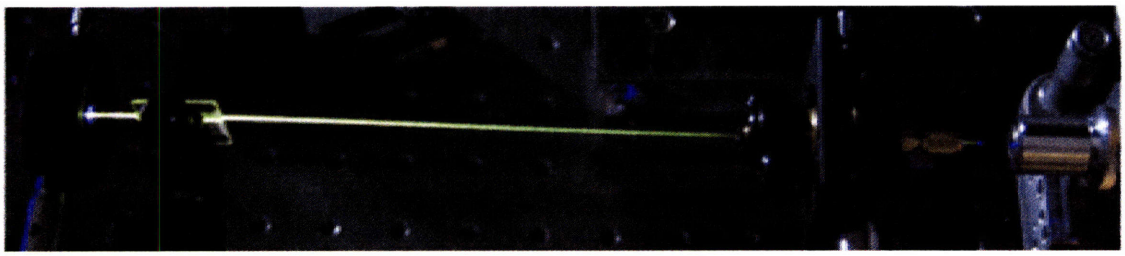

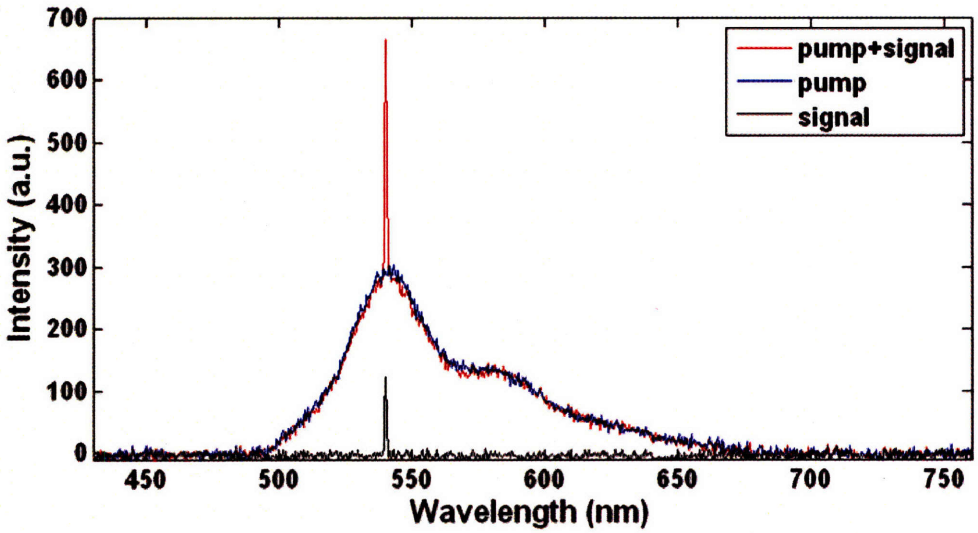

Figure 3.11: a. schematic of the amplifier system showing the beam path of the second (signal) and third (pump) harmonics of the Nd:YAG laser coupling into the hollow-core amplifying fiber and collected at the output by a spectrometer. **b.** An image of the fiber while it pumped with the 355 nm third harmonic. **c.** The spectrum as measured at the output of the fiber in three situation, when only the pump is on – showing the spontaneous emission coming out of the fiber, when only the signal is on, and when both signal and pump are on – showing amplification of ~5dB of the signal.

4 Device Fibers

4.1 Introduction

Heretofore, while novel in their design, the functionalities of our fibers were limited to the classical applications of fiber optics. In the reminder of this work, a new type of fibers is presented, that due to a recent development of fabrication techniques [69] enabled the integration of semiconductor devices into the fiber structure. The combination of conductors, semiconductors, and insulators in well-defined geometries and prescribed sizes, while forming intimate interfaces, is essential to the realization of practically all functional electronic and optoelectronic devices. These devices are typically produced using a variety of elaborate wafer-based processes, which afford small features, but are restricted to planar geometries and limited coverage area. The use of this fabrication approach has been the cornerstone of the electronic revolution, but has had no impact on the optical fiber industry, which relies on a very different fabrication approach. Our goal here is to produce fibers that deliver electronic and optoelectronic functionalities maintained over extended lengths of a fiber. Our strategy in achieving this goal is to use the preform-based fiber-drawing technique that has proven to be simple and yet to yield extended lengths of highly uniform fiber with well controlled geometries and excellent optical and thermal properties [69-72].

The fabrication approach that we adopt thus relies on first preparing a large-scale macroscopic version of the required device in the form of a 'preform' and then reducing it to the desired size through the process of thermal drawing (Fig. 4.1). This process obviously places constraints on the materials that may be utilized. Nevertheless, a set of materials with widely disparate electrical, optical, and thermal properties have been identified and successfully incorporated into fiber-based devices [69]. The fabrication of a preform essentially consists of a semiconductor glass (from the chalcogenide family), metallic electrodes (tin), insulting Poly(ether imide) (PEI) or Poly(ether sulfone) (PES) and multiple alternating thin films of PEI/glass (omnidirectional PBG structure) that are uniform and in intimate contact with each other. Even though the fabrication procedure varies for different structures, the general idea is schematically depicted in Fig. 4.1. A polymer tube obtained from a thin film by rolling on a Teflon rod is consolidated in a

vacuum oven. Four slits are opened to host the metallic electrodes (Fig. 4.1b) and several layers of polymer film are rolled in order to confine the metallic electrodes (Fig. 4.1c). The thin-film deposition technique that we settled on was a thermal evaporation of the chalcogenide glass onto free-standing, commercially-obtained polymer films, allowing us to deposit layers of the chalcogenide glass at high deposition rates (Fig. 4.1d). At the end of that process the preform is consolidated in a zone-defined horizontal vacuum oven while rotating. The preform is then thermally drawn into hundreds of meters of fibers in a three-zone vertical tube furnace (Fig 4.2f).

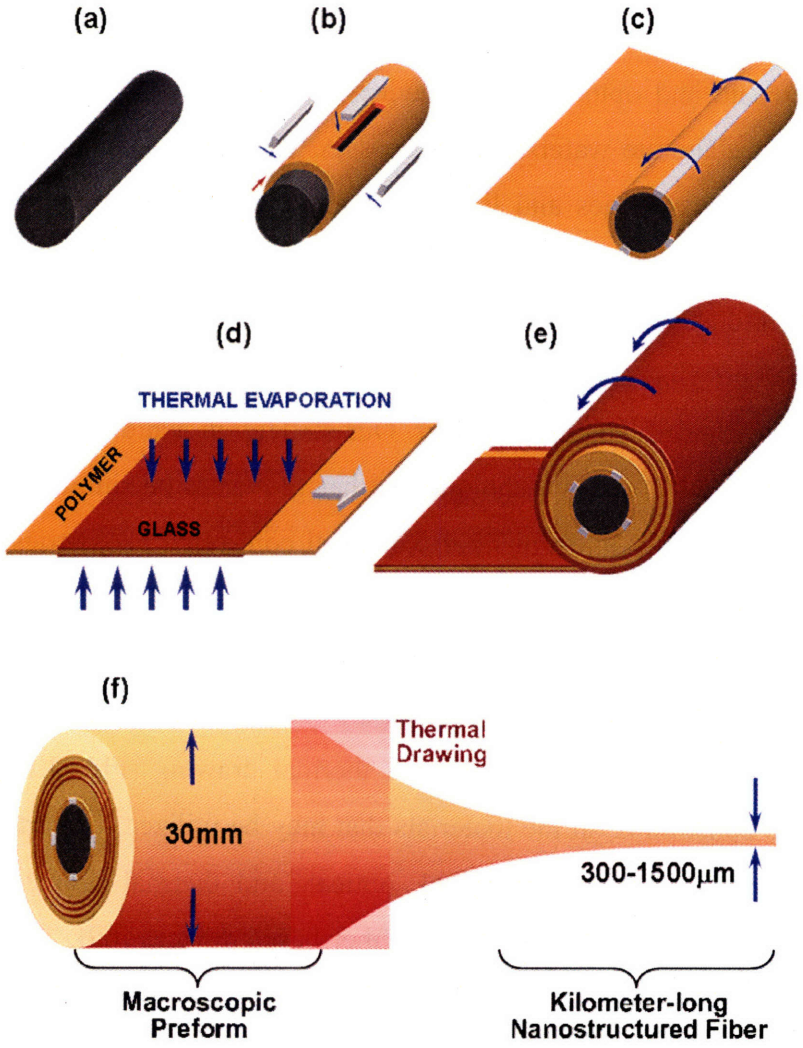

Fig. 4.1. (color) Fabrication steps for nanostructured fibers and fiber devices. (a) An amorphous glass is synthesized from elements in evacuated quartz tube. (b) The glass rod is assembled with an insulating polymer shell and four metal electrodes. (c) A polymer sheet is rolled around the structure to confine the metal conduits inside polymer. (d) A high-refractive-index glass is thermally evaporated on both sides of

meters-long thin polymer film uniformly. (e) The evaporated film is rolled around the structure obtained in part (c). The final structure is then thermally consolidated in a vacuum oven in order to get a solid preform rod. (f) The preform is thermally drawn to kilometer-long mesoscopic-scale fibers containing micro- and nano-structures.

It is important to note that, the device does not demonstrate any functionality at the length scale of the preform. After thermal drawing, a mesoscopic-scale fiber is obtained with the geometry of the preform preserved faithfully after size reduction. At the length scale of the fiber the device becomes functional, and the result is kilometer-long functional fiber devices. In fact, it is conceivable that all the basic components of modern electric and optoelectronic devices (such as junctions, transistors, etc) could potentially be incorporated into fiber-based devices, produced with this simple and yet low-cost technique, on a length scale out of the reach of traditional electronics. An intriguing application of these fibers is the construction of large-area flexible optoelectronic screens, smart fabrics, and artificial skin.

4.2 Integrated Fibers for Self Monitored Optical Transport

The ability to integrate distinct devices into a single circuit enables the realization of systems with higher-level functionality. Here we introduce a new approach to integrating optical, electrical and thermal devices within a single fiber structure. Four solid materials including a polymer insulator, a binary semiconductor, a quaternary semiconductor, and metallic elements are combined into a single fiber perform [69] which is then drawn at high speeds to produce extended lengths of optically and thermally functional fibers. The fibers comprise an optical transmission element which is a hollow-core multilayer cylindrical photonic bandgap (PBG) structure [2,73] designed for the transport of high power radiation at 10.6 microns [5]. Multiple thermal-detection elements are located in the vicinity of the hollow core for the purpose of distributed temperature monitoring. Metal electrodes extend along the length of the fiber in contact with the thermal-detecting elements to deliver an electrical response to the fiber ends. The exponential dependence on temperature of the electrical conductivity of the semiconducting material allows for the discrimination - in real time - between normal transmission conditions and those

which are typical of localized defect formation, thus enabling for the first time a self monitoring high power optical transmission line for failure prediction and prevention.

Index-guided and hollow-core PBG silica fibers have been used for the delivery of high power laser radiation in the near infrared (NIR) wavelengths for industrial and medical applications [74,75]. High power laser light delivery at mid-infrared (MIR) wavelengths for industrial, medical and military applications has been achieved using hollow-core fibers, where light confined using metallic [76], metallo-dielectric [77], or PBG structures [5] has been demonstrated [75,78]. More recently, a polymeric cylindrical PBG fiber was utilized in minimally invasive surgery (MIS) [79]. Regardless of the guiding mechanism or materials used, the containment of such significant power densities within a fiber presents reliability and safety challenges [80,81]. Even a small defect nucleating within such a high power optical transmission line can result in unintentional energy release with potentially catastrophic consequences.

4.2.1 Fiber Structure

We report here on the design, fabrication and characterization of a novel integrated self-monitoring optical transport fiber for MIR transmission. By combining four different materials, namely two amorphous chalcogenide semiconductors (As_2Se_3 and $Ge_{15}As_{25}Se_{15}Te_{45}$ (GAST)), a metal (Sn) and a polymer (polyethersulfone, PES), we prepared a macroscopic preform rod which shares the final fiber geometry. The preform was subsequently heated and drawn into functional fibers. Scanning electron microscopy (SEM) micrographs of a representative fiber are shown in Fig. 4.2a-d. This hybrid fiber has two functional components: (1) a hollow-core photonic band gap waveguide for CO_2 laser transmission (Fig. 4.2a), and (2) three metal-semiconductor-metal (MSM) thermal detectors for temperature sensing (Fig. 4.2b). Each element is an MSM device, with the two electrodes in Fig. 4.2b representing the metal contacts, and the 0.4-μm thin GAST film extending between them is the semiconductor. Figure 4.2c and 4.2d reveal that the drawn fiber preserves the preform geometry during thermal cycling and elongation, a very challenging issue for composite material processing. Because the large distance between each two devices, the operation is rendered independent. Note that the thermal-

sensing devices are not operational at the preform level (because of the large distance between the electrodes) and only become functional after drawing the fiber down to small dimensions. In contrast to our earlier work [69] where we demonstrated a photodetecting fiber and optical transmitting fibers separately, the structure presented here achieves thermal sensing and optical transmission simultaneously.

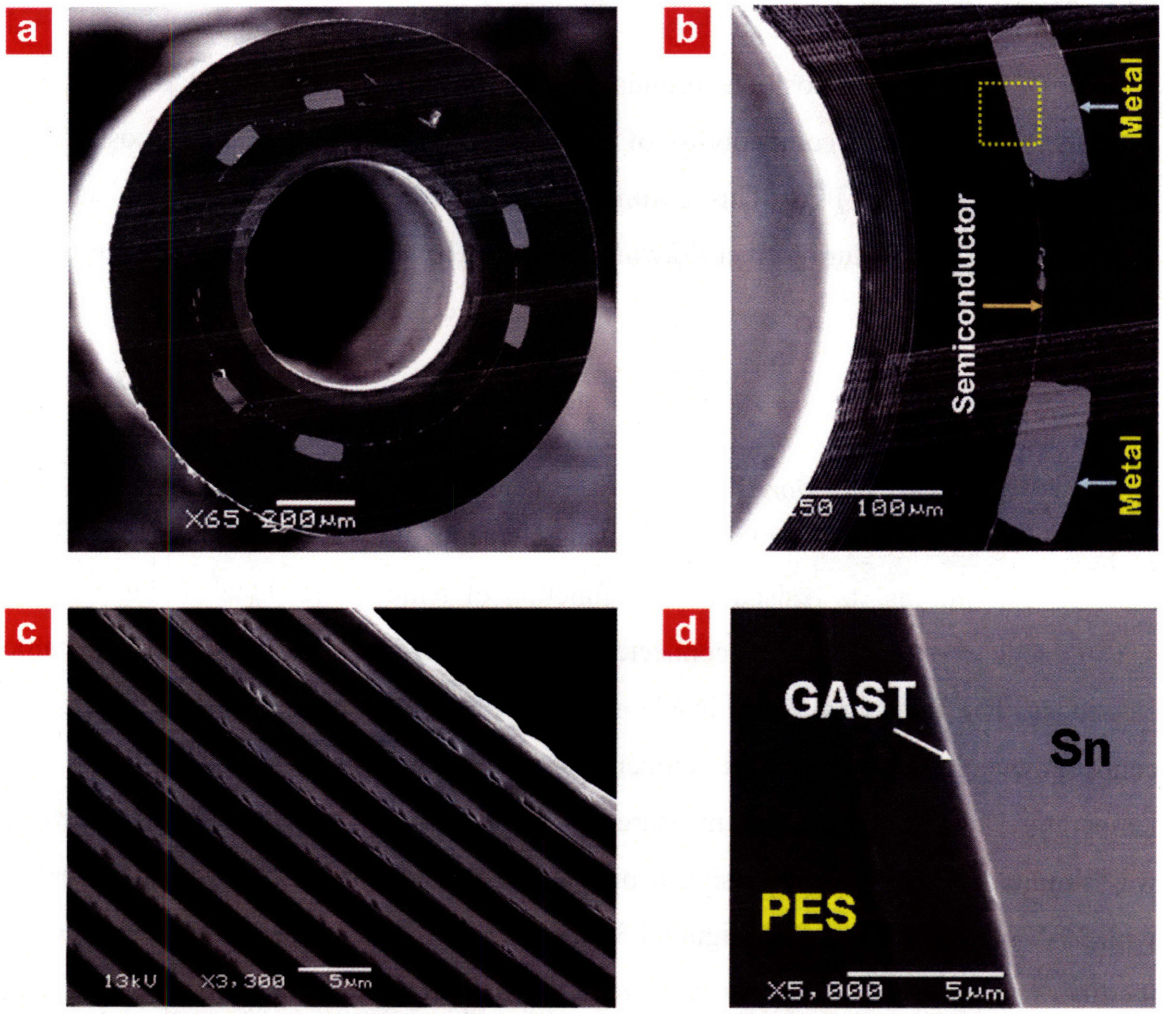

Figure 4.2: SEM micrographs of the hybrid fiber. **a**, The entire cross section of the composite fiber with 560 μm hollow-core, one-dimensional photonic band gap structure, heat sensitive layer, metallic conduits and protective polymer cladding. The outer diameter of the fiber is 1270 μm. **b**, The metal-semiconductor-metal (MSM) heat sensor which consists of a thin amorphous semiconductor ($Ge_{15}As_{25}Se_{15}Te_{45}$) layer and two metal (Sn) electrodes. **c**, 13 pairs of alternating As_2Se_3/PES layers forms a cylindrical mirror exhibiting a photonic band gap centered at 10.6 μm for delivering a CO_2 laser beam. **d**, A magnified micrograph of the box in **b** demonstrating the excellent quality of the insulator-semiconductor-metal interface.

The thermal detection layer described above is a tellurium-containing GAST thin film whose electrical conductivity is highly sensitive to temperature by virtue of the very small thermal activation energy. It is known that very stable glasses can be obtained with around 50% Te content [82,83]. We synthesized a quaternary glass in the Te-rich part of the glass formation diagram. The chosen glass composition $Ge_{15}As_{25}Se_{15}Te_{45}$ was arrived at by optimizing the composition formula $Ge_xAs_{40-x}Se_yTe_{60-y}$ ($10 < x < 20$ and $10 < y < 15$) under constraints of compatibility of glass transition temperature and viscosity with the co-drawn polymer PES. This optimized glass further exhibits enhanced stability against crystallization during fiber drawing and high electrical responsivity to changes in temperature.

4.2.2 Fiber Characterization

We start by characterizing the thermal-sensing elements of a 1270-μm thick, 10-cm long fiber by determining its resistance as a function of temperature. One of the thermal-sensing devices on the fiber was connected to an external circuit through its two metallic electrodes. The fiber was placed inside a hollow quartz tube, with the fiber's electrical connections still intact, and its temperature was raised by a resistive heater. The temperature inside the tube was measured by a thermocouple and the electrical current was simultaneously measured using a pico-ampere meter (Keithly 6487 picoammeter) with 50-V DC voltage applied. Figure 4.3a-b depicts both the temperature dependence of the fiber resistance and the current-voltage (I-V) characteristics of this MSM heat-sensing device. For amorphous semiconductors [84], the resistivity can be expressed as $\rho(T) \propto \exp(\Delta E / k_B T)$ where ΔE is the thermal activation energy, k_B is the Boltzmann constant and T is the absolute temperature. As shown in Fig. 4.3a, the measured resistivity of the GAST thin film as a function of temperature ranging from room temperature to 120 °C fits the above expression with ΔE=0.495 eV. The I-V curves in Fig. 4.3b indicate that the MSM junction has an ohmic behavior at both low and high temperatures.

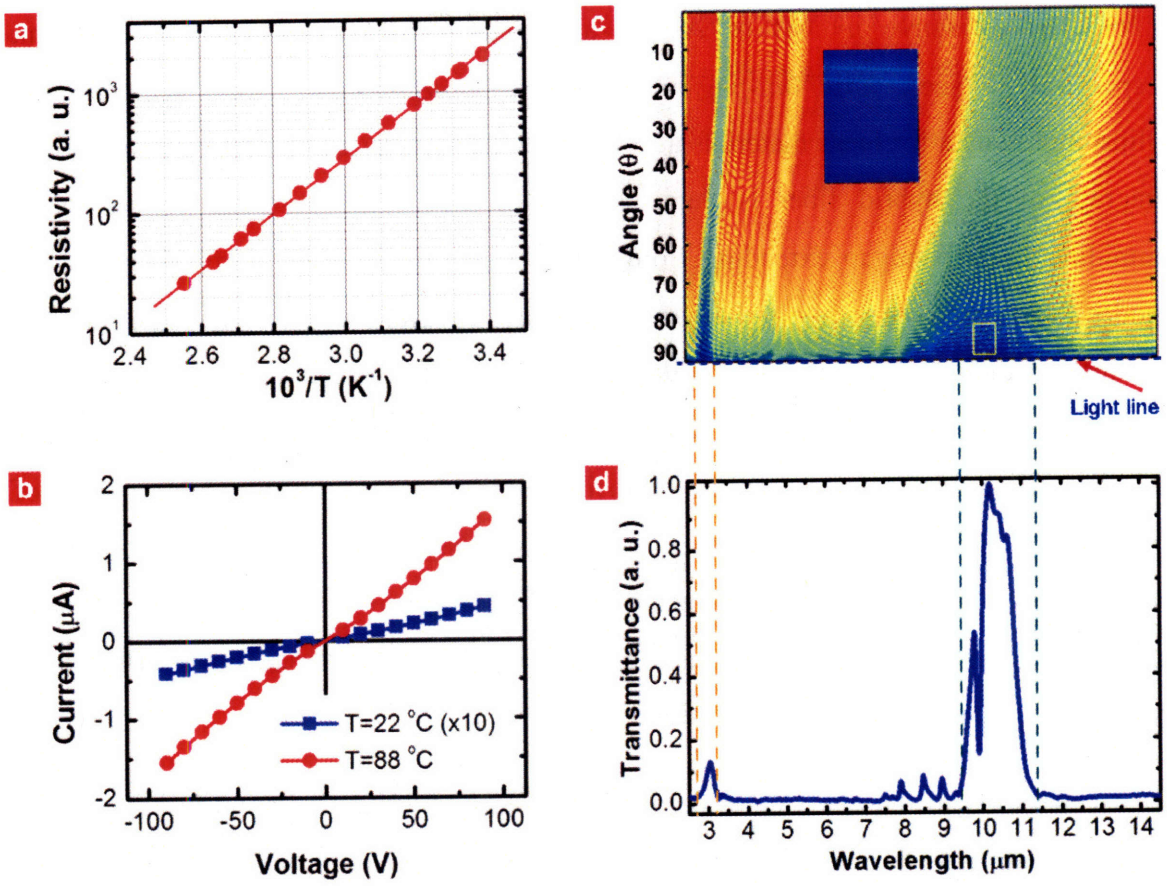

Figure 4.3: Thermal, electrical and optical properties of the hybrid fiber. **a**, The measured resistivity of the GAST thin film in one of the devices on the fiber as a function of inverse temperature. The resistivity decreases more than 2 orders of magnitude when the temperature increases from room temperature to 120 °C. **b**, The current-voltage characteristics of the heat sensor at low and high temperatures. The measured current at 22 °C was multiplied by a factor of 10 in order to enhance visibility. **c**, Calculated band diagram of cylindrical multilayer photonic band gap (PBG) structure. Blue areas correspond to bandgap for the guided modes. Red areas correspond to regions where light couples to radiating modes that are not localized within the fiber core. The inset shows a magnified segment of the guided modes near the light line ($\theta=90^o$). **d**, Measured broad-band transmission spectrum of the hollow core PBG fiber. The primary and third order gaps are centered at 10.6 and 3.0 μm, respectively.

Next, we discuss the optical transport properties of the hybrid fiber. The fiber has a 560-μm-diameter hollow core surrounded by a multilayer structure consisting of 13 bilayers of alternating As_2Se_3 and PES having thicknesses of 1 μm and 1.9 μm, respectively (Fig.

4.2c). The refractive indices of As_2Se_3 and PES are 2.73 and 1.65 at 10.6 μm, respectively (see *http://mit-pbg.mit.edu/Pages/DataBase.html* for spectroscopic ellipsometric data for these materials at NIR and MIR wavelengths). The calculated PBG diagram of the hybrid fiber is depicted in Fig. 4.3c. This structure results in an omnidirectional bandgap extending from 9.4 to 11.4 μm. Blue areas represent guided modes inside the core, while red areas correspond to regions where light is not guided, but instead radiates through the multilayer structure (see 'Band diagram calculation' in Methods). The inset in Fig. 4.3c shows a magnified segment of the PBG diagram detailing the guided modes near the light line (θ=90°), where the dispersion curves of three modes appear as light blue stripes. The transmission spectrum of a 1-m long fiber was measured by a Fourier transform infrared (FTIR) spectrometer (Tensor 37, Bruker) and is shown in Fig. 4.3d. Excellent agreement between the measured (Fig. 4.3d) and the calculated spectrum (Fig. 4.3c) is observed.

Heat generation in the cladding is predominantly due to either radiation leakage of the guided modes into the cladding or to localized defect states. Typical radiation lengths range from a few meters for the low-energy modes, to a few centimeters for higher order modes. However, structural perturbations such as fiber bends and defects tend to increase the overall losses due to coupling to both higher order propagating modes and to localized defect states. In such cases the radiated power from the multilayer structure is absorbed in the polymer cladding and transforms into heat. As a result, thermally excited electron-hole pairs in the GAST layer changes its electrical conductivity. The equivalent conductance of length L of the fiber can be modeled in terms of the local temperature distribution $T(z)$ as $G_{Eq} \propto \int_L \exp(-\Delta E/k_B T(z))dz$.

We demonstrate the delivery of high-power laser light through the hybrid fiber while monitoring the temperature in the fiber. A CO_2 laser (GEM-25, Coherent-DEOS) at 10.6 μm was coupled to the fiber and a 50-V DC voltage was applied to the device electrodes. The input and output optical power as well as the current through the electrodes were recorded. We also measured the power radiated from the fiber outer surface and found it to be negligible with respect to the overall power loss. This suggests that the difference in

power between the input and output dissipates in the fiber cladding and converts into heat, which is further monitored using an infrared (IR) camera (FLIR). We measured the fiber current as a function of the dissipated power ΔP ($\Delta P = P_{in} - P_{out}$) for a 40-cm long bent fiber. We carried out several measurements for decreasing bend radii and recorded the output power, electrical current and temperature distribution (Fig. 4.4a) for a fixed input power of 2 watts. The temperature distribution is found to have an oscillatory behavior [80] due to mode-beating between modes coupled by the bend [18] with a Gaussian envelope centered midway on the fiber bend (Fig 4.4b). Since the mode-coupling strength is inversely proportional to the square of the bend radius [49], an enhancement of the radiated power in the bend is expected, and consequently a raise in temperature. The results are presented in Fig. 4.4c where the increase in current for higher dissipated power (lower radii) is easily observed. The equivalent resistance of the fiber was calculated assuming a Gaussian function for $T(z)$. We found good agreement between the measured values and the calculated response as shown in Fig. 4.4c. Note that the beating amplitude is much smaller then the temperature envelope and therefore its effect on the current is negligible.

4.2.3 Self Monitoring of Failures

The potential usage of this hybrid fiber to cope with the failure of waveguides in high power laser systems by detecting faults *prior* to their occurrence is a very crucial achievement. Such failures normally happen due to distortions in the waveguide structure that result in the appearance of localized defect states. Consequently, high optical energy is coupled from core to the defect state resulting in extensive heat generation. The ability to detect hot spots in the fiber can prevent *catastrophic* failures. However, the existence and location of defects is usually unknown a priori, and monitoring of the temperature along the fiber is required, as achieved by the temperature-sensing device embedded along the entire length of the fiber. The only challenge is to devise a method to obtain an indication of the local defect temperature from integrative current measurements which we proceed to demonstrate. Earlier work on studying the temperature distribution along fibers designed for high power laser delivery has relied on scanning the external fiber

surface using a point thermal sensor [80,81]. This approach obviates the possibility of real time monitoring and is only feasible in a laboratory setting.

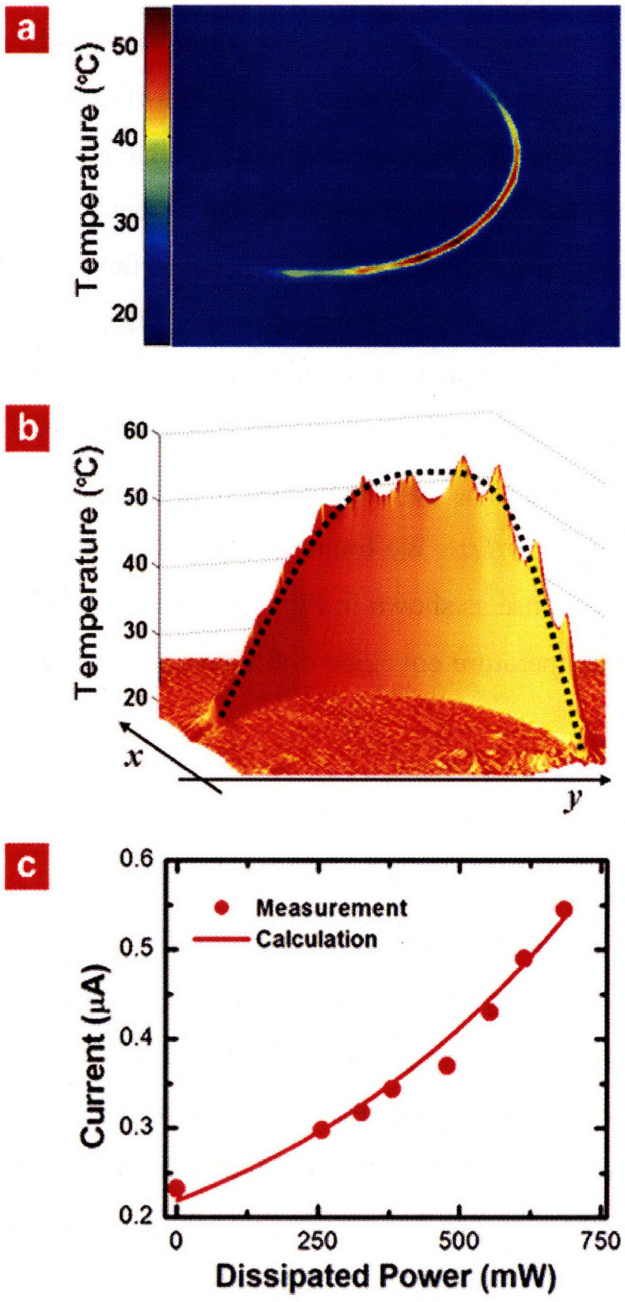

Figure 4.4: Power dissipation along the bent fiber. **a**, Thermal photograph of a bent fiber captured by an IR camera for a dissipated power of ΔP=700 mW ($\Delta P=P_{in}-P_{out}$). **b**, The temperature distribution along the fiber. Periodic variation in the temperature along the fiber is clearly seen. This is due to the fact that (orthogonal) modes are coupled by the fiber bent, resulting in mode beating. **c**, The measured current on the

fiber increases for decreasing bent radii, for a fixed input laser power. The theoretical model agrees well with the measurements.

In order to investigate the self fault detection capabilities of our fiber we measured the current as a function of the dissipated power for defect-free and defective 40-cm long fibers. The defect on the fiber was intentionally generated by burning a small spot on the fiber by a CO_2 laser beam. The temperature distributions along the fibers were recorded using an IR camera for fixed dissipated power as shown in Fig. 4.5a. While the temperature is low and almost constant along the defect-free fiber, a high-temperature spot is observed at the location of the defect in the other fiber. These measured temperature profiles are fitted to Gaussian distributions in Fig. 4.5b. The areas under the two curves are equal as expected since the dissipated powers in both cases are equal. Thus, for fixed dissipated power (equal areas of the Gaussian thermal distribution), defects that are more localized (narrower widths of the distributions) result in a higher peak temperature. It is the exponential relation that exists between the temperature distribution and the measured current that results in the capability of ascertaining whether a certain amount of power loss is attributed to a highly localized defect or a uniformly distributed loss. Because of this exponential relation, the currents generated in these two cases are not equal, even though the amount of dissipated optical power is equal.

The current recorded for these two fibers (by their respective sensitive elements) reveals a dramatic divergence as a function of dissipated power, as shown in Fig. 4.5c. The solid lines are calculated using the temperature data obtained by the IR camera and then implementing the above described model of fiber conductivity. Our model of the electrical response of the heat sensing device indicates an exponential dependence of the local conductivity on temperature. This suggests that a point on the fiber having temperature much higher then the rest would provide the dominant contribution to the current. In fact, for a given dissipated optical power the current would increase exponentially with increase in the peak temperature along the fiber. This significant difference between these fibers for identical dissipated power clearly suggests that a sufficient condition for determining fiber failure from current measurement can be obtained and a damage threshold current can be set.

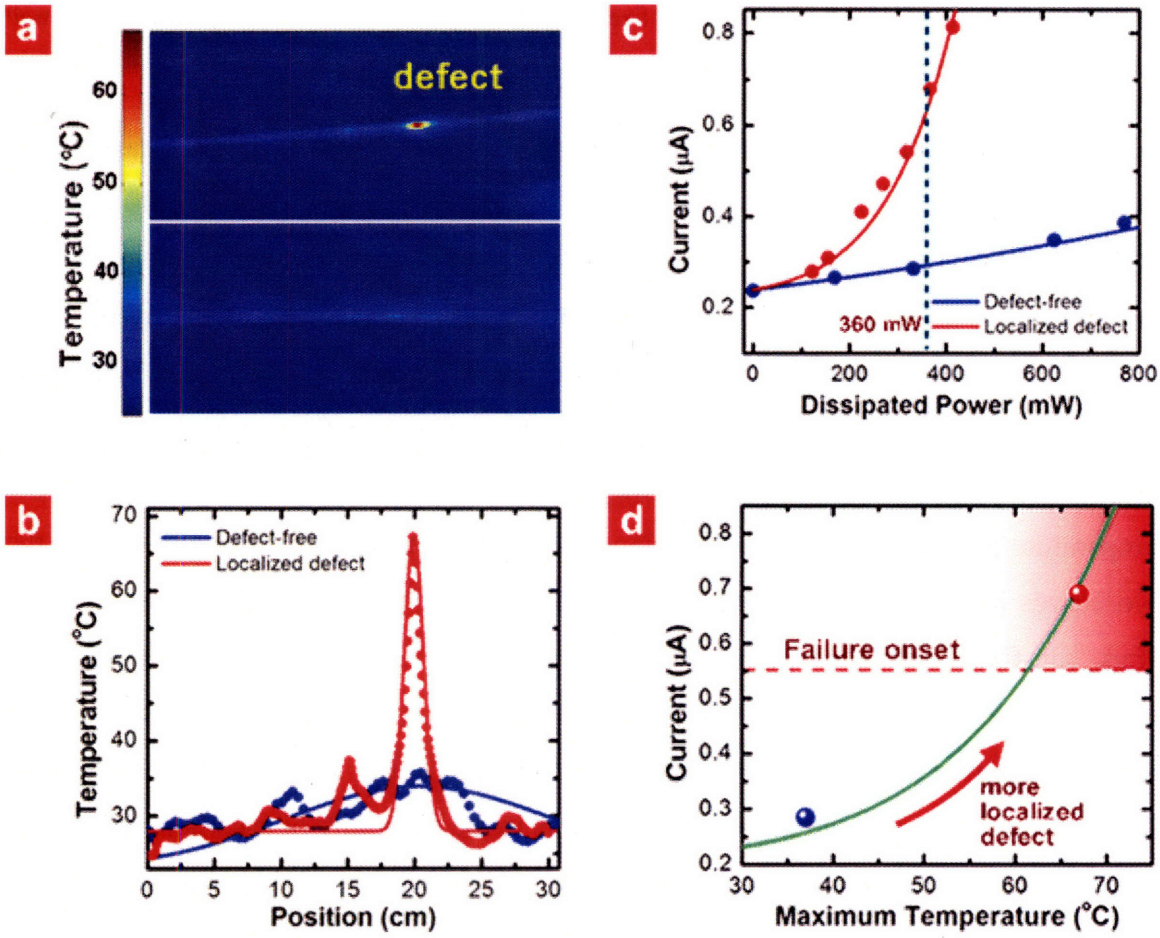

Figure 4.5: High-power laser light delivery through the hybrid fiber and failure prediction. **a,** Thermal photographs of a fiber containing a single localized defect (upper panel) and a defect-free fiber (lower panel) captured by an IR camera. Both fibers carry identical CO_2 laser energy. High power IR light accumulates at the defect site, and consequently heats up the region around the defect. **b,** Temperature distributions along the two fibers shown in **a**. The solid lines provide Gaussian fits to the measured temperature profiles for both cases. **c**, Measured currents as a function of dissipated laser power for defect-free and single-defect-containing straight fibers. The solid lines are calculated by assuming that the temperature distribution along the fiber is Gaussian as in **b**. The current increases dramatically in the defective fiber case. **d**, Calculated current as a function of the maximum temperature along the fiber for a constant dissipated power. A higher maximum temperature corresponds to a more localized defect (narrower temperature distribution at defect site). The two points correspond to the measured current values for defect-free (blue circle) and single-defect containing (red circle) fibers for a dissipated power of approximately 360 mW (vertical dashed line in **c**).

In order to place a failure onset, we calculated the current as a function of temperature distribution width for a given dissipated power (Fig. 4.5d). The maximum temperature is determined by localization properties of the defect, i.e. width of Gaussian distribution (see Fig. 4.5b). In the absence of a localized defect, the current does not exceed a certain threshold value for straight and bent configurations. Hence, when the monitored current exceeds a critical value (failure onset) for a fixed input power level, it is most likely to be due to heat-generated-defects on the inner surface of the fiber.

In conclusion, we have introduced a new approach to integrating multiple materials and a multiplicity of functional devices into a single fiber which is drawn from a macroscopic preform at high speeds. We have incorporated two different semiconductors, an insulator and a metal in the same fiber preform and have codrawn it with no structural deformations while preserving the initial geometry. The thermal-sensing devices embedded in the fiber structure become functionalized only upon drawing down to small cross-sectional dimensions. The utility of this approach was demonstrated by integrating a photonic bandgap optical transport device with multiple thermal sensors within a single fiber. The thermal sensing layer along the fiber enabled electrical monitoring of temperature changes within a high power transmission fiber allowing for the discrimination - in real time - between normal transmission conditions and those which are typical of localized defect formation. The ability to integrate optical transport and thermal monitoring for failure prediction is of paramount importance if high power optical transmission lines are to be operated safely and reliably in medical, industrial and defense applications. This work may also pave the way for new types of fiber sensor devices.

5 Optical-Field Detection Using Geometric Fiber Constructs

5.1 Introduction

The novel fiber structure described in the previous chapter has remarkable properties in it own right. Nevertheless, interesting and unique possibilities stem from the construction of functional fabrics using such optoelectronic fibers. The fibers are both flexible and mechanically tough, and can thus be woven. Furthermore, interesting device applications follow not only from the ability to engineer the single-fiber properties, but also from the specifics of fiber arrangements into larger assemblies. For example, in constructing a 2D optical detector array, a desired resolution of $N \times N$ pixels per unit area would require N^2 point (dimensionality zero) detection elements. A fabric woven out of linear 1D fibers, on the other hand, provides a grid structure which in turn can be used to localize an illumination point on a surface—but with detection elements of only order N (as suggested by comparing figure 5.1a and b). Moreover, by overlapping layers of this fabric, one could even ascertain the direction of incoming illumination.

We envision that arrays of photodetecting fibers can replace traditional optical systems through the use of a novel geometric approach to optical detection. Measurements of optical fields are typically performed using sequential arrangements of optical components such as lenses, filters, beam splitters in conjunction with planar arrays of point detectors placed on a common axis [85]; both the human eye and the photographic camera are examples of such systems. A generic conventional optical system is shown in Fig. 5.1a, involving a single lens and a planar optical detector array. In the limit of geometric optics (where light is represented by rays) the role of the lens is to apply a specific linear transformation **T** to the incident light rays that results in the mapping of an incoming vector to an outgoing vector which is subsequently detected by the detector array. The approach described in this section involves the implementation or, in some cases, the emulation of arbitrary optical systems through the spatial *geometric* arrangement of photodetecting fibers in 3D constructs. A geometric arrangement of 1D photodetectors is shown in Fig. 1b which is capable of detecting the direction of an incoming ray. The linear transformation **T** corresponding to the action of a lens [85] is

then computationally applied, allowing one to answer the question of what direction would the outgoing ray emerge were there to be a lens in its path. Thus, in the geometric optics limit, the lens-detector optical system is computationally emulated by the spatial fiber arrangement.

Note that although an optical detector obstructs the path of a ray since light detection is, in general, a destructive process, nevertheless, an optical array made sufficiently sparse will offer little disturbance to the incident field. The first array in Fig. 5.1c registers the location of the incident beam, which continues its path, only slightly perturbed, to the second web which records the new position of the beam. One may then easily determine the angle of the beam from knowledge of the two locations and the distance d between the planes of the webs, which, along with the position of the beam in a plane, constitutes a complete representation of the ray in the limit of geometric optics [85]. The angular resolution of this arrangement is determined by the ratio of the spatial resolution of a web to d, and the angular bandwidth is limited by the ratio of the size of the array to d.

A physical realization of such an arrangement is shown in Fig. 5.1c where two 32×32 arrays, or 'webs', are used to detect the direction of a beam of light. The arrays are constructed of one-dimensional (1D) photodetecting fibers produced by a fabrication process that enables the incorporation of insulators, conductors, and semiconductors in mesostructured fibers combining both optical and electrical functionalities [69]. Specifically, the fibers we make use of here are constructed of a photoconductive glass core contacted to metal electrodes that run along the length of the fiber and then surrounded by a protective, transparent polymer cladding. A micrograph of the fiber cross-section is given in Fig. 5.1d. The resulting fibers are arbitrarily long, light-weight, flexible, 1D light-sensitive elements that produce an electrical signal, in the form of a change in current in an external circuit, when light impinges on their external surface [41, 86].

This new geometric approach to optical field measurements lifts some of the fundamental limitations associated with conventional measurement systems and, moreover, enables access to optical information on unprecedented length and volume scales. These tough, polymeric, photodetecting fibers [41] are woven into light-weight, low-optical-density, 2D and 3D constructs that measure the basic attributes of

electromagnetic fields on very large areas. The precise geometric construct is tailored to address specific measurement requirements and, in particular, does not necessitate an optical axis. The problem of optical field measurement is therefore transformed from one involving the choice and placement of lenses and detector arrays to that of designing geometrical constructions of polymeric, light-sensitive fibers. These fibers, moreover, enable the realization of large-area optoelectronic functional surfaces, presenting the opportunity to deliver novel semiconductor device functionalities at fiber-optic length scales and cost.

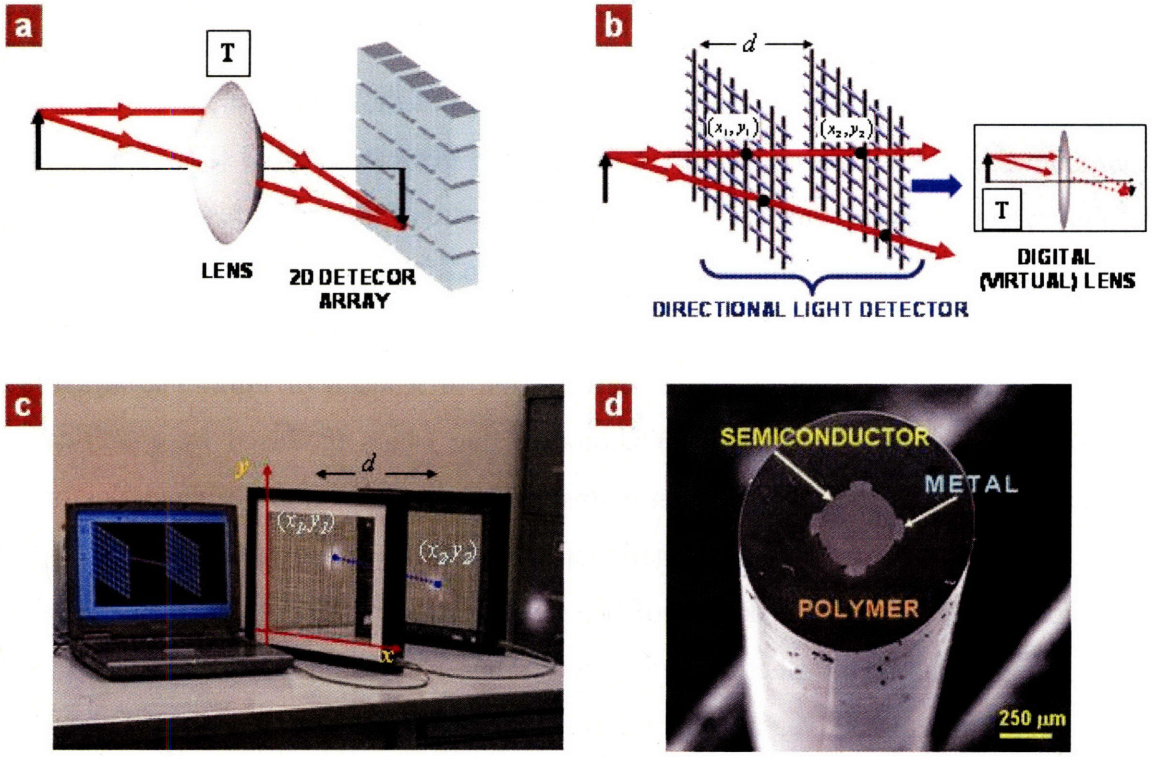

Figure 5.1: Photodetecting fiber webs. **a**, A typical optical imaging configuration. A lens implements an optical transformation **T** that results in mapping incoming rays to outgoing ones. A 2D detector arrays then detects the intensity distribution. **b**, Two transparent, planar detector arrays constitute a directional light detector. Given the location and direction of the ray, one may implement the optical transformation of the lens **T** digitally on a computer. **c**, A physical implementation of a directional light detector consisting of two planar fiber webs, displaying the path of a ray of white light in three dimensions on the computer screen. The two planar fiber webs detect the positions of the two intersection points that determine the beam direction. **d**, A scanning electron microscope micrograph of a fiber cross-section showing four electrodes in contact with a photoconductive, semiconducting glass core, surrounded by a protective polymer cladding.

5.2 Fiber Photodetectors

A well known characteristic of crystalline semiconductors is the change of their electrical conductivity under optical illumination due to the transition of electrons from the valence band to the conduction band through the absorption of photons having sufficient energy. Although the lack of long-range order in amorphous media, such as chalcogenide glasses, renders the Bloch theorem (and thus the crystal momentum k), irrelevant, the energy-band diagram is still a useful conceptual tool that may be used as an approximation to describe the density of electronic states. Amorphous materials possess an energy band gap between the valence and the conduction bands, but in contrast to intrinsic crystalline semiconductors, the density of states is not zero in the gap. Indeed, the random electronic potential in any amorphous structure is responsible for an exponentially decaying density of states that extends out of the conduction and valence bands into the band gap, called Urbach's tail, corresponding to localized states below the mobility edge. Moreover, defect states, such as dangling bonds, that can be present at energies generally corresponding to the center of the gap, are responsible for the characteristic properties of chalcogenide glasses such as p-type conductivity and the pinning of the Fermi level [87].

When light impinges on an amorphous semiconductor, such as that in the fiber core described above, holes from the valence band, as well as from localized states inside the band gap, can gain sufficient energy by absorption of a photon to transit to an extended state in the conduction band, a process not dissimilar from what occurs in the crystalline case. It is interesting to note, however, that there is no sharp energy edge for excitation of electron-hole pairs in amorphous semiconductors, due to the non-zero density of states in the gap. These materials are therefore sensitive to light over a wide range of wavelengths, and are also suitable for sub-bandgap detection, which has important consequences for our fiber-based photodetectors.

Returning to the above described fiber device, when the metal electrodes (that interface with the chalcogenide glass core along the entire length of the fiber) are connected to an external circuit and a voltage is applied, a current determined by the conductivity of the glass in the dark will flow. The fiber undergoes a change in electrical

conductivity when externally illuminated since electron-hole pairs are created, driven apart by the electric field, that contribute to the current flowing through the fiber. The striking originality of this new type of light-sensing device, besides its low cost and simplicity of production, resides in its geometry. It is the first one-dimensional (1D) distributed photodetector that detects light incident on it from any direction at any point along its entire length which may extend to hundred of meters. Producing a photodetecting line with current point photodetectors (of dimensionality 0) would require a large number of devices, and the price of their assembly scales with the detection length required. An inherent disadvantage of an integrating 1D photodetector such as our fiber, however, is that no information about the location of the incident beam along the fiber is obtained. This may be overcome, however, by constructing two-dimensional (2D) assemblies of fibers to localize a point of illumination in a plane.

5.3 Optical Intensity Detection Using Fiber-Webs

We now proceed to demonstrate a more sophisticated task, namely the detection of an arbitrary optical intensity distribution using a planar fiber web. An important observation brings to the fore which body of theoretical work is of relevance to this problem. Since each fiber detects the incident intensity distribution along its whole length, the intercepted power (and, consequently, the electrical signal produced) is therefore a line integral of the intensity distribution along the fiber. A fiber, of length L and diameter Δ ($\Delta << L$) placed along the line $x\cos\theta + y\sin\theta = t_1$ in an optical field having a two-dimensional intensity distribution $I(x,y)$, as illustrated in Fig. 5.2a, generates a photocurrent that is proportional to the intercepted optical power $P_\theta(t_1)$, given by

$$(5.1) \qquad P_\theta(t_1) = \iint\limits_{\text{fiber area}} dxdy\, I(x,y) \approx \Delta \iint dxdy I(x,y)\delta(x\cos\theta + y\sin\theta - t_1)$$

where t_1 is the intercept of the fiber with the t axis, which makes an angle θ with the x axis.

Consequently, the measurements performed by a set of parallel photodetecting fibers form a 'parallel projection' of the incident intensity distribution, a term used in the literature on computerized axial tomography (CAT) [88]. In that context it refers to the

measurements performed by a linear array of point detectors placed on one side of a 2D object of interest, when a linear array of point sources (*e. g.*, X-rays) is placed on the opposite side of the object. In our case, each fiber records the line integral of the intensity distribution of the optical field along its length. An example of a parallel projection produced by a fiber web is shown in Fig. 5.2b, where a 32×32 fiber web (of dimensions 24×24 cm^2) intercepts an image of a letter 'E' and the two orthogonal projections obtained by the rows and columns of the web are displayed. The image is produced by a white-light lamp (Xe-Hg) illuminating a transparency with dimensions 14×14 mm^2 placed at a distance of 1.2 m from the web. No lens is needed to form an image of the object transparency in this case because of the large dimensions (relative to the wavelength of light) used, highlighting the unique advantage of a detector array having such a large area.

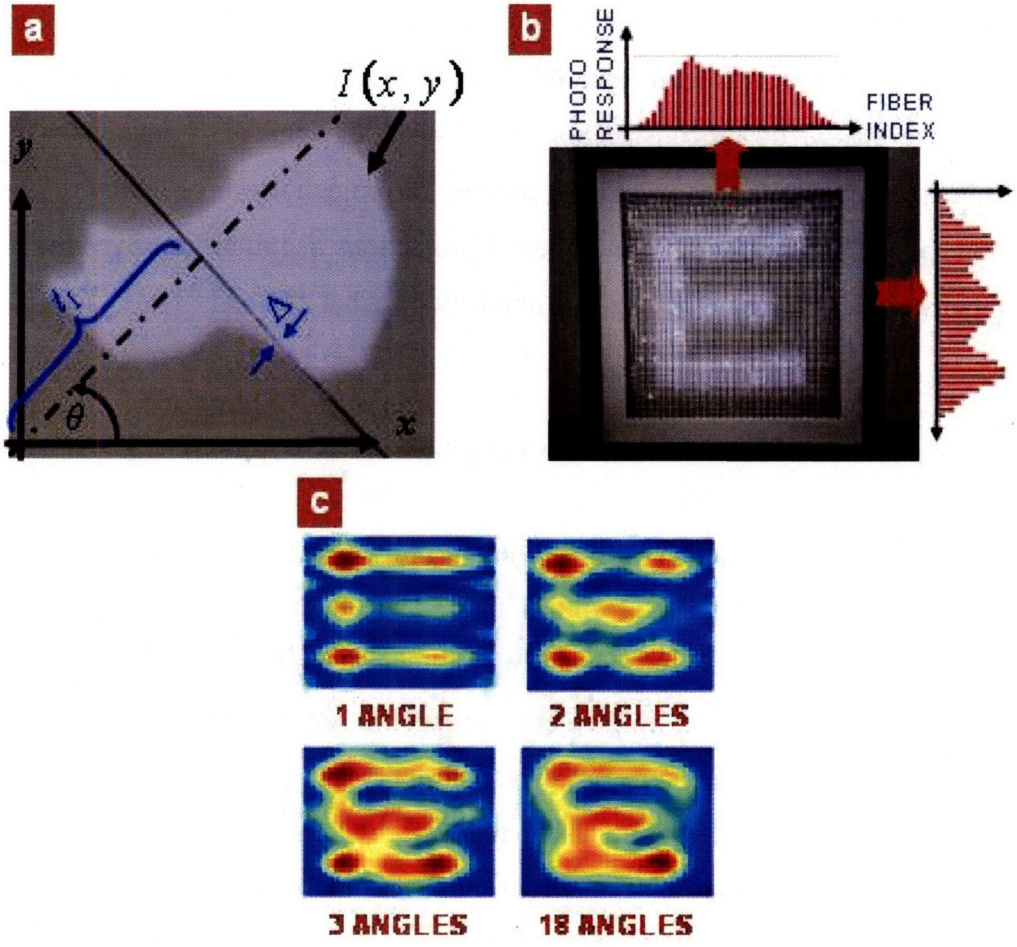

Figure 5.2: Reconstructing an arbitrary optical intensity distribution with a planar fiber web. a, A photodetecting fiber of thickness Λ detects the line integral of the arbitrary incident optical intensity distribution, *I(x,y)*. **b**, An image of the letter '**E**' is projected onto a 32×32 fiber web of dimensions 24×24 cm^2. The detected electrical signals from the web rows and columns (constituting 2 orthogonal projections) are also shown. The image of the letter '**E**' seen here is formed on a white sheet placed behind the transparent web. **c**, Reconstructions of the incident intensity distribution, obtained using the backprojection algorithm, are shown with increasing number of projections. These projections are obtained by rotating the object transparency. 1 angle: 0°; 2 angles: 0°, 45°; 3 angles: 0°, 30°, 60°; and 18 angles: 0° to 85° in 5° steps.

These two apparently different arrangements (CAT and our fiber webs) are, surprisingly, mathematically isomorphic, allowing us to import the theoretical foundations of CAT for use in the problem at hand. In particular, we employ the backprojection algorithm (Radon transform) [88], commonly used in CAT, to reconstruct an estimate of the impinging optical intensity distribution. In the case of fiber webs there are several strategies to achieve this: (1) rotating the fiber web; (2) using adjacent or interleaved fiber webs, each rotated by an angle with respect to each other; or (3) rotating the object that is imaged. In Fig. 5.2c we show the reconstruction results of the image, obtained using the backprojection algorithm, with increasing number of projections recorded by rotating the object transparency. Increasing the number of projections acquired improves the fidelity of the reconstructed image to the incident intensity distribution.

5.4 Optical field detection and lensless imaging

While a single planar fiber web can detect the intensity of an incident optical field, two such webs can be used to detect both the field amplitude and phase, which constitute a complete representation of a scalar optical field. The effect of any optical device may then be simulated on a digital computer by manipulating this information about the field. The human eye, for example, implements a specific transformation (that of an iris followed by a lens) with variable parameters, before detecting a 2D intensity distribution. One could also prepare a hologram using this information, or conceivably implement object-recognition algorithms that benefit from the availability of the complex optical field instead of relying on a 2D intensity image.

The ability to reconstruct the field enables *lensless* imaging of an object by detecting the diffracted intensity image and then using *phase retrieval algorithm* [35, 89-93] in order to gain complete information on the field. We then can calculate numerically the field in any other plane by using the Fresenl transform. The idea proceeds as follows. We use two planar fiber webs, located at two distinct diffraction planes, and obtain the incident 2D intensity distributions from both (by means of the CAT algorithm outlined above); we then implement the phase retrieval algorithm to retrieve the phase of the wave front; knowing the complex field at the first web, we can 'back-propagate' the wave front computationally until an estimate of the object is obtained.

The feasibility of this approach is demonstrated by producing an estimate of the amplitude and phase of an optical wave front produced by a letter '**E**' having an overall size of 750×750 μm^2 (with features size of 150 μm; the object was a chrome mask on a glass substrate) illuminated with laser light having a wavelength of 830 nm. The 2D intensity distribution data obtained by a fiber web at two different locations in the far-field of the object is depicted in Fig. 5.3b. We implemented the phase retrieval algorithm on the two obtained intensity distributions to reconstruct the object wave front. We define an error metric $\Theta = \int d\mathbf{r} \sum_{n=1,2} \left(|G_n(\mathbf{r})|^2 - I_n(\mathbf{r}) \right)^2$ describing the distance between an estimate $|G_n|^2$ and a measured intensity distribution I_n in both diffraction planes, $n = 1, 2$. The distributions in the two diffraction planes are related to the object field distribution $g(x, y)$ through the Fresnel transform $\Im$, $G_n(u,v) = \Im\{g\}(u,v)$. The Nyquist frequency for such system is *1/L*, where *L* is the size of *g* (in one dimension) and the sampling rate corresponds to fiber spacing < $2\pi d/kL$, where λ is the wavelength and *d* is the distance betweeen the object and the array. The array size sets a cutoff for the spatial frequencies and therefore determines the sharpness of the reconstructed image. The phase retrieval algorithm used requires the minimization over the metric Θ with respect to the set of two-dimensional variables $\{g(n,m)\}$, where *n* and *m* are discretized spatial coordinates. The minimization is performed iteratively by repeating the following steps: (1) Calculate G_n in both planes using the previous estimate of *g* (an initial guess for *g* is needed in the first iteration). (2) Calculate Θ and its partial derivatives with respect to *g(n,m)*. (3)

Using the gradient-search method, find the next estimate of g (with smaller error). These steps are repeated until the change in the error metric is limited by the system noise.

We comment on the extent of the disturbance to the optical field produced by absorption of a portion of the impinging optical power by the fiber array. Consider the general situation depicted in Fig. 5.3a where an optical field $E_1(x,y)$ incident on the first array is perturbed by the first planar array before propagating to the plane of the second array where the field is $E_2(x,y)$. To investigate the limits placed on this procedure by diffraction caused by the fibers in the first array, assume that all the fibers in the first array are identical, have an effective width δ and are arranged on a uniform square grid with separations Δ. The incident field, $E_1(x,y)$, is modulated by the 2D transfer function of the array, $T_{2D}(x,y)$, such that the field directly after the array is $E_1(x,y)\cdot T_{2D}(x,y)$. The array transfer function is separable, $T_{2D}(x,y)=T_{1D}(x)\cdot T_{1D}(y)$, with $T_{1D}(x)=1-\text{rect}\left(\frac{x}{\delta}\right)\sum_{n=-N}^{N}\delta(x-n\Delta)$; $\text{rect}\left(\frac{x}{\delta}\right)=1$ when $|x|\le\frac{\delta}{2}$ and is 0 elsewhere; $2N+1$ fibers are assumed along one direction. We assume that the first fiber array is large enough such that it captures most of the incident field $E_1(x,y)$. This allows us to let N formally become infinite, and the Fourier transform of T_{1D} becomes

$$\text{FT}\{T_{1D}\}(u)/2\pi=\delta(u)-\frac{\delta}{\Delta}\cdot\frac{\sin u\delta/2}{u\delta/2}\sum_{n=-\infty}^{\infty}\delta_D\left(u-2\pi\frac{n}{\Delta}\right) \tag{5.2}$$

where $\delta_D(u)$ is the Dirac-delta function. Note that the zeroth-order component in the second term (n=0) on the right-hand side of Eq. (5.2) is weighted by a factor of δ/Δ with respect to the first term. After propagating a distance d to the second array, the diffracted field $E_2(x,y)$ is given by the Fresnel integral of the modulated incident field, $E_2(u,v)=\Im\{E_1T_{2D}\}(u,v)=\Im\{E_1\}(u,v)\otimes\text{FT}\{T_{2D}\}(u,v)$, where $\otimes$ stands for the convolution process (we have ignored an unimportant overall phase term). Two conditions need to be met: (1) the size of the second array should be smaller than the separation between the delta functions in the second term on the right-hand side of Eq. (5.2), and (2) $\delta/\Delta << 1$ (by using fibers of thickness much smaller then the fiber spacing) such that the contribution of the zeroth-order second term in Eq. (5.2) becomes negligible; $E_2(x,y)$ becomes approximately the Fresnel transform of E_1.

A Gaussian beam, from a Ti:Sapphire laser tuned to a wavelength of 830 nm, is incident perpendicularly on an amplitude mask with the letter '**E**', generating a Fresnel diffraction pattern 12 cm away from the mask with size of ~ 1 mm, and a Fraunhofer diffraction pattern 80 cm away with size of ~ 6.5 mm. In this proof-of-principle experiment, we magnified those patterns to match the array size. We implemented the above described phase retrieval algorithm using an optimization routine from MATLAB©, and optimized the error function to obtain the reconstructed field at the plane of the mask. The iterative process converged after less than 20 iterations to an error of less than 1%. Having an estimate of the amplitude and phase of the field in one plane, one can use to propagate the field to *any* other plane, and a "focused" image is observed at a distance that matches the location of the object We compared these results to a theoretical model that numerically propagates the field from the object, using the object distribution modulated by the incidencet laser beam (as captured by a Vidicon camera) and taking into consideration the 32×32 discretization of the diffracted fields at the measurement planes. The calculated images and the reconstructed fields are given in Fig 5.3c.

In order to verify the fidelity of the amplitude and phase estimation, we use the acquired complex wave front to 'propagate' the field computationally at distances receding from the first web towards the object. A set of these computed estimates is shown in Fig. 5.3b. The estimates are blurred until we approach the location of the object where a clear image is formed. For comparison, we used scalar diffraction theory to calculate the diffracted field of a letter 'E' modulated by a Gaussian beam at the two measurement planes, the resulting amplitudes, truncated to the array size, are shown in Fig. 3. We then used the phase retrieval algorithm to reconstruct the object at those same planes receding from the first array.

This approach may eventually become useful in optical imaging when a larger number of fibers are included in the web to form images of objects with more detail. Note that this system has an infinite depth of focus, i.e., an image is formed of the object regardless of the distance of the object from the webs, provided that the diffracted field at the locations of the two webs, is intercepted. Furthermore, the image reproduces the object with its real physical dimensions and also determines its physical distance from the webs. In principle, by virtue of obtaining a complete description (both the amplitude and

phase) of the electromagnetic field, this approach may be used to image 3D objects that are translucent enough so that excessive occlusion does not occur. A distinct approach relies on the use of a single dense array having a higher fill factor. While such an array will result in a strongly perturbed field at the second plane, the reconstruction can still be achieved using a single intensity measurement [94] without the need for a measurement at the second plane. This procedure requires that an over-sampling requirement be satisfied: the sampling of the diffracted field must be dense enough to enable the reconstruction of the autocorrelation function of the object [91, 95]. Moreover, one can arrange for the photoconductive glass core in the fibers to be responsive in different regions of the optical spectrum.

There are several unique features of our approach that are not captured by other techniques that sample a 3D electromagnetic field such as photorefractive crystals, for example. First, our fiber webs are 2D manifolds embedded in 3D space, and therefore they capture much less light than a truly 3D volumetric sampling detector. This serves to reduce the amount of acquired data and minimizes the absorbed power. Second, no optical readout is required, as is the case in photorefractive crystals, since information is acquired directly in the form of an electrical signal. Most importantly, the size of our fiber webs can be made arbitrarily large, an advantage not shared by any other rival technology.

Finally we comment on the weight of such arrays. Assume a 1×1 m^2 array formed of 1-mm diameter fibers with 1-cm spacing providing 10,000 detection points. With average density of the fiber materials being 1.84 gm/cm^3, the overall weight of the array is 0.289 kg, which is negligible when compared to the weight of any traditional optical component of comparable size. Note that using fibers with smaller diameters allow for weaving denser arrays.

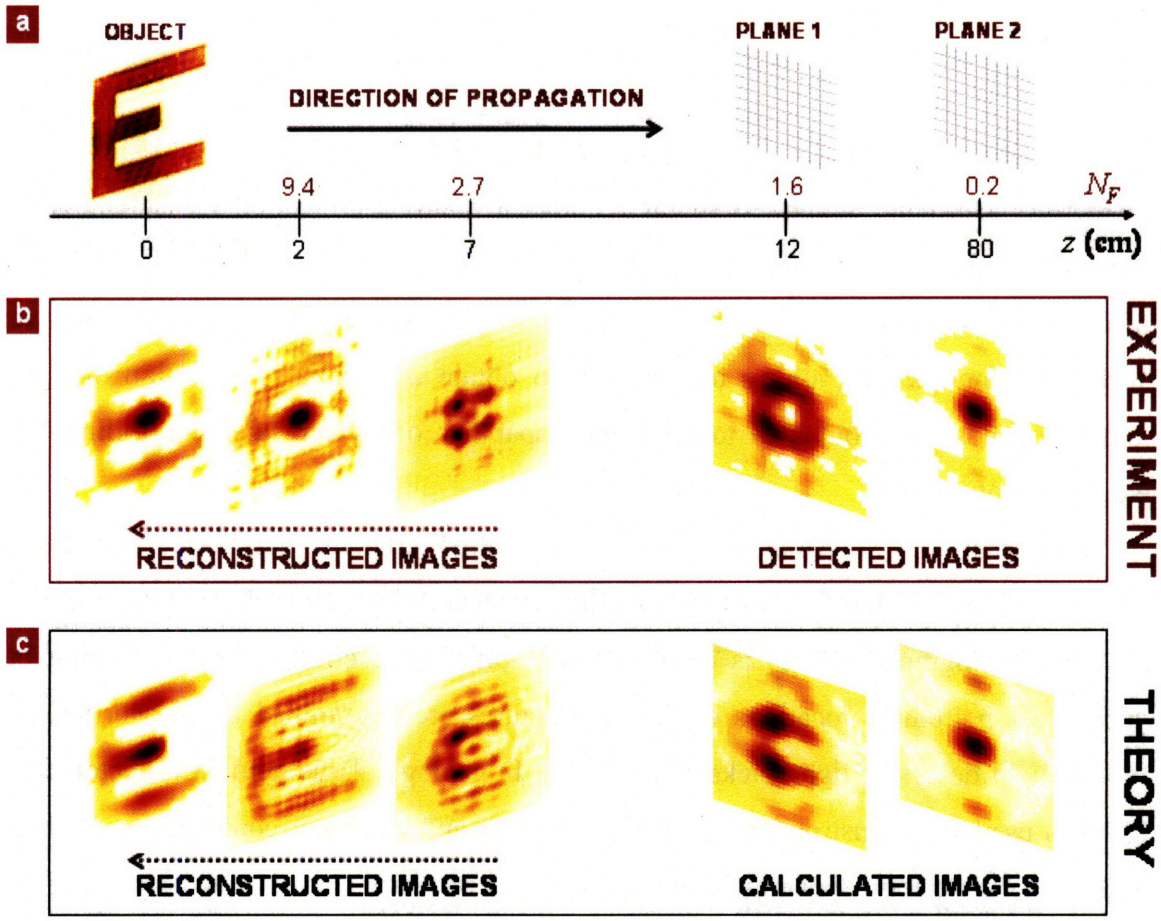

Figure 5.3: Non-interferometric lensless imaging using two fiber webs. a, An object (letter '**E**') is illuminated with a laser beam (the image of the object is captured with a Vidicon camera) and the diffracted fields propagate to the planes of two 32×32 planar fiber arrays at two different locations (Fresnel zone, 12 cm, and Fraunhofer zone, 80 cm, shown on the right, first row) are obtained using the fiber webs. The Fresnel number N_F [1] is also given. **b**, Two intensity distributions are measured. The phase retrieval algorithm is used to obtain back-propagated images in the direction receding from the webs towards the object (the object reconstruction is at at 0 cm, shown on the left). The reconstructed images are blurred, but a clear image is obtained at the location of the object. **c**, The second row shows the results of theoretical reconstructions with the phase retrieval algorithm when using near- and far-field diffraction patterns that were obtained from the measured illuminated object distribution.

5.5 Dynamic Distributed Detection

5.5.1 Modeling the fiber as a transmission line

The detection scheme suggested so far requires a multiple-projection measurement in order to reconstruct any arbitrary intensity or field distribution. In practice, rotating the object or alternatively the detector to obtain the data might pose a problem. Here we suggest a technique that allows us not only to obtain the spatial distribution of light incident upon a fiber but also to have the capability of dynamically controlling the detection resolution.

The reconstruction of a spatial distribution of a layered structure that is accessible from only one end surface has been studied recently in several disciplines. In biology, Optical coherence tomography (OCT) is employed for noninvasive cross-sectional imaging in which the longitudinal locations of tissue structures are determined by measuring the time-of-flight delays of light backscattered [96]. In geology, Time domain reflectometry (TDR) is used to reconstruct the dielectric constant and electrical conductivity of soils having different electrical conductivities [97].

One can harness these same techniques to reconstruct the spatial light distribution of our photo-detecting fiber by noting that this structure can be regarded as a *transmission line*. The reasoning behind it is the observation that a fiber with electrodes surrounding a uniform core supports the propagation of transverse-electromagnetic (TEM) mode. Figure 19a shows a calculation of the electric field distribution in a cross section of a fiber with two electrodes surrounding a glass core. This calculation was made by FDTD techniques using Femlab and clearly shows the existence of TEM field solution to that structure. We note that for a fiber having a thin-film detecting layer as shown in Fig. 5.4b (with insulating polymer core) the structure would still support a TEM mode. Here however, a perturbation to the structure is introduced by the conductivity of the glass layer.

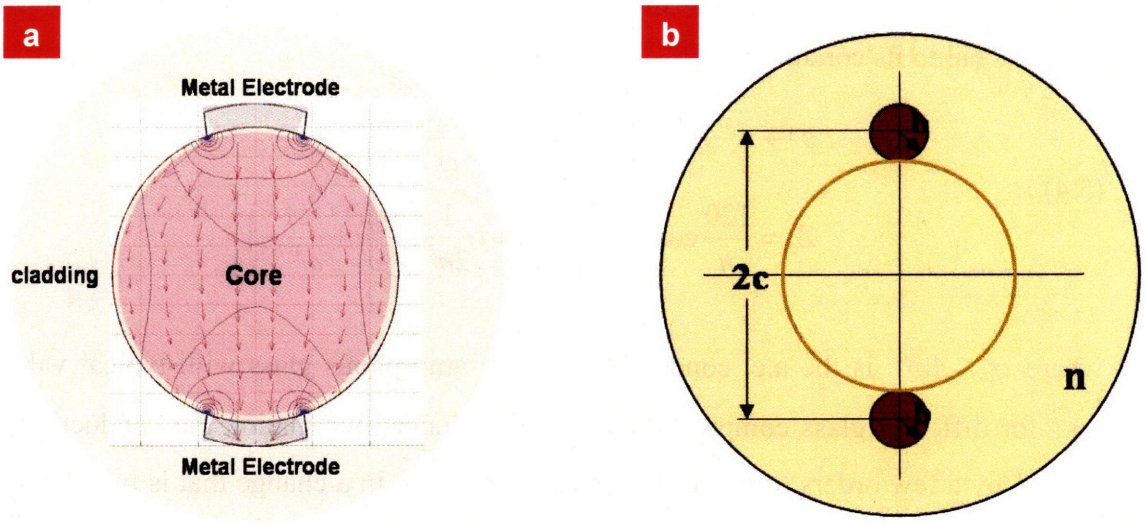

Figure 5.4: The Modeling of one-dimensional fiber detector as a transmission line. **a.** a photocunducting glass core surrounded by two metal electrodes supports a TEM mode with a complex impedance due to the finite resistively of the glass. **b.** analytical solution to idealized structure can be obtained using conformal mapping technique. This structure consists of two metal rods and a uniform core. In the case of thin film fiber detector with a polymer core, the thin layer of photoconducting glass is considered as a perturbation to the structure that introduces a complex permittivity.

The solution for the idealized structure (Fig. 5.4b) can be obtained simply by using conformal mapping. This mathematical technique allows particular transmission line geometry to be transformed into a new geometry in a second coordinate system, with a certain rules governing the relationship between the electrical properties of the lines in the two systems. Using this technique the electrical parameters of the transmission line are found to be

$$C = \frac{\varepsilon\pi}{\cosh^{-1}(c/b)}$$

$$L = \frac{\mu \cosh^{-1}(c/b)}{\pi} \tag{5.3}$$

$$Z_0 = \sqrt{\frac{L}{C}} = \sqrt{\frac{\mu}{\varepsilon}}\frac{\cosh^{-1}(c/b)}{\pi} = \frac{120}{n}\cosh^{-1}(c/b)$$

these parameters assume a uniform core having a refractive index of n and two cylindrical electrodes separated by a distance of $2c$ and having diameter of $2b$.

The permittivity of the glass is in general a complex number with the imaginary part proportional to its conductivity

$$\varepsilon \to \varepsilon - i\frac{\sigma_{dc}+\sigma_{ac}}{\omega} = \varepsilon - i\left(\frac{\sigma_{dc}}{\omega}+\frac{A}{\omega^{1-\alpha}}\right)$$

(5.4)

$$Z_0 \simeq \frac{120}{n}\cosh^{-1}(c/b)\left[1+i\frac{1}{2n^2}\left(\frac{\sigma_{dc}}{\omega}+\frac{A}{\omega^{1-\alpha}}\right)\right]$$

where $\sigma_{ac}=A\omega^{\alpha}$ is the a.c. conductivity of the amorphous glass with typical values of $\alpha \leq 1$ for different glass compositions [98-101]. Under illumination the conductivity can change by a few orders of magnitude [69,86] resulting in a change that is proportional to the local light intensity of the imaginary part of the transmission line impedance. We note that the induced change is inversely proportional to the modulation frequency. It is therefore expected that in order to obtain a measurable change in Z_0 at high frequencies the α parameter of the a.c. conductivity need to be close to unity.

We also note that the above analysis is valid for the thin-film fiber configuration, in which a thin detecting layer of glass surrounds a polymer core, with the appropriate geometrical modification to the complex term.

5.5.2 Reconstruction of the non-uniform impedance

Under illumination this one-dimensional fiber detector translates the intensity distribution into a non-uniform distribution of the complex characteristics impedance, $Z_0(z)$. This distribution can be reconstructed in terms of time domain reflectometry by sending an electrical pulse on the fiber electrodes and measuring the reflected signal (Fig. 5.5). In the simple case of single point illumination the pulse would reflect from the point along the fiber axis where the impedance is discontinuous due to change in conductivity. In that case the location can be reconstructed by measuring the time-of-flight of the signal. For an arbitrary distribution of the intensity the procedure is somewhat more complicated [102-103]. The basic idea behind the procedure is the reconstruction of the system response function using discrete linear system techniques. The transmitted and reflected signals are represented by their Z-transform and the coefficients of the system response

function (the non-uniform impedance) are reconstructed using either reconstruction methods or other techniques.

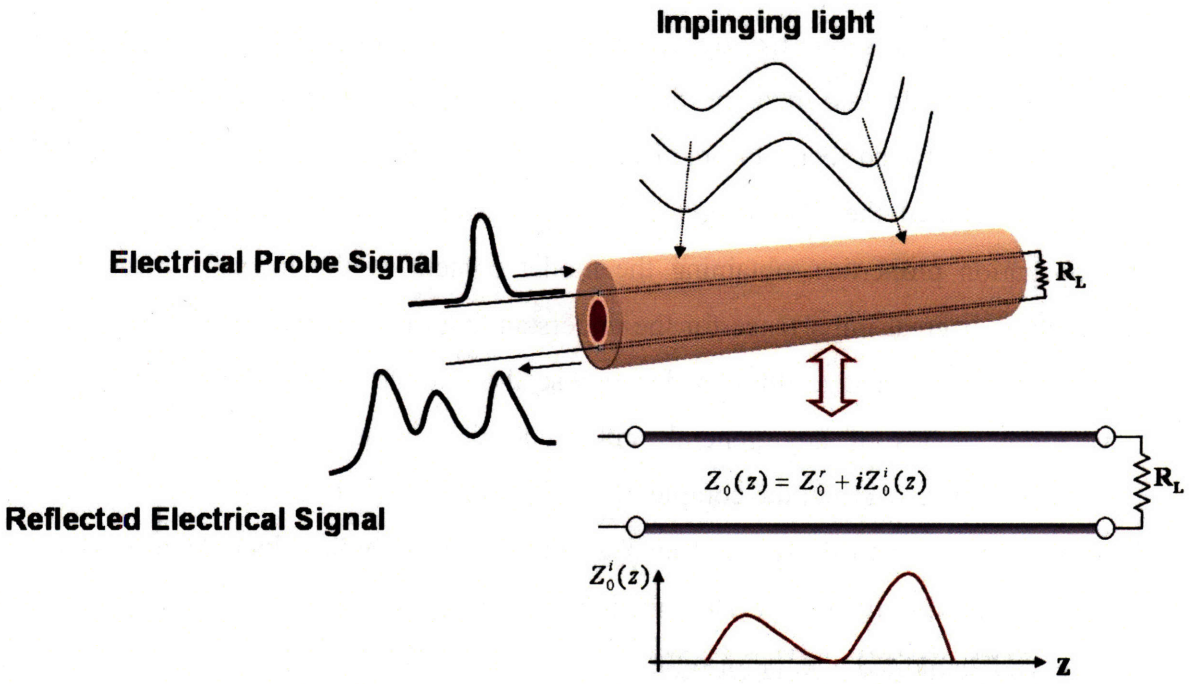

Figure 5.5: Reconstruction of the non-uniform impedance using Time-Domain-Reflectometry (TDR). An arbitrary light intensity distribution is incident on the outer surface of the fiber and in turn translated into non-uniform impedance due to the local change in the glass conductivity. These variations are reconstructed from the reflection of an electrical pulse that is sent on the fiber electrodes.

6 Conclusions

This work demonstrated the design, characterization, and analysis of a broad range of optical and optoelectronic fiber devices with functionality ranges from waveguiding electromagnetic radiation in a hollow-core photonic bandgap structure to imaging system constructed of an array of photodetecting fibers. The work begins with the study of the mode properties supported by the multimode PBG fiber. We use the leaky mode technique to calculate the core, defect, surface, and cladding modes and to analyze the interaction between them. In practice, the field emerges out from a multimode fiber is a superposition of the fiber eiegnmodes. Since each mode is characterized by different propagation properties, obtaining the modal content of the intensity measured at the output is of great importance for the understanding of light propagation inside the fiber. We developed an algorithm to decompose the complex expansion coefficients of the vectorial modes of any general multimode waveguide by using a phase retrieval technique to reconstruct the complex field from two intensity measurements. These set of tools enabled us to design and analyze higher functionality fiber devices such as the surface emission fiber laser. Here we introduced an organic gain medium into the hollow core and exploited the omni-reflectivity of the multilayer cladding to generate laser emission with an interesting dipole like radiation in the radial direction. Furthermore, the ability of the group to incorporate metals, semiconductors, and insulators in well defined fiber geometry enabled the fabrication of semiconductor fiber devices. We demonstrated here two such devices. The first was designed to have the dual functionality of both guiding high power laser power and at the same time, by integrating thermal element to the cladding, to self-monitor the temperature inside the entire fiber length for the purpose of real-time failure detection. The second made use of photo-detecting fibers to construct an optical imaging using large-area, three-dimensional optical-detector array. Lensless imaging of an object is achieved using a phase retrieval algorithm.

7 Bibliography

[1] W. D. Warters, "WT4 Millimeter Waveguide System", The bell System Technical Journal, 56, 1825, (1977)

[2] P. Yeh, E. Marom, and A. Yariv, "Theory of Bragg Fiber", Journal of the Optical Society of America, 68, 1196, (1978)

[3] M. Miyagi, and S. Kawakami, "Design Theory of Dielectric-Coated Circular Metallic Waveguides for Infrared Transmission", Journal of Lightwave Technology, LT-2, 116, (1984)

[4] Y. Matsuura, T. Abel, J. Hirsch, and J.A. Harrington, "Small-Bore Hollow Waveguide for Delivery of Near Singlemode IR Lase Radiation", Electronics Letters, 30, 1688, (1994)

[5] B. Temelkuran, S.D. Hart, G. Benoit, J.D. Joannopoulos, and Y. Fink, "Wavelength-Scalable Hollow Optical Fibers With Large Photonic Bandgaps For CO_2 Laser Transmission", Nature, 420, 650, (2002)

[6] A. Dayan, A. Goren, and I. Gannot, "Theoretical and experimental investigation of the thermal effects within body cavities during transendoscopical CO2, laser surgery", Laser in Surgery and Medicine, 35, 18-27, (2004)

[7] M. J. Renn, D. Montgomery, O. Vdovin, D.Z. Anderson, C.E. Wieman, and E.A. Cornell, "Laser-Guided Atoms in Hollow-Core Optical Fibers", Physical Review Letters, 75, 3253, (1995)

[8] E. Constan, D. Garzella, P. Breger, E. Mevel, Ch. Dorrer, C. Le Blanc, F. Salin, and P. Agostini, "Optimization High Harmonic Generation in Absorbing Gases: Model and Experiments", Physical Review Letters, 82, 1668, (1999)

[9] J. H. V. Price , T. M. Monro, K. Furusawa, W. Belardi, J.C. Baggett, S. Coyle, C. Netti, J. J. Baumberg, R. Paschotta and D. J. Richardson ", UV Generation in a Pure Silica Holey fiber", Applied Phsyics B, 77, 291 (2003)

[10] N. J. Doran and K. J. Bulow, "Cylindrical Bragg fibers: A design and feasibility study for optical communications ", Journal of lightwave technology, LT-1, 588, (1983).

[11] C. M. de Sterke and I. M. Bassett, "Differential losses in Bragg fibers ", Journal of Applied physics, 76, 680,(1994).

[12] F. Brechet, P. Roy, J. Marcou, and D. Pagnoux, "Single-mode propagation into depressed-core-index photonic-bandgap fibre designed for zero-dispersion propagation at short wavelengths", Electronics Letters, 36(6), 514, (2000).

[13] R. F. Cregan, B. J. Mangan, J. C. Knight, T. A. Birks, P. St. J. Russell, P. J. Roberts, D. C. Allan, "Single-mode photonic band gap guidance of light in air," Science **285**, 1537-1539 (1999).

[14] B. J. Eggelton, C. Kerbage, P.S. Westbrook, R.S. Windeler, A. Hale, "Microstructured optical fiber devices", Optics express 9, 698-713 (2001).

[15] C. Anastassiou, G. Dellemann, O. Weisberg, and U. Kolodny , "Fibers Deliver CO2 Laser Beams for Medical Applications", Photonics Spectra, March 2004.

[16] K. Kuriki, O. Shapira, S. D. Hart, G. Benoit, Y. Kuriki, J. F. Viens, M. Bayindir, J. D. Joannopoulos, and Y. Fink, "Hollow multilayer photonic bandgap fibers for NIR applications", Optics Express, 12, 1510, (2004)

[17] Y. Fink, J.N. Winn, S. Fan, S. Chen, J.Michel, J.D. Joannopoulos, E.L. Thomas, "A Dielectric Omnidirectional Reflector", Science, 282, 1679, (1998)

[18] S.G. Johnson, M. Ibansecu, M.Skorobogatiy, O. Weisberg, T.D. Engeness, M. Soljacic, S.A. Jacobs, J.D. Joannopoulos, and Y. Fink, "Low-loss asymptotically single-mode propagation in large-core OmniGudie fibers", Optics Express, 9, 748, (2001)

[19] M. Ibansecu, S.G. Johnson, M. Soljacic, J.D. Joannopoulos, and Y. Fink, "Analysis of mode structure in hollow dielectric waveguide fibers", Physical Review E, 67, 046608, (2003)

[20] A.W. Snyder and J.D. Love, "Optical Waveguide Theory" (Chapman and Hall, London 1983)

[21] T. Engeness, M. Ibanescu, S. Johnson, O. Weisberg, M. Skorobogatiy, S. Jacobs, and Y. Fink, "Dispersion tailoring and compensation by modal interactions in OmniGuide fibers," Opt. Express 11, 1175-1196 (2003)

[22] G. Benoit, K. Kuriki, J. F. Viens, J. D. Joannopoulos, Y. Fink, "Dynamic all-optical tuning of transverse resonant cavity modes in photonic bandgap fibers", Opt. Let., 30, 13, 1620-1622 (2005)

[23] T. A. Birks, D. Mogilevstev, J. Knight, and P. S. Russell, "Dispersion compensation using single-material fibers," IEEE Phot. Techn. Lett. 11, 674–676 (1999).

[24] S. O. Konorov, A. B. Fedotov, O. A. Kolevatova, E. A. Serebryannikov, D. A. Sidorov-Biryukov, J. M. Mikhailova, A. N. Naumov, V. I. Beloglazov, N. B. Skibina, L. A. Melnikov, A. V. Shcherbakov and A. M.Zheltikov "Waveguide modes and dispersion properties of hollow-core photonic-crystal and aperiodic-claddingfibers," Laser Physics 13, 148–160 (2003).

[25] J. D. Joannopoulos, R. D. Meade, J. N. Winn, "*Photonic Crystals*," Prinction unversiry Press (1995)

[26] H. A. Haus, W. Huang, "Coupled-Mode Theory", Proc. IEEE, 79(10) 1505-1518 (1991)

[27] G. C. Southworth, "Hyper Frequancy Wave Guides: General Consideration and Experimental results", Bell System Tech. J., 15, 284 (1936)

[28] Y. Matsuura and D. Akiyama and M. Miyagi, "Delivery of F2-Excimer Laser Light by Aluminum Hollow Fibers ", Opt. Express, 6(13), 257 (2000)

[29] M. Skorobogatiy and C. Anastassiou and S. G. Johnson and O. Weisberg and T. D. Engeness and S. A. Jacobs and R. U. Ahmad and Y. Fink, "Quantitative Characterization of Higher-Order Mode Converters in Weakly Multimoded Fibers", 11(22), 2838 (2003)

[30] Y. Matsuura and T. Abel and J. Hirsch and J. A. Harrington, "Small-Bore Hollow Waveguide for Delivery of Near Singlemode IR Laser Radiation", Elec. Lett., 30(20), 1688 (1994)

[31] R. W. Gerchberg, "A New Approach to Phase Retrieval of a Wave Front", J. Mod. Opt., 49(7), 1185 (2002)

[32] R. W. Gerchberg and W. O. Saxton, "a Practical Algorithm for the Determination of Phase From Image and Diffraction Plane Pictures", Optik, 35, 237 (1972)

[33] W. O. Saxton, "Computer Techniques for Image Processing in Electron Microscopy", Academic Press, 1978

[34] J. R. Fienup, "Phase Retrieval Algorithms - A Comparison", Appl. Opt., 21(15), 2758 (1982)

[35] H. Stark, "Image Recovery: Theory and applications", Academic Press (1987)

[36] G. N. Ramachandran and R. Srinivasan, "Fourier Methods in Crysallography", Wiley-Interscience, New York, (1970)

[37] H. A. Ferwerda, "the phase reconstruction problem for wave amplitudes and coherence functions", Inverse Source Problems in Optics (edited by H. P. Baltes) Springer-Verlag, Berlin, 1978, Chapter 2.

[38] M. H. Hayes and J. H. McClellan, "Reducible polynomials in two or more variables", *Proc. IEEE* 70 (2), 197-198 (1982).

[39] J. L. C. Sanz and T. S. Haung, "Stability of unique Fourier transform phase reconstruction", J. opt. Soc. Am. 73 (11), 1442-1445 (1983)

[40] M. H. Hayes, "The reconstruction of a multidimensional sequence from the phase or magnitude of it Fourier transform", IEEE Trans. Acoust., Speech, Sig. Proc. ASSP-30(2), 140-154 (1982).

[41] A. Walther, "The question of phase retrieval in optics", Opt. Acta 10, 41-49 (1963)

[42] R. Barakat and G. Newsam, "Necessary Conditions for a unique solution to the two-dimesnssiobal phase recovery", J. Math. Phys. 25, 3190-3193 (1984)

[43] D. Izraelevitz and J. S. Lim, "A new direct algorithm for image reconstruction from Fourier transform magnitude", IEEE Trans. Acoust. Speech Signal Process. ASSP-35, 511-519 (1987)

[44] R. G. Lane, W. R. Fright, and R. H. T. Bates, "Direct phase retrieval", IEEE Trans. Acoust. Speech Signal Process. ASSP-35 520-525 (1987)

[45] J. R. Fienup, "Reconstruction of a Complex-Valued Object from the Modulus of its Fourier Transform Using a Support Constarint", J. Opt. Soc. Am. A 4 118-123 (1987)

[46] R. H. T. Bates and D. G. H. Tan, "Fourier Phase Retrieval When the image is Complex", Proc. SPIE 558 54-59 (1985)

[47] J. Miao, D. Sayre, and H. N. Chapman "Phase Retrieval from the Magnitude of the Fourier Transform of Nonperiodic Object", J. Opt. Soc. Am. A 1662-1669 (1998)

[48] J. R. Fienup, "Lensless Coherent Imaging by Phase Retrieval with an Illumination Pattern Constraint", Opt. Express 498-508 (2006)

[49] O. Shapira., A.F. Abouraddy, J.D. Joannopoulos, Y. Fink, "Complete modal decomposition for optical waveguides," Phy. Rev. Let., 94, 14, 143902/1-4 (2005)

[50] M. J. F. Digonnet, "Rare-Earth-Doped Fiber Lasers and Amplifiers", Marcel Dekker (1993)

[51] C. W. Wilmsen, H. Temkin, and L. A. Coldren, "Vertical-Cavity Surface-Emitting Lasers: Design, Fabrication, Characterization, and Applications", Cambridge University Press (2002).

[52] V. Ntziachristos, C. Bremer, R. Weissleder, "Fluorescence imaging with near-infrared light: new technological advances that enable in vivo molecular imaging", Eur. Radiol., 1, 195-208 (2003)

[53] D. A. Boas, D. H. Brooks, E. L. Miller, C. A. DiMarzio, M. Kilmer, R. J. Gaudette, Q. Zhang, "Imaging the body with diffuse optical tomography", IEEE Sig. Proc. Mag. 18 (6): 57-75 NOV 2001

[54] A. Rose, Z. G. Zhu, C. F. Madigan, T. M.. Swager, V. Bulovic, "Sensitivity gains in chemosensing by lasing action in organic polymers", Nature 434 (7035): 876-879 APR 14 2005

[55] R. M. Verdaasdonk, and C. F. P. van Swol, "Laser light delivery systems for medical applications", Phys. Med. Biol. 42 869-887 (1997)

[56] J. Spigulis, "Emitting Fibers Brighten Our World in New Ways" OPN, October 30, (2005).

[57] Y. Yamamoto, F. Tassone, H. Cao, "Semiconductor Cavity Quantum Electrodynamics", Springer (2000)

[58] P. Berman, "Cavity Quantum Electrodynamics", Academic Press (1993)

[59] F. P. Schafer,"Dye lasers", Springer-Verlag, (1989).

[60] P. P. Sorokin, J. R. Lankard, E. C. Hammond, V. L. Moruzzi: IBM J. Res. Dev. 11, 130 (1967)

[61] T. Erdogan, O. King, G. W. Wicks, D. G. Hall, E. H. Anderson, M.J. Rooks, "Circularly Symmetrical Operation of a Concentric-circle-grating, surface-emitting, AlGaAs/GaAs quantum-well semiconductor-laser", App. Phys. Lett. 60, 1921-1923 (1992).

[62] J. Scheuer, W. M. J. Green, and A. Yariv, "Annular Bragg Resonators: Beyond the Limits of Total Internal Reflection", Photonics Spectra, May 2005

[63] C. Bauer, H. Giessen, B. Schnabel, E. B. Kley, C. Schmitt, U. Scherf, and R. F. Mahrt, "A surface-emitting circular grating polymer laser", *Adv. Mater.* **13**, 1161-1164 (2001).

[64] E. Desurvire, "Erbium-Doped Fiber Amplifiers, Principles and Applications", Wiley (2002)

[65] N. K. Dutta, and Q. Wang, "Semiconductor Optical Amplifiers", World Scientific Publishing Company (2006)

[66] M. N. Islam, "Raman Amplifiers for Telecommunications 1: Physical Pricnciples", Springer (2003)

[67] J. Y. Zhang, J. Y. Haung, Y. R. Shen, "Optical Parametric Generation and Amplfication", CRC (1995)

[68] Q. Zhou, and T. M. Swager, "Methodology for Enhancing the Sensitivity of Fluorescence Chemosensors: Energy Migration in Conjugated Polymers", J. Am. Chem. Soc. 117 71017-7108, 1995.

[69] Bayindir, M., Sorin, F., Abouraddy, A.F., Viens, J., Hart, S.D., Joannopoulos, J.D., Fink, F., "Metal-insulator-semiconductor optoelectronic fibres", Nature 431, 826-829 (2004).

[70] M. Bayindir, A. F. Abouraddy, F. Sorin, J. D. Joannopoulos, and Y. Fink, Fiber photodetectors codrawn from conducting, "semiconducting and insulating materials", Opt. and Photon. News 15, 24 (2004).

[71] M. Bayindir, O. Shapira, D. Saygin-Hinczewski, J. Viens, A. F. Abouraddy, J. D. Joannopoulos, and Y. Fink, "Integrated fibres for self-monitored optical transport", Nature Materials (November, 2005).

[72] M. Bayindir, A. F. Abouraddy, J. D. Joannopoulos, and Y. Fink, "Thermal-sensing mesoscopic fiber devices by composite-material processing", Adv. Mat., 18(7), 845-849 (2005).

[73] Y. Fink, J. N. Winn, S. Fan, J. Michel, C. Chen, J. D. Joannopoulos, E. L. Thomas, "A dielectric omnidirectional reflector", Science 282, 1679-1682 (1998).

[74] J. D. Shephard, *et al,* "High energy nanosecond laser pulses delivered single-mode through hollow-core PBG fibers", Opt. Express 12, 717-723 (2004).

[75] J. A. Harrington, "Infrared Fibers and Their Applications, SPIE Press, (2004).

[76] T. Abel, J. Hirsch, and J. A. Harrington, "Hollow glass waveguides for broadband infrared transmission" Opt. Lett. 19 1034-1036 (1994).

[77] T. Katagiri, Y. Matsuura, and M. Miyagi, "Metal-covered photonic bandgap multilayer for infrared hollow waveguides", Appl. Opt. 41, 7603-7606 (2002).

[78] A. Dayan, A. Goren, and I. Gannot, "Theoretical and experimental investigation of the thermal effects within body cavities during transendoscopical CO_2, laser-based surgery", Laser Surg. Med. 35, 18-27 (2004).

[79] Omniguide Communication Inc., private communications.

[80] D. Karasawa, M. Miyagi, and S. Nishida, "Temperature distribution along oversized hollow-core waveguides for infrared radiation" Appl. Opt. 26, 4581-4586 (1987).

[81] D. Su, S. Somkuarnpanit, D. R. Hall, and J. D. C. Jones, "Thermal effects in a hollow waveguide beam launch for CO_2 laser power delivery", Appl. Opt. 35, 4787-4789 (1996).

[82] I. Inagawa, R. Iizuka, T. Yamagishi,and R. Yokota, "Optical and thermal properties of chalcogenide Ge-As-Se-Te glasses for IR fibers", J. Non-Cryst. Solids 95-96, 801-808 (1987).

[83] V. K. Tikhomirov, "Glass formation in the Te-enriched part of the quaternary Ge–As–Se–Te system and its implication for mid-infrared optical fibers", Infrared Phys. Technol. 45, 115-123 (2004).

[84] M. A. Popescu, "Non-Crystalline Chalcogenides", Kluwer Academic Publishers (2000).

[85] B. E. A. Saleh, and M. C. Teich, "Fundamentals of Photonics", Wiley (2001).

[86] M. Bayindir, M. et al. "Fiber photodetectors codrawn from conducting, semiconducting and insulating materials", Opt. and Photon. News 15, 24 (2004).

[87] D. Adler, and E. J. Yoffa, "Electrical Strcuture of Amorphous Semiconductors", Phy. Rev. Let. 36(20) 1197-1200 (1976).

[88] A. C. Kak, and M. Slaney, "Principles of Computerized Tomographic Imaging" , IEEE Press, (1988).

[89] J. R. Fienup, "Phase-retrieval algorithms for a complicated optical system", *Appl. Opt.* **32**, 1737-1746 (1993).

[90] J. R. Fienup, "Phase retrieval for undersampled broadband images", *J. Opt. Soc. Am. A* **16**, 1831-1837 (1999).

[91] J. Miao, D. Sayre, and H. N. Chapman, "Phase Retrieval from the Magnitude of the Fourier Transforms of nonperiodic objects", J. Opt. Soc. Am. A, 15(6) 1662-1669 (1998)

[92] R. H. T. Bates, and D. G. H. Tan, "Fourier Phase Retrieval when the Image is Complex", SPIE Vol. 558 Inverse Optics II, 54-59 (1985)

[93] M. H. Hayes, "The Reconstruction of a Multidimensional Sequence from the Phase or Magnitude of its Fourier Transform", IEEE Trans. Acous. Speech, and Sig. Proc., ASSP-30(2) 140-154 (1982)

[94] J. N. Cederquist, J. R. Fienup, J. C. Marron, and R. G. Paxman, "Phase retrieval from experimental far-field speckle data", Opt. Lett. 13, 619-621 (1988).

[95] R. H. T. Bates, "Fourier phase problems are uniquely soluble in more then one dimension. I: Underlying theory", Optik 61, 247-262 (1982).

[96] J. T. Guillermo, M. E. Brezinski, B. E. Bouma, S. A. Boppart, C. Pitris, J. F. Southern, and J. G. Fujimoto, "In Vivo Endoscopic Optical Biopsy with Optical Coherence Tomography", Science, 276, 2037-2039 (1997)

[97] F. N. Dalton, W. N. Herkelrath, D. S. Rawlins, and J. D. Rhoades, "Time-Domain Reflectometry: Simultaneous Measurement of Soil Water Content and Electrical Conductivity with a Single Probe", Science, **224**, 989-990 (1984)

[98] S. R. Elliot, "A.C. conduction in Amorphous Chalcogenide and Pnictide Semiconductors", Adv. Phys., 36(2) 135-218 (1987)

[99] A. I. Lakatos, and M. Abkowitz, "Electrical Properties of Amorphous Se, As_2Se_3, and As_2S_3", Phys. Rev. B, 3(6) 1791-1800 (1971)

[100] J. J. Hauser, "Conductivity (ac and dc) in III-V Amorphous Semiconductors and Chalcogenide Glasses", Phys. Rev. B 31(4), 2133-2139 (1985)

[101] K. Shimakawa, "Microwave Absorption in Amorphous Chalcogenide Semiconductors", Phil. Mag. B., 48(1) 77-85 (1983)

[102] B. Z. Katsenelenbaum and L. Mercader del Rio and M. Pereyaslavets and M. Sorolla Ayza and M. Thumm, "Theory of Nonuniform Waveguides: The Cross-Section Method", Inst. of Electrical Engineers, 1998, London

[103] T. W. Pan, C. W. Hsue, and J. F. Huang, "Time-Domain Reflectometry Using Arbitrary Incident Waveforms", IEEE Transactions on Microwave Theory and Techniques, 50(11), 2558 (2002)